SOFIA
Stratospheric Observatory for Infrared Astronomy

FORCAST

Handbook for Archive Users

J. De Buizer, J. Radomski, S. Shenoy

Rev 1.0
Date: 2023 Sep 28

REVISIONS

REV	DATE	DESCRIPTION
0.0	2023/08/14	Initial Draft
0.1	2023/09/12	Major reformatting and copy editing
0.2	2023/09/20	Major edits and reformatting
0.3	2023/09/22	Minor edits
1.0	2023/09/28	Final formatting and edits; Released as Rev 1

FORCAST Handbook for Archive Users

Table of Contents

1. ESSENTIAL INFORMATION

Table 1: General Information About FORCAST

Instrument wavelength total range[1]	5 < λ <40 μm
Short Wavelength Camera (SWC) [1]	5 < λ < 28 μm; optimized for 5 < λ < 25 μm
Long Wavelength Camera (LWC) [1]	8 < λ < 40 μm; optimized for 25 < λ < 40 μm
Array manufacturer (SWC and LWC) [1]	DRS Tech
Pixel size (SWC and LWC) [1]	0.768 arcsec (after field distortion correction)
Array size (SWC and LWC) [1]	256 × 256 pixels
Field of view (SWC and LWC) [1]	3.4 × 3.2 arcmin (after field distortion correction)
Astrometric precision[2]	<3 arcsec
Main observing modes[3]	Imaging, Long Slit Grism Spectroscopy[4]
Spectroscopy slit widths[3]	2.4 and 4.7 arcsec
SOFIA observing cycles in service	Early Science, Cycle 1 to Cycle 9
Years in service	2010 to 2022
Built by	Cornell University (PI: Terry Herter)

[1]See Section 2.1; [2]Average across all observing cycles (see Section 3.2); [3]See Section 2.2; [4]Limited cross dispersed spectroscopy was available in Cycles 1-3 resulting in a few datasets.

Table 2: Spectroscopic Grism Characteristics, Wavelength Range, Spectral Resolution

Channel	Grism	Material	Groove Sep. (μm)	Prism Angle (°)	Order	Coverage (μm)	R (λ/Δλ) Wide Slit 4.7″ × 191″	R (λ/Δλ) Narrow Slit 2.4″ × 191″
SWC	FOR_G063	Si	25	6.16	1	4.9 - 8.0	120	180[a]
	FOR_G111	KRS-5	32	15.2	1	8.4 - 13.7	130	260[a]
LWC	FOR_G227	Si	87	6.16	1	17.6 - 27.7	110	120[a]
	FOR_G329	Si	142	11.07	2	28.7 - 37.1	160	[b]

[a] The resolution of the long, narrow-slit modes is dependent on (and varies slightly with) the in-flight image quality (See Section 3.1); [b] Only available with the 4.7'' × 191'' slit.

Table 3: FORCAST Imaging Filters, Effective Wavelengths and Range, Spatial Resolutions

Channel	Filter	λ_{mean}(µm) Single/Dual[1]	Δλ (µm)	Spatial Resolution (FWHM in arcsec)[2]	
				Single Channel	Dual Channel
SWC	FOR_F054	5.36/5.36	0.16	–[3]	–[3]
	FOR_F056	5.61/5.61	0.08	3.39+/-0.30	3.06+/-0.20[4]
	FOR_F064	6.35/6.35	0.14	2.71+/-0.21	2.70+/-0.23
	FOR_F066	6.61/6.62	0.24	–[3]	3.05+/-0.16
	FOR_F077	7.70/7.72	0.47	2.67+/-0.23	2.76+/-0.30
	FOR_F088	8.80/8.64	0.41	2.63+/-0.18	2.72+/-0.17
	FOR_F111	11.09/11.01	0.95	2.66+/-0.24	2.67+/-0.23
	FOR_F112	11.24/11.14	2.7	2.54+/-0.16	2.67+/-0.17
	FOR_F197	19.70/19.70	5.5	2.50+/-0.20	2.54+/-0.23
	FOR_F253	25.24/25.24	1.86	2.52+/-0.32	2.51+/-0.27
LWC	FOR_F113	11.34/11.31	0.24	2.57+/-0.26	–[5]
	FOR_F118	11.80/11.90	0.74	2.63+/-0.25	–[5]
	FOR_F242	24.92/27.68	2.9	2.62+/-0.25	–[5]
	FOR_F315	31.40/31.36	5.7	2.78+/-0.21	2.85+/-0.17
	FOR_F336	33.43/33.57	1.9	3.00+/-0.20	3.15+/-0.49
	FOR_F348	34.68/34.64	3.8	3.03+/-0.21	3.09+/-0.32
	FOR_F371	37.12/36.98	3.3	3.11+/-0.34	3.20+/-0.50

[1]Mean wavelength can be different for single channel and dual channel modes (see Table 15); [2]Average across Cycles 3 to 9 (see Section 3.1); [3]The 5.4 and 6.6 µm filters were used briefly in Early Science (Cycle 0) and under a limited set of other situations; sufficient data to perform an accurate image quality analysis do not exist. [4]The 5.6 µm filter was rarely used in dichroic mode and thus this value is derived from limited data. [5]Filter not usable in dichroic mode.

Table 4: Which FORCAST FITS Files Are Science-Ready From the Archive

Mode	Data Level	File type	Use
Imaging	Level 4	*_MOS_*.fits	If a region larger than the FORCAST field of view was imaged with multiple pointings, mosaic files may have been created. Also created for multiple observations of very faint sources over several Series within a Cycle. This file type is flux calibrated and science-ready[2]
	Level 3	*_CAL_*.fits (or *_COA_*.fits) [3]	For sources that are fully contained in the FORCAST field of view, their imaging data will be reduced to Level 3. This file type is the flux calibrated version that is science-ready[2, 3]
Spectroscopy	Level 4	*_SCB_*.fits	If a region was observed by scanning the slit across it, spectral maps may be available. These data cubes are flux and wavelength calibrated, corrected for tellurics, and science-ready.
	Level 3	*_CRM_*.fits (or *_CMB_*.fits) [3]	For spectra made from a single pointing, these files are the science-ready 2D spectra that have been flux and wavelength calibrated, and corrected for tellurics[3]

*[1] For a description of all file types from Levels 1-4 see Table 13; [2] Though corrected for most instrument artifacts, there may be critical residual artifacts. Check Mission ID in header of data against the "known issues" tables in Appendix D. See also Section 4.5.1 for descriptions and examples of known imaging issues and Section 4.5.2 for spectroscopic issues. [3] Until REDUX pipeline version 1.1, the most-processed imaging files were *_COA_*.fits, and until version 2.1.0 the most-processed spectroscopic files were *_CMB_*.fits (see Section 4.1 and Table 11). Calibration factors have to be applied to COA files by the user by dividing the data by the CALFCTR keyword.*

2. INSTRUMENT DESCRIPTION

In this section the design and observing modes of the FORCAST instrument are discussed. For information about the scientific objectives of FORCAST and its unique capabilities, see the introduction to Section 5.

2.1 FORCAST OVERVIEW

The **F**aint **O**bject infra**R**ed **CA**mera for the **S**OFIA **T**elescope (FORCAST) was a dual-channel mid-infrared camera and spectrograph sensitive from 5–40 μm. Each channel consisted of a 256×256 pixel array that yielded a 3.4 × 3.2 arcmin instantaneous field-of-view with 0.768 arcsec pixels, after distortion correction. The Short Wavelength Channel (SWC) used a Si:As BIBIB (Back-Illuminated Blocked-Impurity-Band) array which was functional from $2 < \lambda < 28$ μm, but in FORCAST was optimized for $5 < \lambda < 25$ μm, while the Long Wavelength Channel's (LWC) Si:Sb BIBIB array was functional from $8 < \lambda < 40$ μm but was optimized for $25 < \lambda < 40$ μm in FORCAST. Both detector arrays were manufactured by DRS Technologies (formerly Boeing North American) and are of the same design employed in the failed Wide-field Infrared Explorer (WIRE) satellite and successful (original) VISIR instrument on the European Southern Observatory's Very Large Telescope (VLT). Observations could be made through either of the two channels individually or, by use of a dichroic mirror, with both channels simultaneously across most of the range. Spectroscopy was also possible using a suite of six grisms, which provided coverage from 5–40 μm with a spectral resolution of $R = \lambda/\Delta\lambda \sim 200$.

The FORCAST instrument was composed of two cryogenically cooled cameras of functionally identical design. Light from the SOFIA telescope entered the dewar through a 7.6 cm (3.0 in) cesium iodide (CsI) window and cold stop and was focused at the field stop, where a six-position aperture wheel was located. The wheel held the imaging aperture (used for stray light reduction), the slits used for spectroscopy, and a collection of field masks for instrument characterization. The light then passed to the collimator mirror (an off-axis hyperboloid) before striking the first fold mirror, which redirected the light into the liquid helium-cooled portion of the cryostat.

The incoming beam then reached a four-position slide, which included an open position, a mirror, and two dichroics. The open position passed the beam to a second fold mirror, which sent the beam to the LWC. The mirror position redirected the light to the SWC. Both magnesium oxide (MgO) dichroics reflected light below 27 μm to the SWC and passed light from 27–40 μm to the LWC (but had subtle non-zero transmission differences from 5-12 μm). The light then passed through a Lyot stop where two filter wheels of six positions each were located, which allowed combinations of up to 10 separate filters and grisms per channel.

Finally, the incoming beam entered the camera block and passed through the camera optics. These two-element catoptric systems were composed of an off-axis hyperboloid mirror and an off-axis ellipsoid mirror that focused the light on the focal plane array. An insertable pupil viewer that imaged the Lyot stop on the arrays to facilitate alignment of the collimator mirror with the telescope optical axis and allowed characterization of the emissivity of both the sky and telescope was also included.

For more information on the optical design, thermal and mechanical descriptions, detectors and their responses, as well as a description of the instrument electronic layout, see Herter et al. (2018) and references therein.

2.2 OBSERVING MODES

FORCAST had two main observing modes: imaging and spectroscopy. Imaging was performed in single-channel mode (i.e., observing through a filter in only the SWC, or only the LWC) as well as dual-channel mode (i.e., observing through filters in both the SWC and LWC simultaneously with the use of a dichroic). The spectroscopy mode was only performed in single-channel mode. IRSA. Additionally, FORCAST had an 8.6 µm (FOR_F086) filter with a 0.21 µm width and a 25.4 µm (FOR_F254) filter with a 1.86 µm width, but these were only used for engineering purposes. However, spectroscopy could be performed with a narrow (2.4″ wide) or wide (4.7″ wide) slit, which yield slightly different spectral resolutions.

For imaging mode, the filter names, adopted central wavelengths (λ_{cen}) in micrometers, and bandwidths ($\Delta\lambda$) in micrometers are given in Table 5. Their transmission profiles are shown in Figure 1. The transmission profile data can be downloaded from the FORCAST webpage.

Table 5: FORCAST Imaging Filters

Channel	Filter	λ_{mean} (µm)* Single/Dual	$\Delta\lambda$ (µm)
SWC	FOR_F054	5.36/5.36	0.16
	FOR_F056	5.61/5.61	0.08
	FOR_F064	6.35/6.35	0.14
	FOR_F066	6.61/6.62	0.24
	FOR_F077	7.70/7.72	0.47
	FOR_F088	8.80/8.64	0.41
	FOR_F111	11.09/11.01	0.95
	FOR_F112	11.24/11.14	2.7
	FOR_F197	19.70/19.70	5.5
	FOR_F253	25.24/25.24	1.86
LWC	FOR_F113	11.34/11.31	0.24
	FOR_F118	11.80/11.90	0.74
	FOR_F242	24.92/27.68	2.9
	FOR_F315	31.40/31.36	5.7
	FOR_F336	33.43/33.57	1.9
	FOR_F348	34.68/34.64	3.8
	FOR_F371	37.12/36.98	3.3

** Mean wavelength can be different for single channel and dual channel modes (see Table 15).*

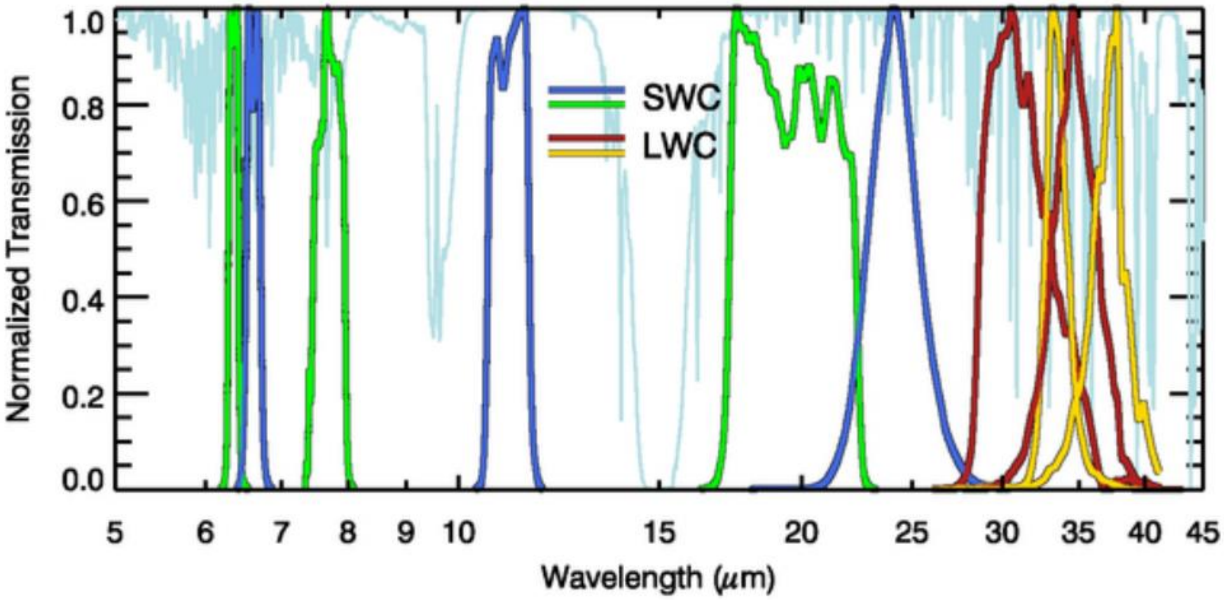

Figure 1 *FORCAST filter transmission profiles along with an ATRAN model of the atmospheric transmission across the FORCAST band (assuming a zenith angle of 45° and 7 μm of precipitable water vapor). For clarity, the filter profiles have been normalized to their peak transmission. SWC filters alternate between green and blue, while LWC filters alternate between red and yellow. Data for the actual filter profiles can be found on the FORCAST webpage at IRSA.*

For spectroscopic mode, the grism names, wavelength coverages in micrometers, and spectral resolutions for the wide and narrow slits are given in Table 6. Not shown in the table are the FORCAST cross-dispersed grism modes (R~1000) which were available in Cycles 0-3. The throughput of this mode was very low and the data were time consuming (in terms of observing time) to calibrate, and thus the mode was decommissioned at the end of Cycle 3. There were two main cross-dispersed settings: FOR_XG063, which covered 4.9-8.0 μm, and FOR_XG111, which covered 8.4-13.7 μm. A very small amount of data was collected in Cycles 1-3 using the FOR_XG063 mode, but no science data were taken with the FOR_XG111 mode.

Table 6: FORCAST Spectroscopic Grisms

Channel	Grism	Coverage (μm)	R (λ/Δλ) Wide Slit 4.7″	R (λ/Δλ) Narrow Slit 2.4″
SWC	FOR_G063	4.9 - 8.0	120	180
	FOR_G111	8.4 - 13.7	130	260
LWC	FOR_G227	17.6 - 27.7	110	120
	FOR_G329	28.7 - 37.1	160	*

** The narrow slit is not used for the longest wavelength grism.*

3. INSTRUMENT PERFORMANCE

3.1 BEAM / IMAGE QUALITY

Unlike some of the SOFIA instruments working at longer wavelengths, FORCAST image quality was a product of several factors, many of which changed from flight to flight, within a flight, or as a function of target specific issues. Therefore, unlike those other long-wavelength SOFIA instruments, and unlike mid-infrared data from a satellite mission, FORCAST image quality was highly variable.

Typically, however, the FORCAST imaging data are close to or at the diffraction limit at wavelengths greater than 30 µm. From 8 to 30 µm the image quality was typically limited by wind-driven telescope vibrations (aka “jitter”), though at high altitudes and with favorable conditions the image quality could sometimes be diffraction limited down to 20 µm. At wavelengths less than 25 µm, FORCAST image size did not decrease, as one might expect, but instead flattened out and even appeared to rise at wavelengths less than 7 µm. A reason for this behavior was never found, as the problem could not be reproduced in a lab setting and other SOFIA instruments that work at FORCAST’s shortest wavelength (e.g., FLITECAM at 5 µm) did not suffer from as poor image quality in-flight.

Issues affecting image quality of FORCAST data are:

Telescope jitter

Jitter is the name given to the vibrations of the telescope produced by the movement of the aircraft as well as environmental winds and gusts. The opening in the cavity of the plane housing the telescope was not covered by a window but was open to the outside environment. Though the aircraft fuselage was designed to minimize turbulent airflow over the cavity opening (i.e., shear layer turbulence), it was not perfect, and winds could directly drive oscillations in the top end of the telescope. Reflections of the winds within the telescope cavity (i.e., cavity turbulence) could also jostle the telescope. Additionally, at the high altitudes the aircraft flew, it could encounter high-speed jet streams and gusts, and the angle of incidence of the aircraft with such winds could also affect the amount of jitter.

Aircraft altitude

Tests have shown that the higher the aircraft altitude, the less wind-driven telescope vibrations were observed (i.e., jitter) and the better the image quality of the observations were.

Telescope elevation

Test have also shown that there was a general trend in image quality due to the elevation (i.e., the angle from the horizon) of the telescope during the observations, with the worst image quality generally being encountered at telescope elevations near 45° and the best at the upper (~58°) and lower (~23°) elevation limits of the telescope. However, this trend was only occasionally noticeable in the FORCAST data at the shortest (i.e., <10 µm) data.

Chop amplitude

If observations were taken with symmetric chopping (i.e., NMC or C2N mode), then the larger the chop amplitude, the more the image size would be increased due to coma. For large chop throws (greater than 180″) this degradation could be significant (see Figure 2). This degradation did not occur in C2NC2 mode.

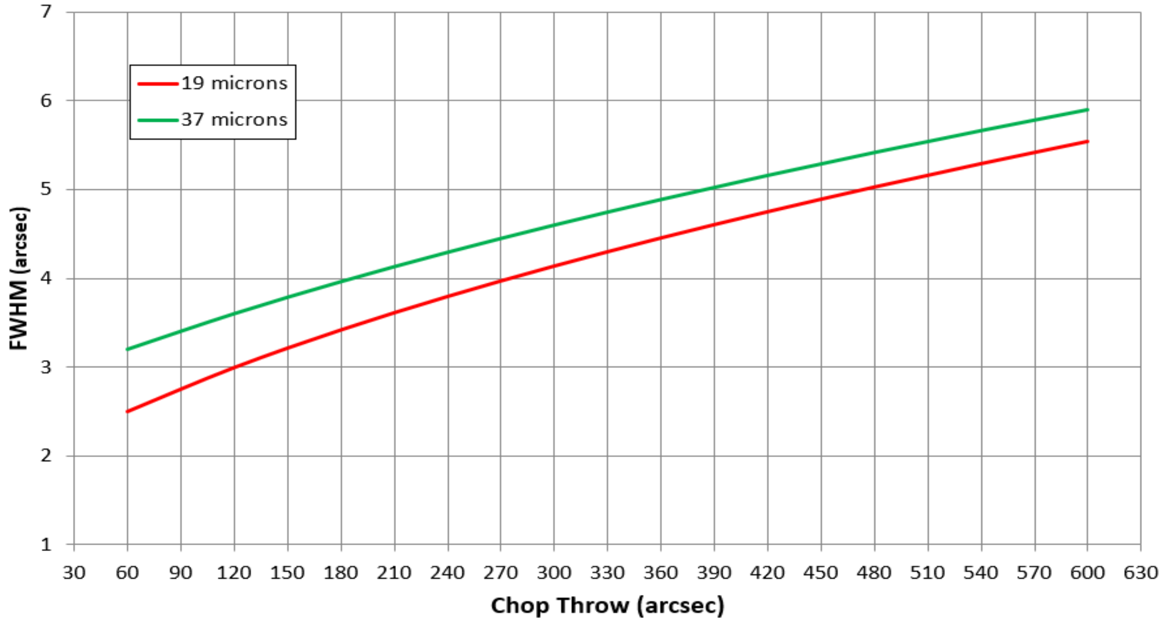

Figure 2 *The effects of image quality as a function of chop throw size for symmetric chop modes (i.e., C2N, NMC). Larger chop throws introduced more coma and increased the effective FWHM of images. This effect decreased substantially with longer wavelength (i.e., this was only a minor issue for instruments like GREAT, FIFI-LS, and HAWC+). For clarity, chop throw is equal to twice the chop amplitude (for symmetric chop modes only).*

Aircraft turbulence

The active optics of the SOFIA telescope could maintain the telescope pointing under modestly severe turbulence, however there could be some degradation of image quality during turbulent episodes.

Active optics precision

As described above for aircraft turbulence, SOFIA had an active control system that corrected telescope pointing multiple times a second. This could reduce the effects of telescope jitter and turbulence. However, these systems were fine-tuned over the course of the first three SOFIA observing cycles, and thus image quality in general improved over that time as well. Therefore, early-cycle FORCAST data in general has poorer image quality than later cycles (i.e., Cycles 4-9).

Active mass dampers

An additional vibration control system was tested and implemented on some of the Cycle 9 FORCAST flight series and further reduced the negative effects of jitter and turbulence, resulting in improved image quality.

Figure 3 shows the average image quality versus wavelength for FORCAST with errors averaged over all FORCAST flights and flight series in Cycle 7. If knowledge of the FORCAST PSF is needed with greater precision for additional science, it is best to compare the target PSF to that of a point source on the same field as the target. Unfortunately, this is not a frequent occurrence. Standard stars from the same flight or flight series can be used to estimate the PSF, with the caveat that some or all the issues listed above may be different (and extremely difficult to account for) when compared to the target observations. Therefore, using many standard star observations close in time to the target observations (i.e., in the same flight series) to get a mean PSF size with errors is the only alternative to using the numbers given in Table 3.

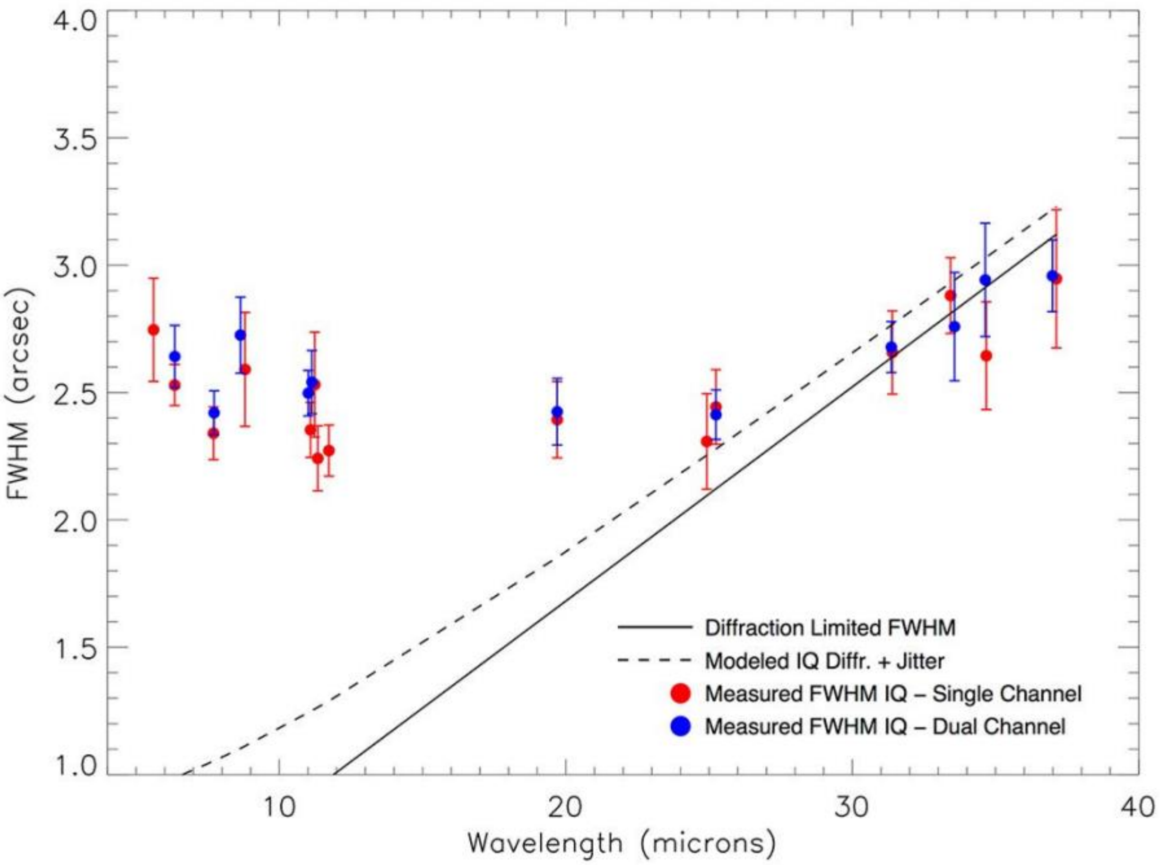

Figure 3 *Measured image quality vs. wavelength for the FORCAST camera in select filters as measured during Cycle 7 (these values come from Table 2 of this document). Also shown are the diffraction limited FWHM (solid line; calculated for a 2.5-m primary with a 14% central obstruction) and the modeled IQ (dashed line), which includes shear layer seeing and 0.5 arcsec rms telescope jitter (corresponding to 0.83" FWHM).*

3.1.1 PSF Stability Over Time

Figure 4 demonstrate the stability of the image quality of FORCAST over time. Using data from calibration stars, an average FWHM was measured in each FORCAST flight series from Cycle 3 to Cycle 9. A line is fit to the mean value and the legends give that mean value and the errors over all flight series shown. These data are also given in Table 3. Figure 4 shows all of the data for filters in the SWC in single channel mode, Figure 5 shows the LWC filters in single-channel mode, Figure 6 shows the data for all filters in the SWC when in dual-channel mode (i.e., the dichroic is in the optical path), and Figure 7 shows the data for all LWC filters in dual-channel mode.

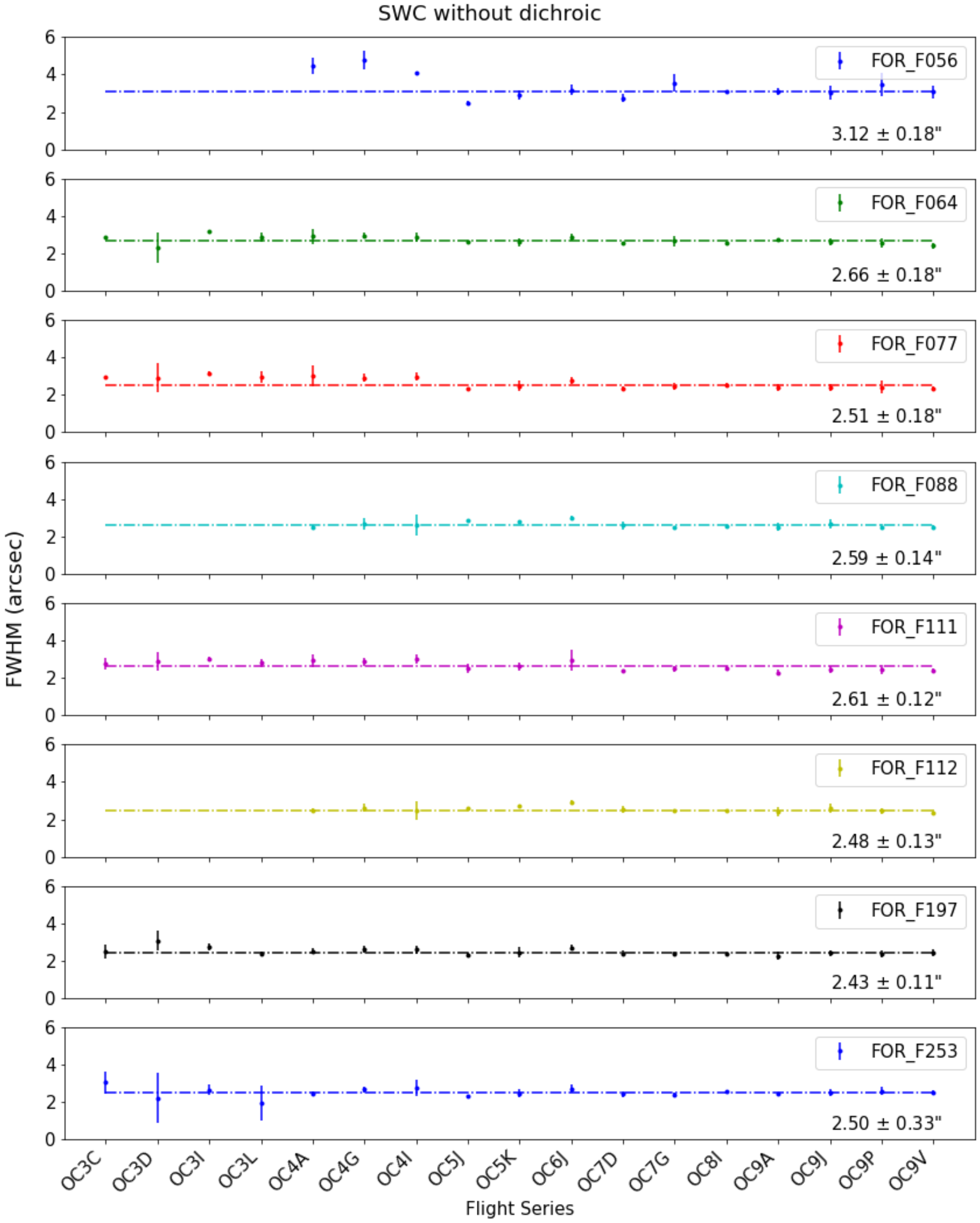

Figure 4 *Measured FWHM in arcsec for different SOFIA FORCAST observing series. These data were measured by observing the standard stellar calibrators in each series. These data are for Short Wavelength Channel (SWC) without dichroic (i.e., single-channel mode). Each of the panels displays data for a given filter listed on the top right-hand-side of the panel. The numbers in the bottom right-hand-side of the panel are the median FWHM in arcsec.*

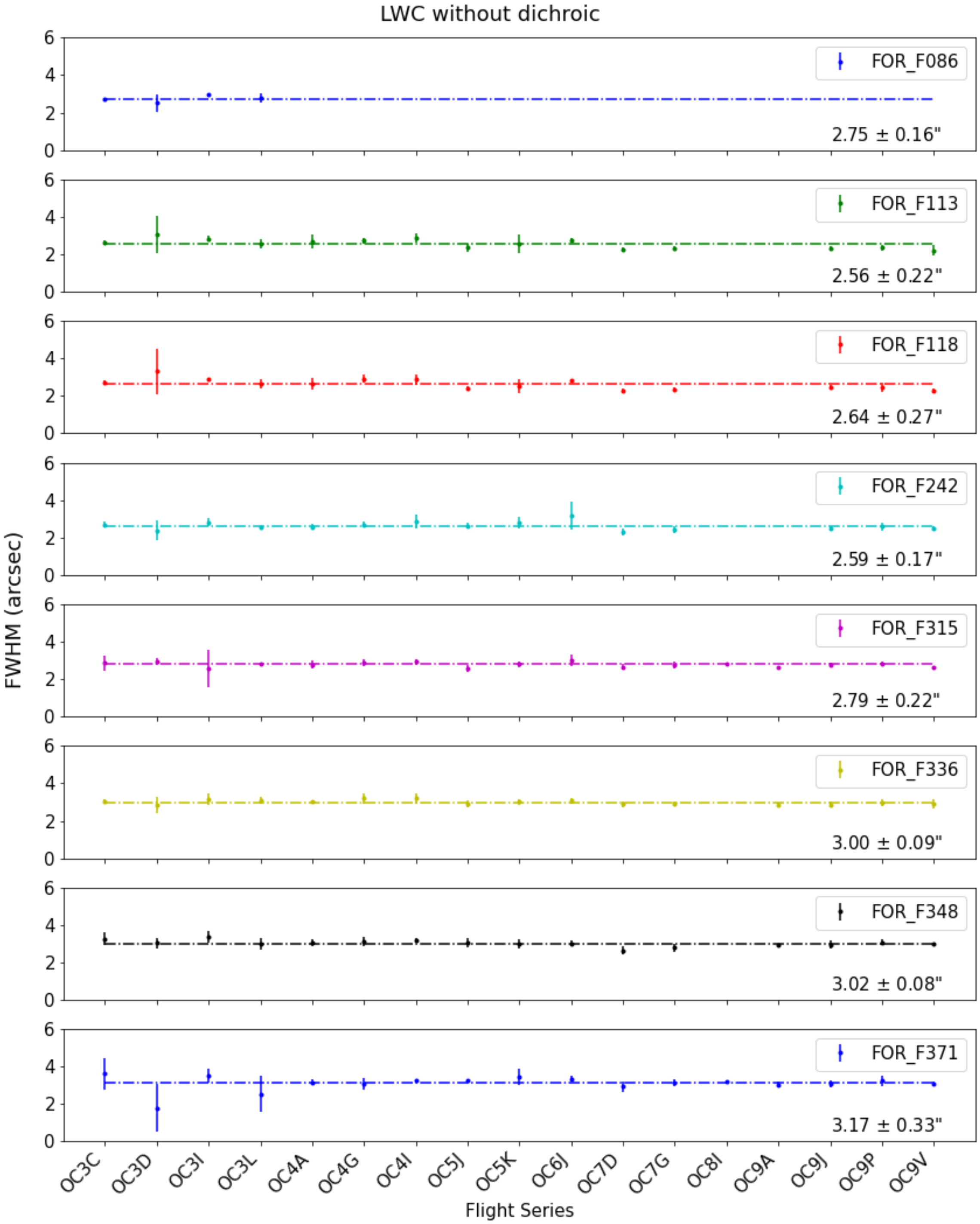

Figure 5 *Same as Figure 4 but for data obtained in the Long Wavelength Channel (LWC) without dichroic (i.e., single-channel mode).*

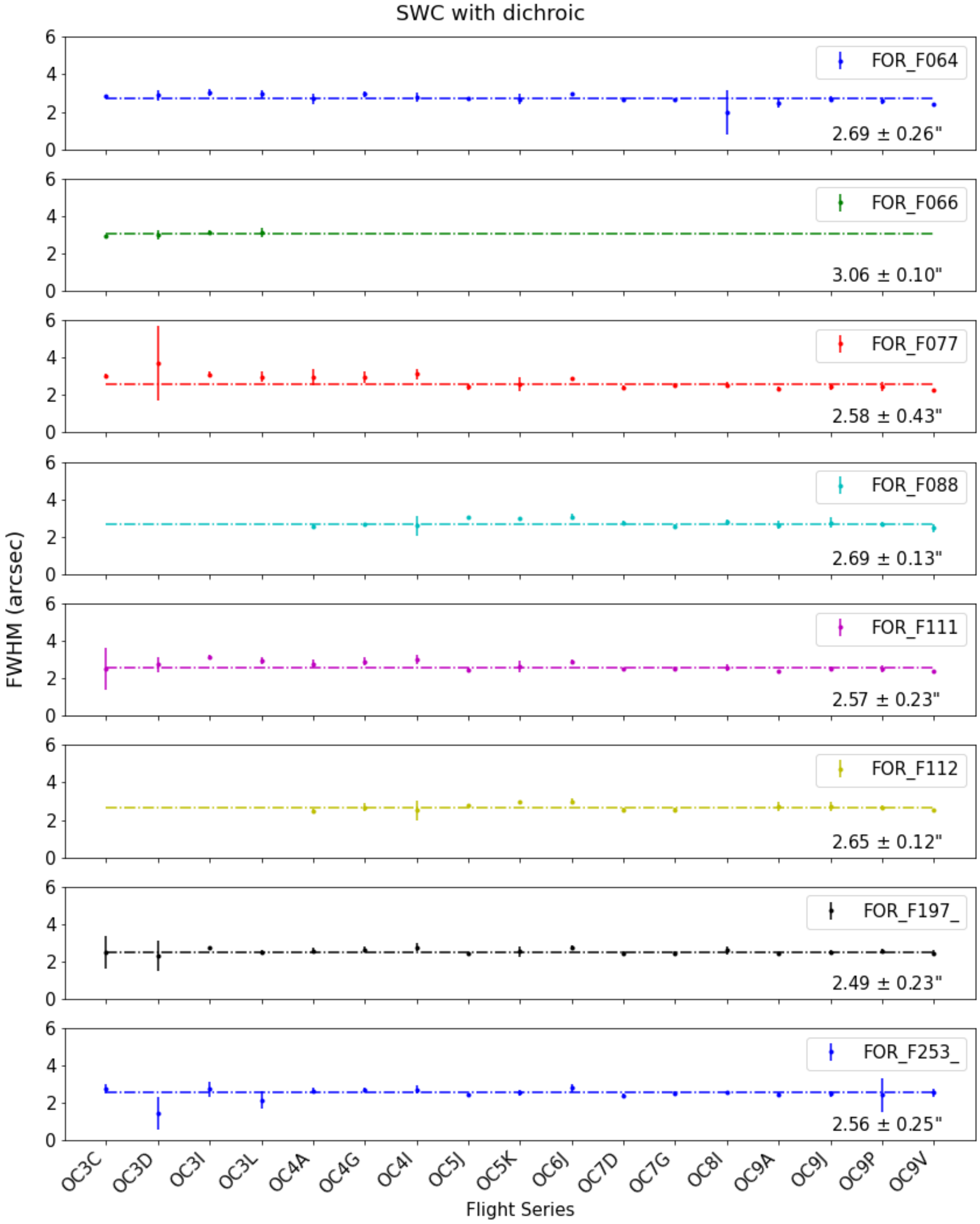

Figure 6 *Same as Figure 4 but for data obtained in the Short Wavelength Channel (SWC) with dichroic (i.e., dual-channel mode).*

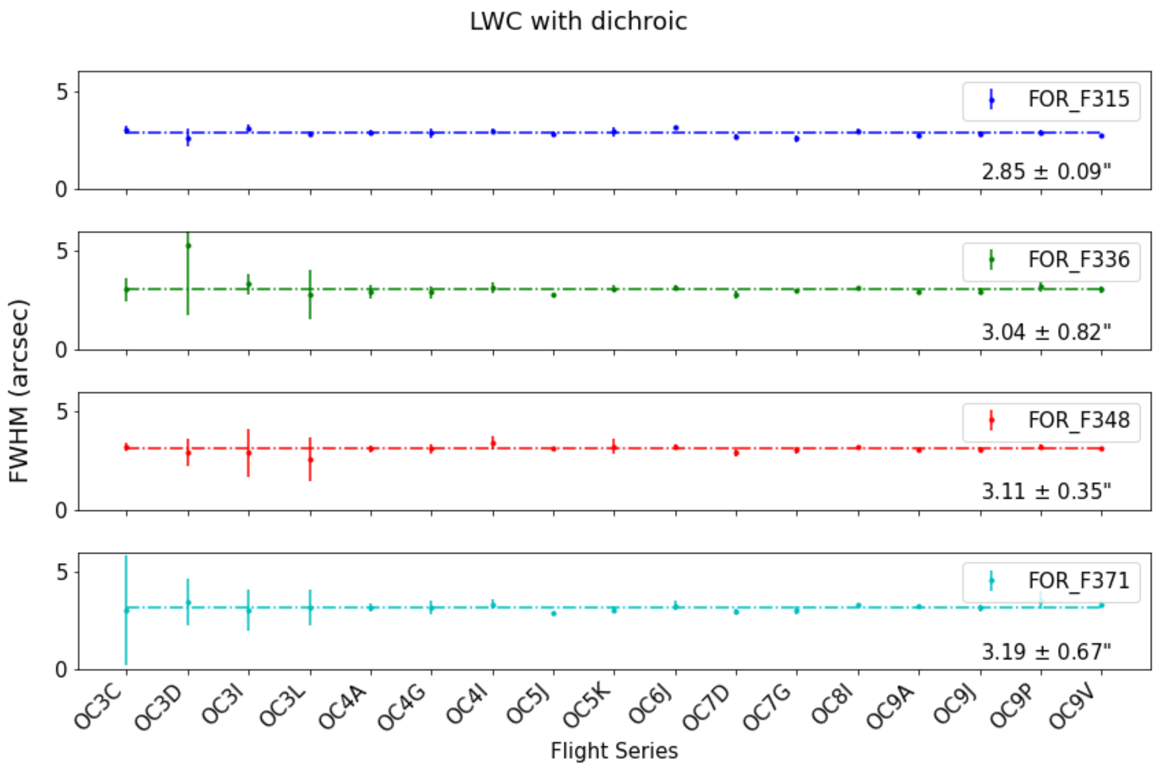

Figure 7 *Same as Figure 4 but for data obtained in the Long Wavelength Channel (LWC) with dichroic (i.e., dual-channel mode).*

3.2 POINTING PERFORMANCE

3.2.1 Telescope Boresight Definition and Accuracy

At the beginning of a flight, the telescope optical axis (a.k.a. boresight) was set-up to be (or confirmed to be) aligned with a certain pixel location on the FORCAST array. This set-up was done using the SWC 11.1 µm filter without the dichroic present (i.e., single channel mode). This position was measured and updated each flight series and had a measurement error of approximately ±1 pixel. Offsets between filters ranged from < 1 pixel to more than ~10 pixels in the case of FOR_F197 and FOR_F371. Table 7 and Table 8 give the relative offsets on Level 1 data (i.e., raw data prior to distortion correction) by filter and mode. The presence of different filters and the dichroic shift the boresight position on the FORCAST array due to difference in their intrinsic indexes of refraction. With the release of FORCAST REDUX version 1.1.3 (2016-09-20) and in subsequent releases of the pipeline, these filter shifts were removed consistently and automatically from the data in the Level 2 and 3 data products. In previous series the set-up of the pixel locations of the boresights were not always consistent from flight to flight. Therefore, for early FORCAST data, there was an additional uncertainty in the telescope pointing, and therefore astrometry (see Section 4.5.1.16).

Additionally, though never formally quantified or studied, it is known observationally that the boresight position on FORCAST could drift over a flight by 1-3 FORCAST pixels (or ~1-2″), possibly due to the telescope/optics temperature changes over the course of each flight.

Table 7: Filter Shifts for the FORCAST SWC

Short Wavelength Channel			
Mode	**Filter**	**Filter Shift***	
		dx	**dy**
SINGLE	FOR_F056	-1.3	-1.3
SINGLE	FOR_F064	-1	-4.2
DUAL	FOR_F064	-1.9	-4.5
SINGLE	FOR_F077	-0.5	-0.6
DUAL	FOR_F077	-1.3	-0.7
SINGLE	FOR_F088	-2	-1.4
DUAL	FOR_F088	-2.6	-1.5
SINGLE	FOR_F111	0.0	0.0
DUAL	FOR_F111	-0.6	0.0
SINGLE	FOR_F112	-1.4	-1.3
DUAL	FOR_F112	-2.3	-1.6
SINGLE	FOR_F197	-4.6	-1.9
DUAL	FOR_F197	-5.2	-1.9
SINGLE	FOR_F253	-0.6	-1.9
DUAL	FOR_F253	-1.4	-2.2

** With respect to the 11.1 μm filter in single channel mode (i.e., no dichroic). Based on values measured on 1/27/22. Typical errors ±1 pixel over several Cycles, though larger changes could appear in early data when filters were swapped.*

A similar procedure was done for spectroscopy, but the slit appeared in approximately the same location ±2 pixels in each of the SWC and LWC arrays, with an offset of ~6-7 pixels between the short and long wavelength position in the X direction. In the Y direction, the boresite in spectroscopy mode was set approximately 30 pixels higher on the array than in imaging to avoid dispersing the spectra over bad pixels areas. Thus, spectroscopic data are centered on the top half of the array.

3.2.2 Astrometric and WCS Accuracy

In additional to the potential offsets due to the inaccuracies of the boresight alignment and drift described in the previous section, the understanding and recording of the astrometry associated with FORCAST data has gone through several stages as technical improvements have steadily been made to enhance overall accuracy. Known data issues with WCS are documented in the tables in Appendix D. As with all issues with FORCAST data, please refer to specific quality assessment (QA) comments located in the HISTORY of the individual .fits files for more information. A general timeline of improvements is listed below:

Table 8: Filter Shifts for the FORCAST LWC

Long Wavelength Channel			
Mode	Filter	Filter Shift*	
		dx	dy
SINGLE	FOR_F113	-1.9	-0.6
SINGLE	FOR_F118	0.1	0.6
SINGLE	FOR_F242	-0.8	0.6
SINGLE	FOR_F315	0.0	0.0
DUAL	FOR_F315	5.7	3.5
SINGLE	FOR_F336	-1.5	-0.2
DUAL	FOR_F336	4.1	3.5
SINGLE	FOR_F348	-1.2	0.3
DUAL	FOR_F348	4.4	3.5
SINGLE	FOR_F371	-1.5	0.9
DUAL	FOR_F371	4.2	4.7

** With respect to the 31.5 μm filter in single channel mode (i.e., no dichroic). Based on values measured on 1/27/22. Typical errors showed a standard deviation of 0.2 in measurements over several Cycles, though larger changes could appear in early data when filters were swapped.*

Cycle 1 - Cycle 2 (2013-2015) – This was the very earliest FORCAST data and both the telescope and instrument were being commissioned. WCS header keywords often did not record accurate information from the telescope or have a consistent format, and it was common that the position of the off-source rather than on-source beam was recorded. This resulted in the astrometry being off by the distance of the Chop/Nod Throw on scales of 60″ to ~400″ or more. Fixes were applied when possible and recorded in the QA comments.

Cycle 3 (2015) – Updates to the MCCS telescope system/keywords were being finalized and new discrepancies with FORCAST keywords resulted in the same issue that the position of the off-source rather than on-source beam was often recorded. At this point the issue was primarily with C2NC2 mode as NMC mode began to become more accurate. FORCAST header keyword WCSQUAL was initially used to mark as NOMINAL/PROBLEM depending on whether WCS had major issues or not.

Cycle 4 (early 2016) – The keyword issues were primarily fixed for all modes and coordinates. During this time updates were being made to account for filter shifts and boresight definitions, improving all data to have a WCS typical accuracy of order of a few arcseconds with occasional larger deviations no worse than 10″. Since it was not viable to check WCS to accuracies better than this, WCSQUAL keyword was always marked as UNKNOWN in the data and any specific issue were noted in the QA comments.

Cycle 4 – Cycle 9 (later 2016-2022) – Unless otherwise noted in QA comments, astrometry was typically accurate to within a few arcseconds.

In early data (Cycles 1-3, or <2016) caution should be taken with the WCS due to the many issues, and, when available, the OBSRA and OBSDEC FITS header keywords which list the requested position from the observer may be more accurate than the CRVAL1 and CRVAL2 WCS positions recorded by the telescope. From later Cycle 4 onwards (2016-2022), unless noted, the general accuracy of FORCAST data are on the order of a few arcseconds. In all cases multiwavelength data should be checked and the FORCAST data may need to be adjusted to make final updates to the astrometry for more accuracy. This was done during QA of LEVEL4 mosaic data when possible, which results in a higher accuracy for those products. Doing this for all LEVEL3 data products was not viable in order to release the data in a timely manner. In addition, several issues arose when trying to get better accuracy than 1-2″:

- Most observations in FORCAST did not contain multiple star fields (like optical/near-IR) for astrometric alignment, as most stars have little thermal emission in the 5-40 μm range.

- The boresight (e.g., pointing) of the telescope could slightly change by ~1-3 FORCAST pixels (1 pixel = 0.768″) relative to the FORCAST array over a night of observing, possibly due to the telescope system cooling at stratospheric temperatures and/or pointing accuracy.

- FORCAST had higher resolution than similar observations taken using other instruments (e.g., WISE, MSX, etc.), making exact alignment difficult.

- FORCAST observed some of the brightest regions (e.g., Galactic Center) which are partially to completely saturated in other data sets (e.g., WISE, SPITZER) so no maps at similar wavelengths are available for comparison.

- FORCAST observed at longer wavelengths than SPITZER and JWST and changes in temperature of dust features may shift the position from cooler dust at 37 μm to warmer dust at 10-20 μm.

- There was a slight field distortion that increased towards the edges of the array (see Section 4.5.1.14) which can result in a few pixel (1-3″) position offsets.

Overall, the final astrometric alignment for FORCAST data will need to be looked at from a scientific perspective using multiple data sets and comparing different source types to align as best as possible.

3.3 SENSITIVITY

3.3.1 Saturation

Since SOFIA was observing through the Earth’s atmosphere, in terms of sensitivity it was more like a ground-based observatory than a space-based observatory. FORCAST observations were background-limited, which means that its detectors received several orders of magnitude more photons from the telescope and sky than typical astronomical objects. For even the brightest astronomical sources (with the only exceptions perhaps being Jupiter, Eta Car, and the Moon), FORCAST still received more background photons on its array than from the source. The techniques for how background subtraction was performed to extract the signal from these high backgrounds are described in Appendix A, but in terms of sensitivity, being background-limited had a distinct bonus. FORCAST arrays were tuned to typically read-out when they reached 50% well-depth (i.e., 50% of the saturation limit) and therefore the array did not saturate on bright astronomical sources (with the exceptions being the sources listed above; and even those could be observed without saturation after some tweaking of the observational parameters). The most common cause for detector saturation was due to the presence of clouds (see Section 4.5.1.11).

Therefore, although the FORCAST array could not be tuned to be as sensitive as space-based facilities like Spitzer and WISE because of the emission from the Earth's atmosphere and the warm telescope, unlike those facilities, FORCAST was well-suited to observe the brightest objects in the cosmos.

3.3.2 Imaging Sensitivities

The FORCAST imaging sensitivities for a continuum point source for each filter are presented in Figure 8 where the Minimum Detectable Continuum Flux (MDCF; 80% enclosed energy) in mJy needed to obtain a S/N = 4 in 900 seconds of on-source integration time is plotted versus wavelength. The MDCF scales roughly as (S/N) / √t where t is the on-source exposure time. The horizontal bars indicate the effective bandpass at each wavelength. At the shorter wavelengths, the bandpass is sometimes narrower than the symbol size. Atmospheric transmission will affect sensitivity, depending on water vapor overburden. The sensitivity is also affected by telescope emissivity, estimated to be 15% for Figure 8.

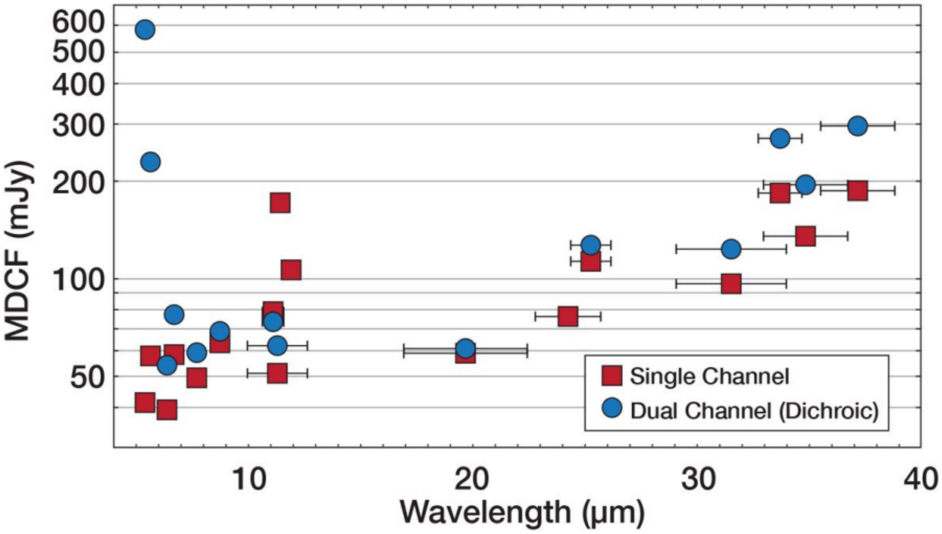

Figure 8 *Cycle 10 continuum point source sensitivities for single and dual channel modes. Values are for S/N = 4 in 900 s under nominal conditions.*

3.3.3 Grisms Sensitivities

Figure 9 presents the continuum point source sensitivities for the FORCAST grisms. The plots are the MDCF in Jy needed for a S/N of 4 in 900 seconds at a water vapor overburden of 7 µm, an altitude of 41K feet, and a zenith angle of 60°. The rapid variations with λ are due to discrete atmospheric absorption features (as computed by ATRAN).

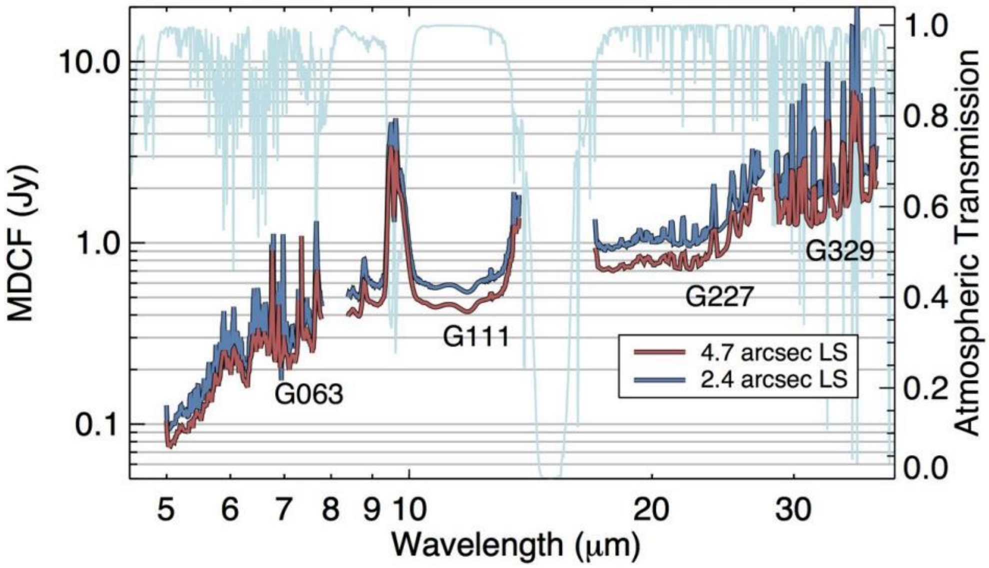

Figure 9 *Cycle 7 grism continuum point source sensitivities for both wide and narrow long slits overlaid on an atmospheric transmission model (light blue). Values are for S/N = 4 in 900 s under nominal conditions.*

3.4 FLUX CALIBRATORS AND FLUX CALIBRATION ACCURACY

3.4.1 FORCAST Flux Calibrators

The flux calibration error value, ERRCALF, is given in the headers of the FITs images. The process for deriving imaging flux calibration error (ERRCALF) is detailed in Section 4.4. In short, this value is derived from the standard deviation of the calibration factors across multiple flights using several different stellar standard stars and asteroids. For imaging flux calibration, only stellar sources are used (for more on imaging calibration see Section 4.4.1). Then, using the flux calibrated data, a blackbody model is built for the asteroid data, which are then used to calibrate the long wavelength FOR_G227 and FOR_G329 grism data (for more on grism calibration see Section 4.4.2).

FORCAST used a limited set of stellar and asteroid calibrators to flux calibrate imaging and spectroscopy data, and these are given in Table 9 and Table 10.

The stars in Table 9 were chosen because they are cool enough and bright enough to still have significant flux out to 25 μm to allow for rapid observation. All of these stars also have MARCS spectral energy models (Model Atmospheres with a Radiative and Convective Scheme; Gustafsson et al. 2008) out to at least 200 μm which were confirmed via observations to be accurate by the Herschel calibration team (Dehaes et al. 2011).

For the longest wavelengths of FORCAST (30-40 μm), the stellar calibrators in Figure 9 have modest flux for spectroscopic calibrations, and so cooler sources, i.e., asteroids, were needed. Furthermore, performing calibrations using both stellar and asteroid calibrators allowed for better understanding of the color corrections of the filters (see Section 4.4.1.1). The selection of asteroid calibrators to be used for any given flight series with FORCAST was done based on which ones were brighter than 150 Jy and 25 μm during the time of year they were to be observed. Table 10 lists all asteroids ever used as calibrators for FORCAST.

Table 9: FORCAST Stellar Calibrators for Imaging and SWC Grism Data

Stellar Calibrators	Spectral Type
Alpha Boo	K2IIIp
Alpha Cet	M2III
Alpha Tau	K5III
Beta And	M0III
Beta UMi	K4III
Gamma Dra	K5III
Sigma Lib	M3/M4III

Table 10: FORCAST Asteroid Calibrators for LWC Grism Data

Asteroid Calibrators
1 Ceres
2 Pallas
3 Juno
4 Vesta
10 Hygiea
15 Eunomia
19 Fortuna
52 Europa
532 Herculina

3.4.2 Flux Calibration Accuracy

There are two types of flux calibration error: relative and absolute. Relative flux error refers to how variable (precise) the measurements are from observation to observation. Absolute flux error refers to how accurate observations are at producing measured flux values consistent with a known flux quantity.

3.4.2.1 Imaging Relative Flux Error

The RMS error in the ERRCALF values in the FITS headers (derived across multiple calibrators and flights) are typically on the order of about 6% (see Herter et al. 2013). This error is mostly the statistical measurement error.

3.4.2.2 Imaging Absolute Flux Error

Because most of the calibration stars are mildly varying and stellar models are also not perfect (see Dehaes et al. 2011), there is an additional uncertainty that must be applied to derived FORCAST imaging fluxes, which is on the order of 5-10%. Combined, the above relative error and this error give the “absolute” flux calibration error.

3.4.2.3 Grism Relative Flux Error

Comparisons between the calibrated FORCAST spectra of standard stars and their models show deviations on the order of about 5% (RMS) for the G063, G227, and G329 grisms throughout their spectral ranges. For the G111 grism, the RMS deviation across its spectral range is found to be on the order of about 10%, due primarily to the highly variable ozone feature at 9.6 µm.

3.4.2.4 Grism Absolute Flux Error

Because slit losses can be variable during a science observation (due to varying image quality and, perhaps, slit drift) as well as for calibration observations, absolute flux calibration of FORCAST spectra require additional photometric observations taken in FORCAST imaging mode. Spectra can then be scaled to match the photometric points to achieve absolute flux calibration. Because this final calibration step is dependent upon the imaging photometry absolute flux error, the error described in Section 3.4.2.2 must be combined with the grism relative error to obtain the spectroscopic absolute flux error.

3.4.3 Flux Calibrator Variability Over Time

To assess the variability of flux calibration over time the reference calibration factors are measured (see Section 4.4 for details) for each FORCAST filter per observing series, which is a robust average of all reference calibration factors derived for every standard observation in a given series and it is compared versus the average of the reference calibration factor (master calibration factor) for the entire lifetime of SOFIA.

The plots below show reference calibration values (symbols) for each series and for each filter (colors). The solid line in the plot corresponds to the master calibration value. Figure 10, Figure 11, Figure 12, and Figure 13 are the data for observations of each filter without the dichroic and Figure 14, Figure 15, and Figure 16 are for filters with dichroic.

In these figures_it can be seen that, for SWC filters (regardless of observations with or without dichroic), series OC6J, OC7D, and OC7G are outliers. This is due to an instrument issue that began in OC6J, where the entrance window was found to be degraded and needed a replacement (see Section 4.5.1.15 for more details). In the next two FORCAST flight series multiple entrance windows were tested. However, after these three outlier flight series, the reference calibration factors in the SWC filters returned to the nominal values that were seen before the window incident (e.g., Figure 17). Similarly, for LWC filters with or without dichroic it was found that there was an offset in the reference calibration values after the OC6J series, however this offset continued until the last FORCAST flight series (e.g., Figure 18). Why only the LWC filters remained affected is unknown, but as both science and calibrators were affected similarly, it is not believed that this affects the LWC flux calibration accuracy (or accuracy of the three SWC outlier series).

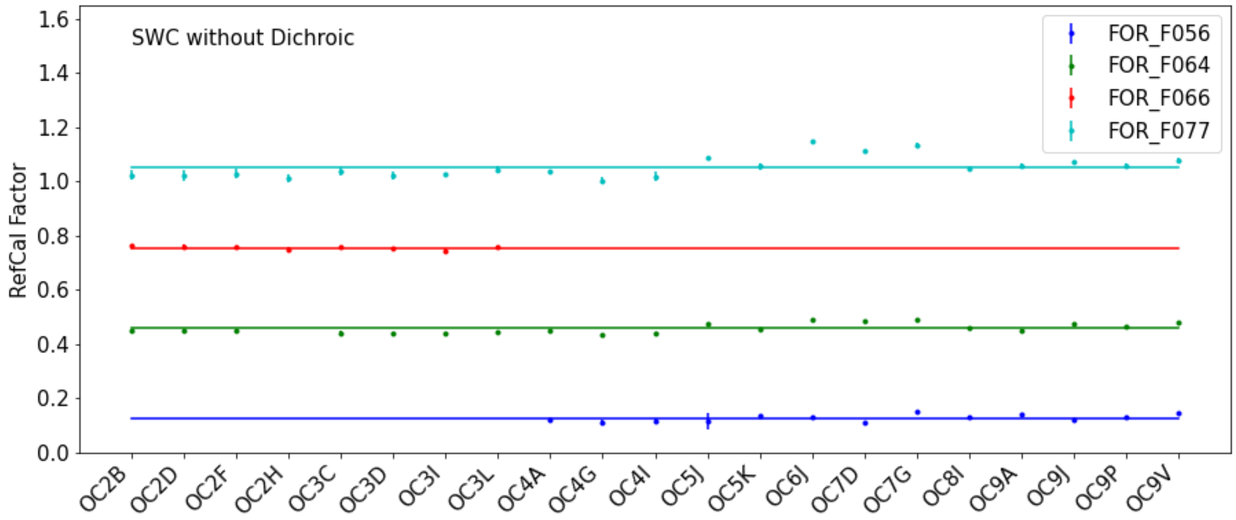

Figure 10 *Plot of Reference Calibration Factor (see Section 4.4) for all of the SOFIA FORCAST flight series. The data shown above is for Short Wavelength Channel (SWC) without dichroic. The data for each of the filters are plotted with an offset for display purpose. Series OC6J to OC7G shows larger deviation than nominal due to different entrance windows used during these observations.*

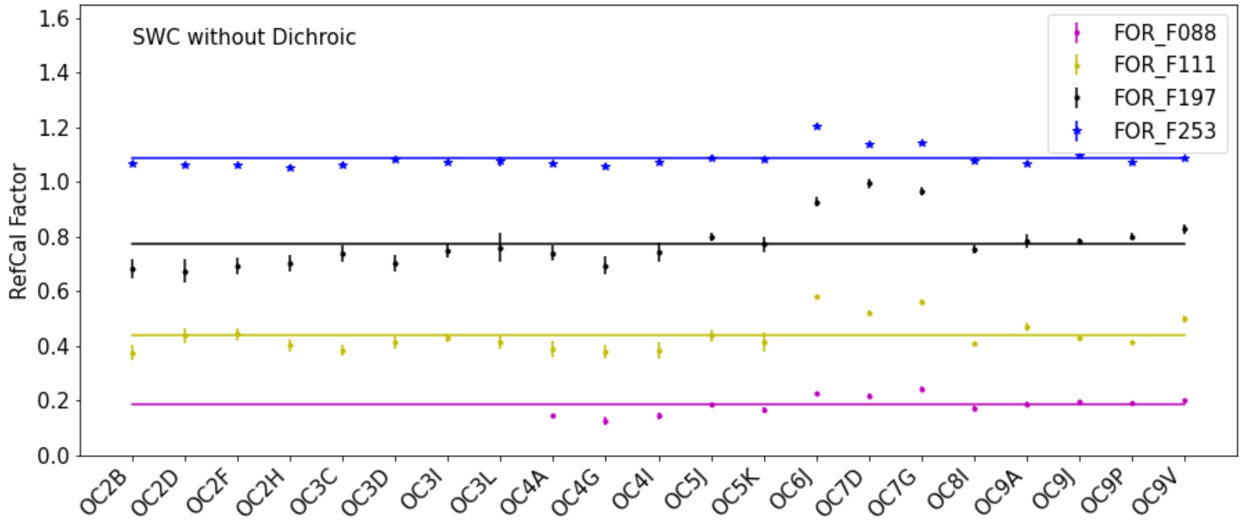

Figure 11 *Same as Figure 10 but for a different set of Short Wavelength Camera filters.*

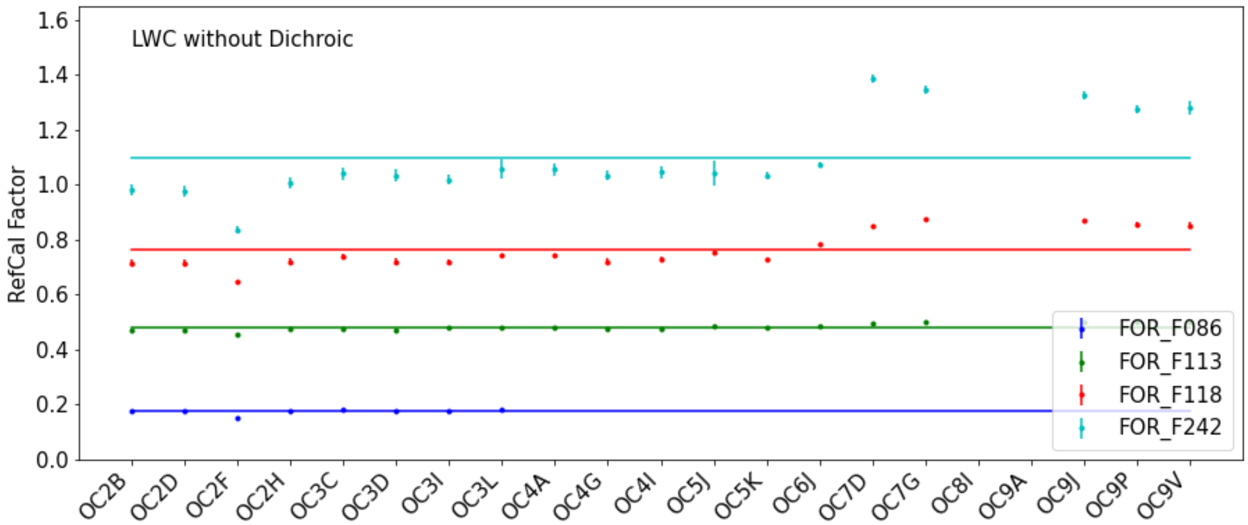

Figure 12 *Same as Figure 10 but for Long Wavelength Channel (LWC). In the case of LWC data the change in the calibration factors after the changes made to the entrance window of the instrument in series OC6J can be clearly observed.*

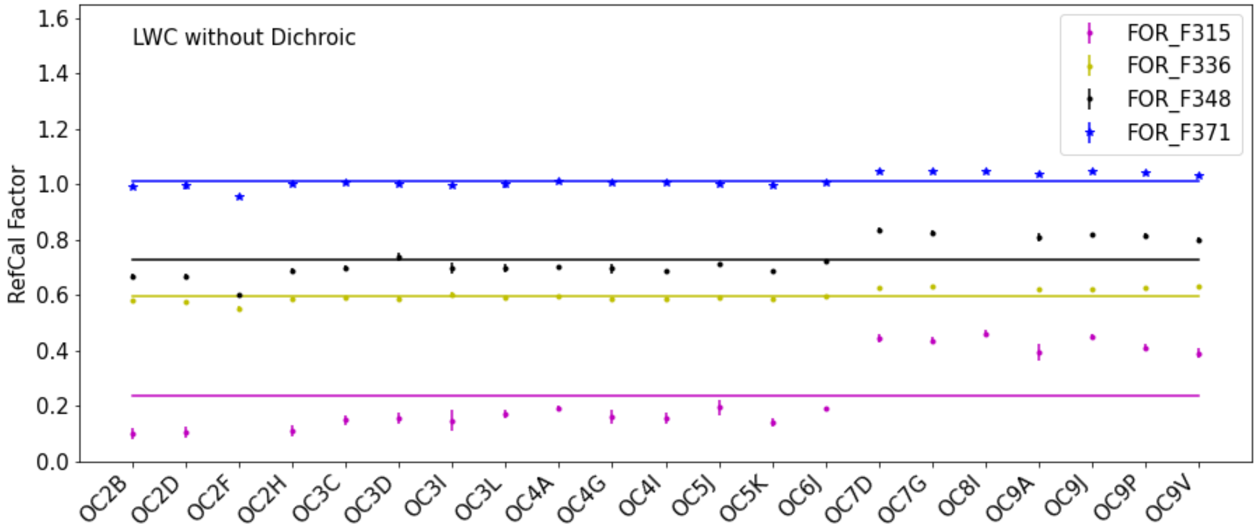

Figure 13 *Same as Figure 12, but for a different set of Long Wavelength Camera filters.*

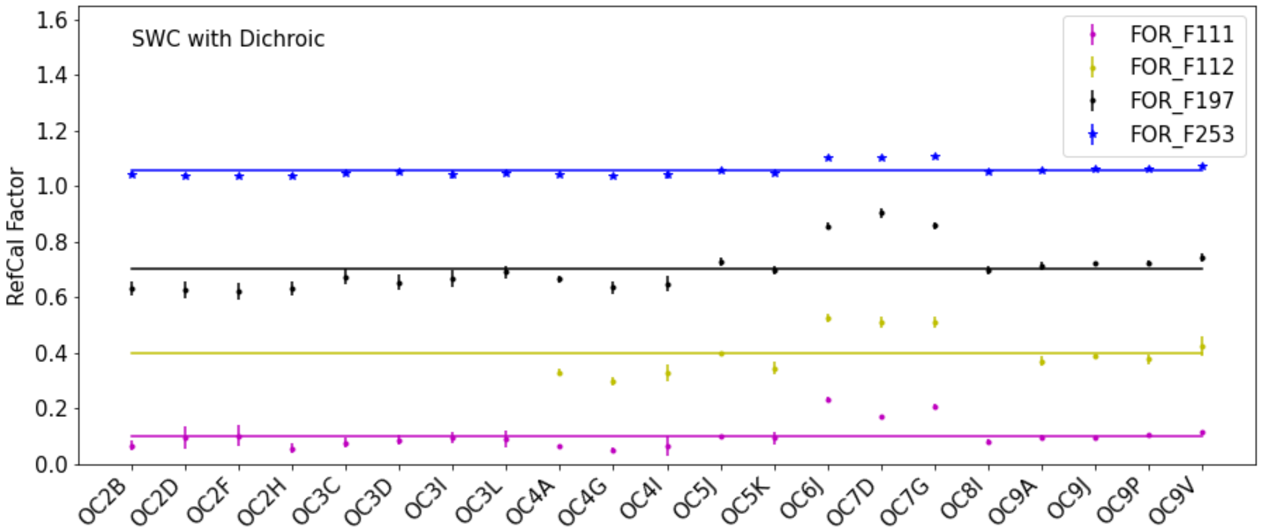

Figure 14 *Same as Figure 10 but for Short Wavelength Camera with dichroic.*

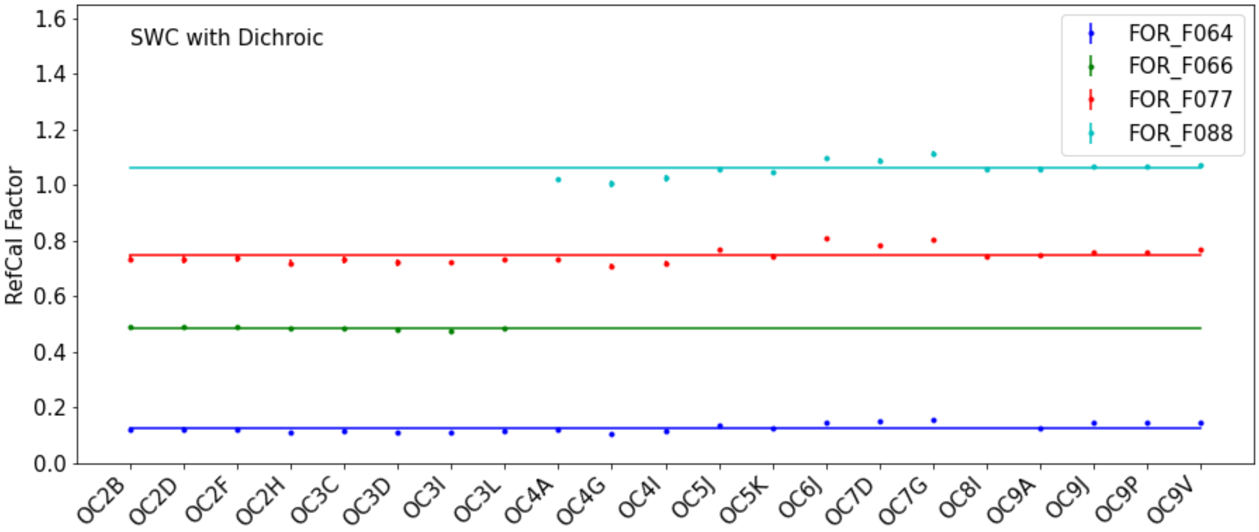

Figure 15 *Same as Figure 14 but for a different set of Short Wavelength Camera filters.*

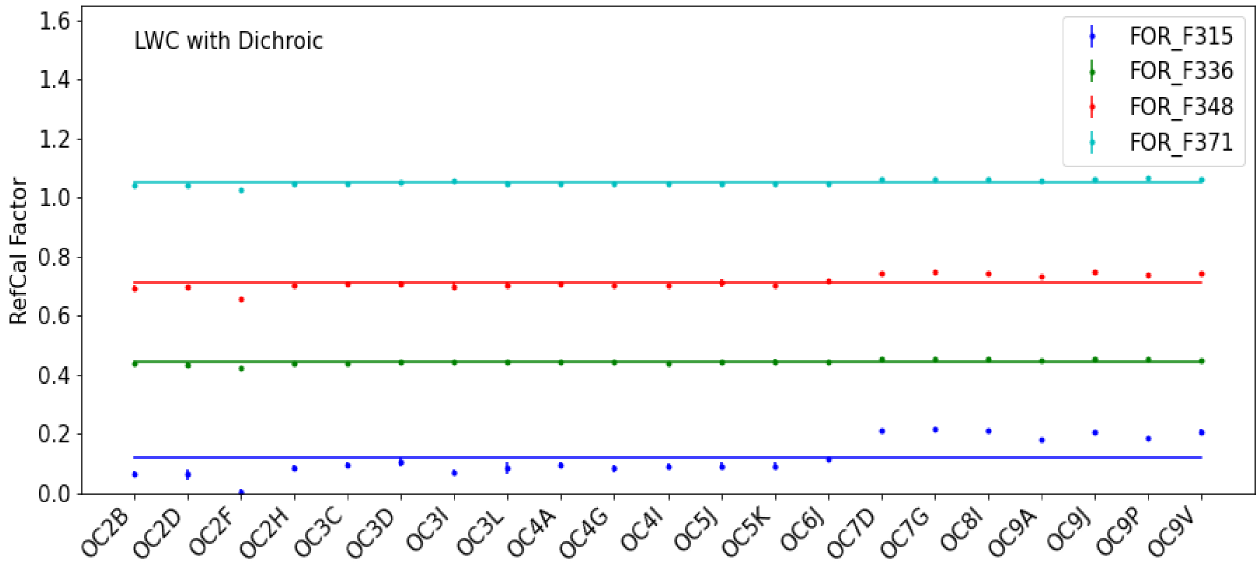

Figure 16 *Same as Figure 10 but for Long Wavelength Camera with dichroic.*

The following figures (Figure 17, Figure 18, Figure 19, and Figure 20) show the plots for percent difference between the reference calibration factor for a given series versus the average for all of the series (master). Here again the effects of changes in the entrance window on the reference calibration values can be clearly seen.

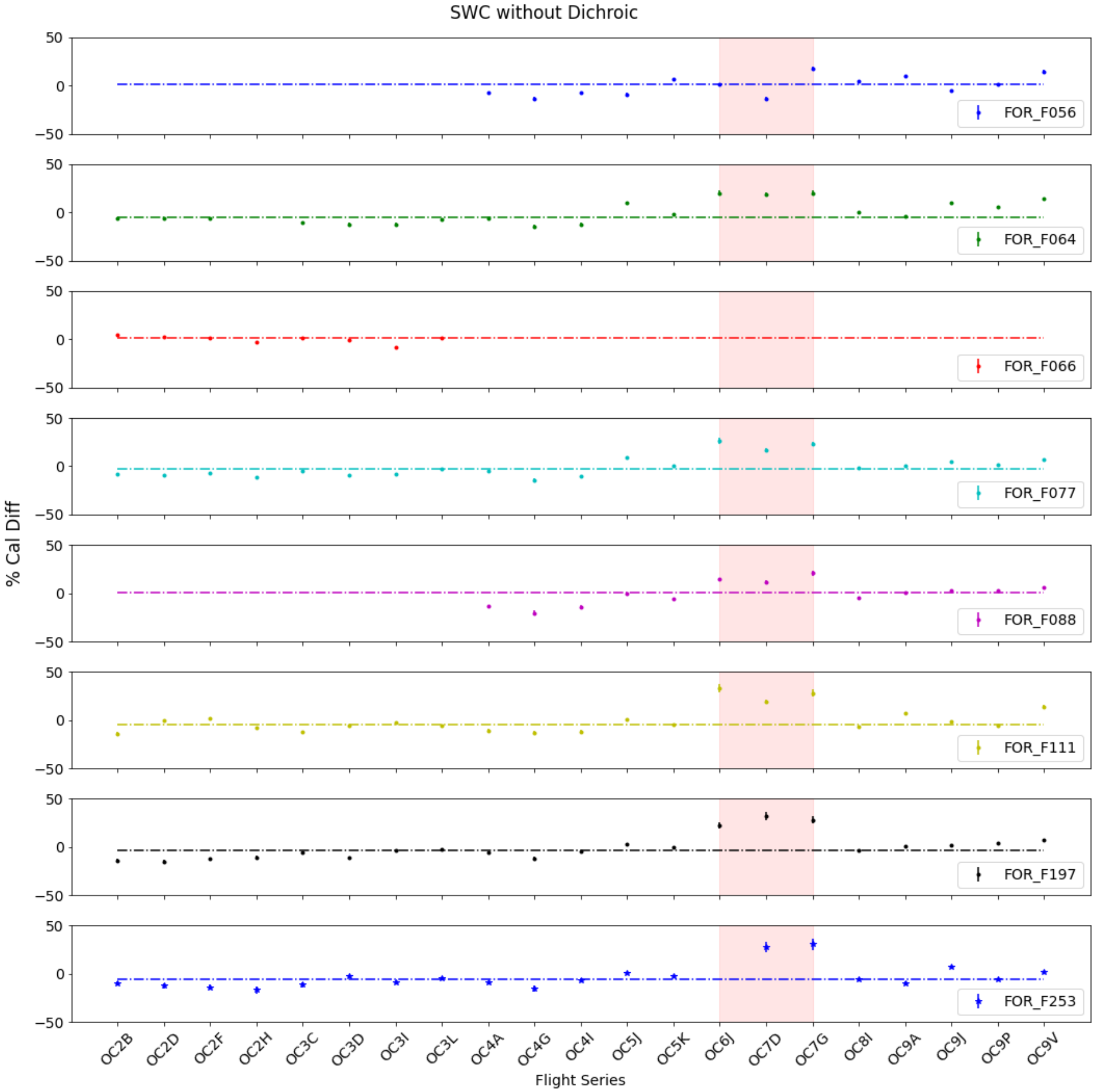

Figure 17 *Percentage calibration difference between the reference calibration factor for each of the SOFIA FORCAST series compared to the average of all reference calibration factors (master). The data is for observations in SWC without dichroic. The three off nominal cases are shown shaded in red.*

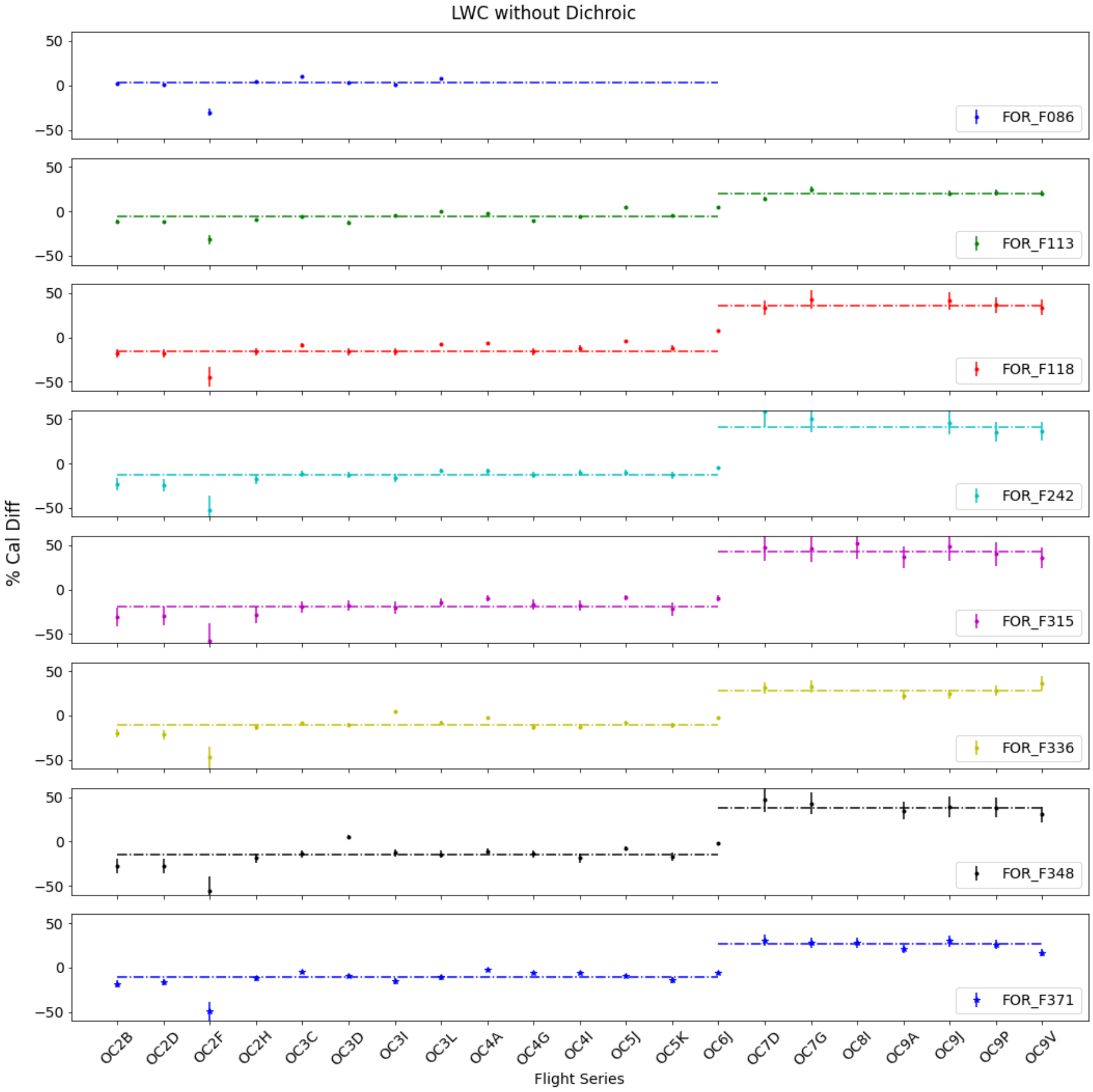

Figure 18 *Same as Figure 17 but for LWC.*

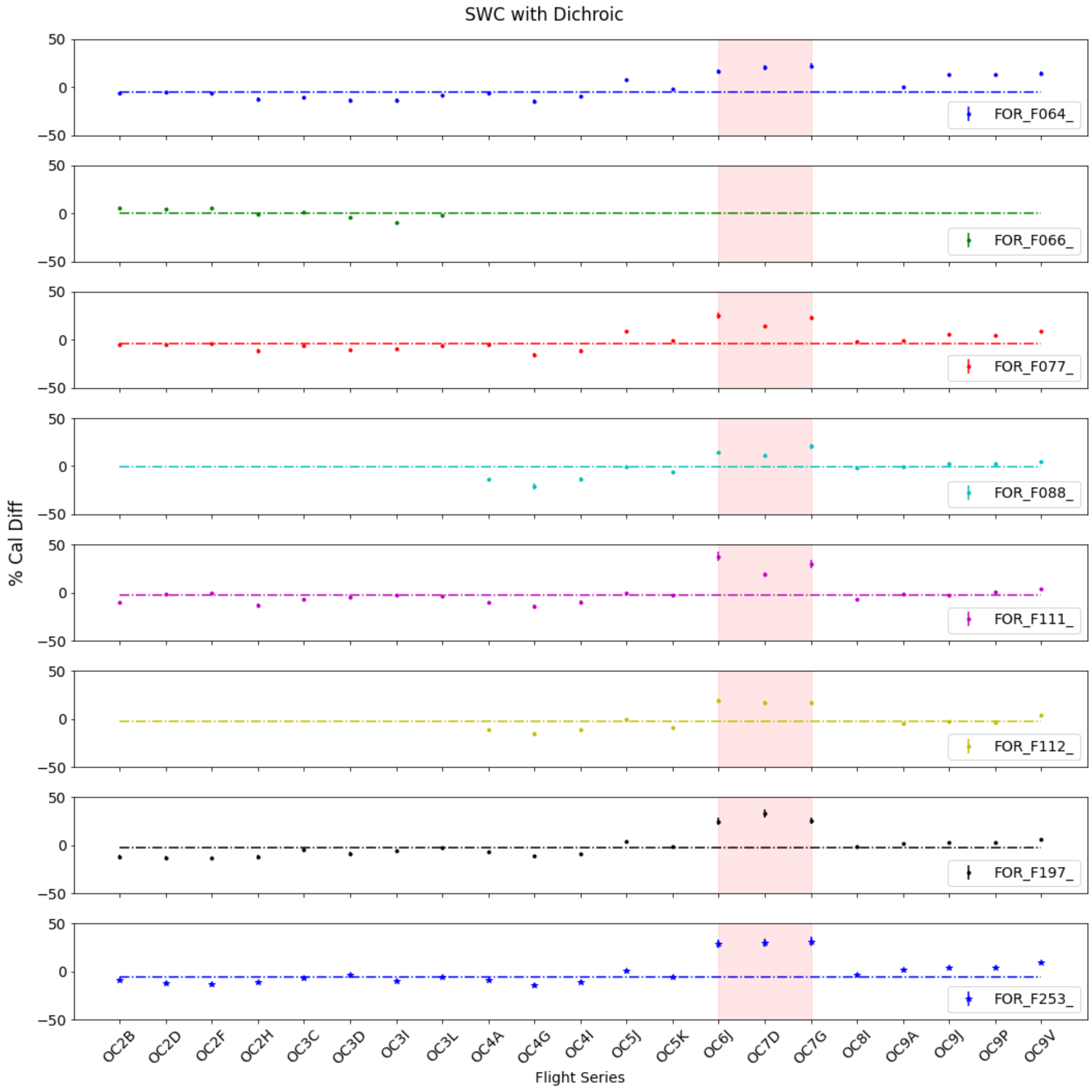

Figure 19 *Same as Figure 17 but for SWC with dichroic.*

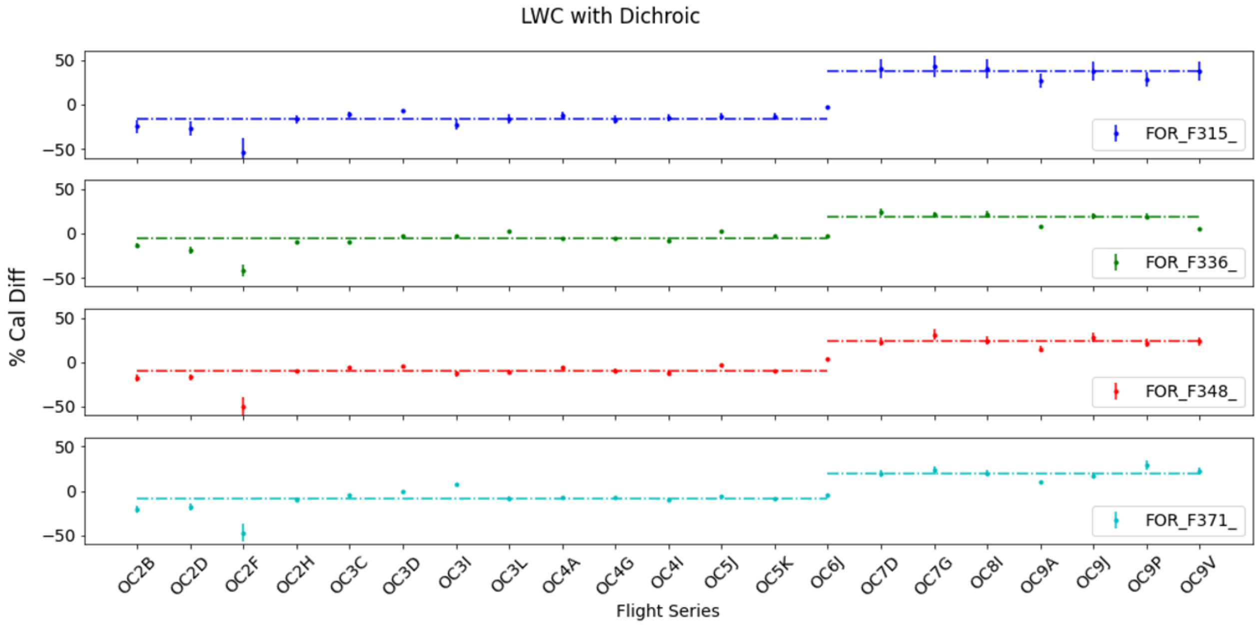

Figure 20 *Same as Figure 17 but for LWC with dichroic.*

3.5 GRISM WAVELENGTH CALIBRATION ACCURACY

A standard method of wavelength calibration in mid-infrared is observing well studied standards with strong emission lines (like planetary nebula) and comparing the lines in that spectrum with the target spectrum. The RMS (root mean square) in the residual peak position of the actual line versus those measured in the spectra can then be used to quantify the wavelength calibration accuracy of the instrument. Unfortunately for FORCAST, this method put a heavy burden on flight planning and significantly lowered the overall science efficiency of flights. Therefore, for FORCAST, grism wavelength calibration maps were derived from specialized sky data.

Wavelength calibration maps were derived from sky images (i.e., frames from the off-source chop-nod positions; see Appendix A) for which telluric absorption lines filled the whole image, from top to bottom, and were evenly spaced from left to right. Raw sky data were cleaned and summed to produce an image with a high signal-to-noise ratio in the telluric lines. After preprocessing, the strongest telluric lines were identified with specific wavelengths from a priori knowledge (ATRAN model), then they were re-identified with a centroiding algorithm at as many places across the array as possible. The identified positions were then fitted with a smooth 2D surface, which provided the wavelength value in microns at any pixel, accounting for any optical distortions as needed. The RMS in the residual peak position after fitting was found to be less than half a pixel which corresponds to 0.0058 µm. This was true for most of the grism and slit combinations except for G111 passband which does not contain strong telluric lines, and therefore the wavelength calibration accuracy in this passband will be larger.

For observed sources with strong emission lines, the lines in the data can be used to verify this result.

3.6 FIELD ORIENTATION / GRISM SLIT ROTATION ACCURACY

Since the instrument mounting flange on the SOFIA telescope had 24 fixed mounting bolts, the orientation of the FORCAST instrument was for all practical purposes the same each time it was installed on the telescope. However, the optical system as a whole (which included FORCAST) may have suffered from flexure or slight misalignments that may have caused slight distortion in the field that can be seen as a rotation from one observation to another. Furthermore, improper definition of the telescope boresight (i.e., optical axis) while observing (or as defined in the reduction software) may also have caused small errors in the rotation. This rotation error is very difficult to measure, as FORCAST rarely had complex fields with multiple stars which could be used to calculate any possible small rotations. In most cases when such fields have been observed, the rotation error measured is typically very close to zero (<0.5°), though the largest single variations ever measured have been +1.1° and -0.5°. Thus, a maximum deviation of the rotation of approximately ± 1° is estimated.

Since the SOFIA telescope was not an equatorially mounted telescope, the field of view during an observation rotated over time. Unlike many non-equatorial mounted telescopes, SOFIA did not have a field de-rotator either (and one was not built into FORCAST), and so this meant the angle of the slit on sky for spectroscopy could not be set at a desired angle, and therefore the slit orientation depended on where and when the object was observed. Thus, for any given Level 2 data product (i.e., a single FORCAST observation) the error in the known orientation of the slit on a source is the same as that of the field rotation given above (i.e., ± 1°). However, as a spectroscopic target was observed, the slit rotated on the source with a speed dependent on the sky rotation rate. This means that the final co-add of all Level 2 data into a final Level 3 spectrum may include data from many different slit orientations. Finally, the narrow 2.4″ slit in FORCAST was at a slight angle ~1.4° with respect to the y-axis of the arrays and slightly curved (see Figure 21). Any effects this may have had on the spectra are corrected in the FORCAST REDUX software.

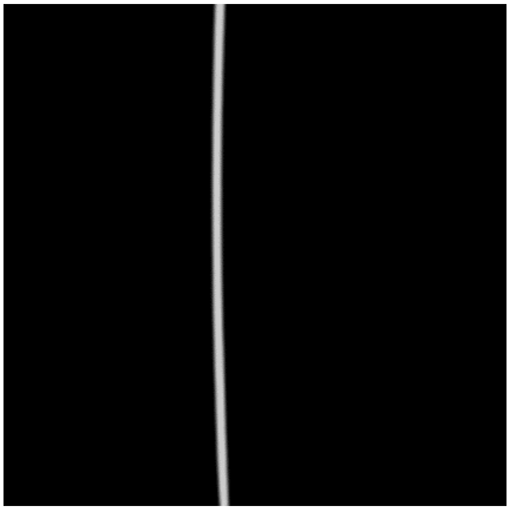

Figure 21 *Image of the 2.4" (LS_24) slit. The larger 4.7" (LS_47) slit has less noticeable curvature.*

3.7 ARRAY FLATNESS AND FLAT FIELDING

Flat-field frames are needed to permit correction for fixed-pattern noise in the array and large-scale distortions caused by various optical issues. The FORCAST array is not flat. Variations in the flux measured on a point source depending on its position on the array (especially toward the edges) can differ on scales of 10-15%. In the optical, flat fields are typically taken at the end of the night by observing either a screen mounted on the dome or the sky to provide uniform illumination on the detector. However, in the mid-infrared, dome flats are unusable, because the screen, which is a room temperature blackbody, will generally saturate a mid-IR detector through most passbands. Several methods for trying to create mid-infrared flat fields have been attempted from a multitude of instruments: CanariCam[1] on the GTC, T-ReCS on Gemini South, Michelle on Gemini North, and both OSCIR and TIMMI2[2] on multiple telescopes. None of these instruments/facilities were successful at creating usable flat-fields.

In theory, to create a mid-IR flat field at least two images with different levels of background illumination that differ from each other by a few percent would be needed. Subtracting the lower–background image from the higher-background image provides a map of the spatial variations in sensitivity of the pixels across the array. One method tested by the instrument groups listed above was to observe the sky at a low airmass and at a higher airmass. The background level increases with increasing zenith distance and atmospheric optical depth, which results in the images being taken at both a low and a high background. Another method tried was to take the flat field near in time and location to the science observation. This was done for CanariCam by use of a fore-optics assembly which contains a polystyrene filter to slightly increase the background. Michelle attempted to use the dark back of the tertiary mirror to take an image to have a slightly different background. All these methods had issues and, in most cases, increased the noise, resulting in overall worse data. Thus, it has been concluded that there was no reliable flat-field correction that can be used for these facilities/instruments.

Likewise, attempts were made to create flat-fields for FORCAST, using many similar methods described above, but none were successful. Therefore, FORCAST does not apply any flat-field corrections and there is a potential 10-15% flux variation across the array. For single compact objects, this effect is much less of an issue; compact objects were always placed to within a few pixels of the same location on the array and in the same place as the flux calibrators when they were observed. For extended sources, if dithers were used, this flux variation could also be averaged out.

Additionally, there is a low-frequency noise in some FORCAST data (mostly those data taken with the 19 µm filter, but occasionally in others) due to unknown reasons, but potentially related to poor chop-nod subtraction over such a relatively large field of view. This is discussed in detail in Section 4.5.1.7.

---

[1] Manual pg 9 http://www.gtc.iac.es/instruments/canaricam/media/cc_users_manual_20090423.pdf

[2] http://www.ls.eso.org/sci/facilities/lasilla/instruments/timmi/T2_Flats/timmi_flat.html

4. DATA

FORCAST data and format are described below. More information about the data format as well as specifics of the pipeline processing of the data can be found in the FORCAST Pipeline User's Manual, available at the SOFIA website at IRSA: FORCAST Pipeline User's Manual. All data taken in the C2N (NMC), C2NC2, and NXCAC modes are saved into Level 1 FITS data in four extensions. These four extensions generally refer to data taken in the four chop and nod positions of the telescope (see Appendix A), which are combined to create the final raw image. The basic format of the science data taken in the most common chop-nod configuration (i.e., NMC (C2N) mode) is shown below in Figure 22.

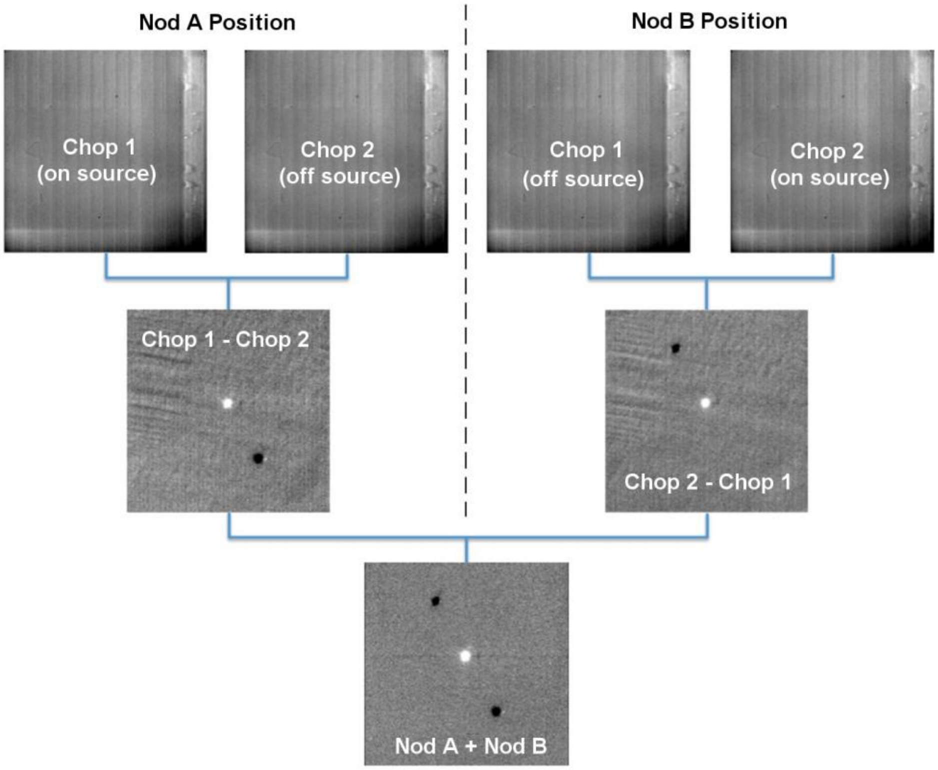

Figure 22 *The data contained in the four FORCAST extensions of Level 1 FITS data are displayed in the top row. These extensions correspond to the two secondary mirror positions (i.e., chop positions) and the two telescope pointing positions (i.e., nod positions). These frames in the upper row are: Nod A Chop1 (on source), Nod A Chop2 (off-source), Nod B Chop2 (off-source), Nod B Chop1 (on-source). The off-source chop image is also often referred to as a "sky frame" or "chop reference frame". The top row of images are dominated by the background from the sky and telescope and pixel offsets. The second row shows the chop-subtracted images (Chop 1 – Chop2 in the Nod A position, left, and Chop 2 – Chop 1 in the Nod B position, right). These middle two images show how chop subtraction removes the sky emission and pixel offsets but leaves the telescope emission artifacts sometimes called Nod noise (the high-frequency ripple across the array). The bottom image shows the final raw image which is an addition of the two images in the second row. The addition of the two middle row images removes the telescope emission artifacts.*

For standard stars, an additional step was taken to maximize signal-to-noise (S/N). The final raw image (like that at the bottom of Figure 22) was replicated twice but multiplied by –1.0. This made two additional images where the central instance of the source was negative, and the two formerly negative instances were positive. These negative images were shifted and added so that all three instances of the source could be coadded (see Figure 23).

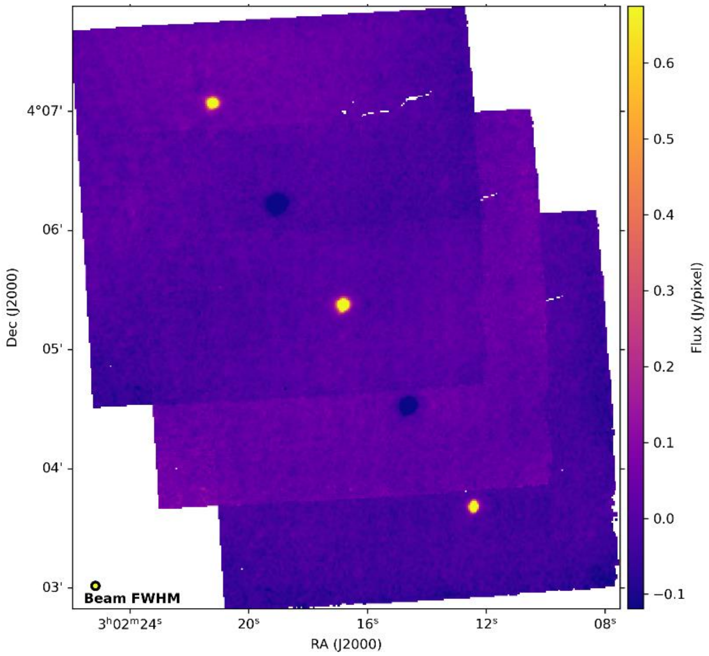

Figure 23 *For standard star calibrators the final image was shifted to add the negative beam on top of the positive beam to increase S/N slightly (<15%). Only the central of the now five instances of the source was used for flux calibration.*

For C2N (NMC) mode, the nodding sequence of the telescope was ABBA (for more see Appendix A); the first FITS image in an observation would consist of chopped data taken first in the telescope Nod A position followed by chopped data taken in the Nod B position. The next image would start with chopped data taken in the Nod B position first followed by chopped data taken in the Nod B position. If the observation required more observing time, this ABBA sequence would be repeated as necessary (e.g., ABBAABBA...).

C2NC2 raw data sets for imaging or NXCAC raw data sets for spectroscopy use a different nod sequencing pattern: ABA the first FITS image in an observation would consist of chopped data taken first in the telescope Nod A position followed by chopped data taken in the Nod B position. The next image would start with chopped data taken back in the Nod A position, but the data for the Nod B position in this second FITS image is the same as that taken in the first FITS image. In other words, both the first and second FITS image share the same Nod B data. If the observation required more observing time, this ABA sequence would be repeated as necessary (e.g., ABAABA...). Unlike C2N (NMC) data, only the Nod A position contained the source. The Nod B position was usually very far from the source and sampled only sky (see more in Appendix A). Additionally, for C2NC2 mode (but not NXCAC) the Nod A and B positions are always dithered (so the noise remains uncorrelated). If five FITS files were used in the observation, the nod sequence for C2NC2 would have been □1□1□2□3□2□4□5□3, where the off-source B nods are shared between some of the files and the numbers refer to the unique dither positions:

File 1 = □1□1

File 2 = □1□2

File 3 = □3□2

File 4 = □2□4

File 5 = □5□3

Again, for more information on chop-nod sequences and data format, please see the FORCAST Pipeline User’s Manual as well as Appendix A of this document.

4.1 PIPELINE UPDATES

The FORCAST REDUX data reduction pipeline software and the data products it creates have gone through several updates over time. In particular, the recent update to version 2.0.0 introduced some relatively large changes to the format of the data that may require updates to any local routines used to analyze the data.

Below is a table summarizing major changes by pipeline version. Dates refer to approximate release dates. Check the PIPEVERS key in FITS headers to confirm the version used to process the data, as some early data may have been reprocessed with later pipeline versions.

More detailed change notes are available in *Appendix D: Change notes for the FORCAST pipeline* in FORCAST Pipeline User’s Manual (FORCAST Pipeline User's Manual).

Table 11: Examples of Important FORCAST REDUX Pipeline Change Notes

Version	Date	Software/Cycle	Comments
<1.0.3	01/23/15	IDL:Cycle 1,2	Earliest FORCAST data where some modes were still being commissioned.
1.0.5	05/27/15	IDL:Cycle 3	TOTINT keyword added for comparison to requested/planned value in SITE (SOFIA Integration Time Estimator).
1.1.0	01/28/16	IDL:Cycle 4	Flux calibration factors are now applied to data arrays to convert them to physical units (Jy). The calibrated data product has file code CAL (PRODTYPE=calibrated). COA files are no longer designated Level 3, even if their headers contain calibration factors. Also border-padding around valid imaging data now has NaN value instead of 0.
1.1.3	09/20/16	IDL:Cycle 4/5	Update rotation of field to filter boresight rather than center of array; previous data may have had an offset in astrometry between different filters.

1.2.0	01/25/17	IDL:Cycle 4/5	Overall improvement to calibration. Updated to include TEL files which are similar to REG files with telluric corrections applied to each file. Final calibrated file CAL file is same as COA file but with calibration factor (CALFCTR) already applied. Improved telluric correction for FORCAST grism data.
1.3.0	04/24/17	IDL:Cycle 5	Pipeline begins support for FORCAST LEVEL 4 Imaging Mosaics. EXPOSURE map is now propagated in units of time (seconds) instead of number of exposures.
1.4.0	02/21/19	IDL: Cycle 6	Introduce support for grism, slit-scan observations. The output product is a spatial-spectral cube (file code SCB, PRODTYPE=speccube, PROCSTAT=LEVEL_4).
2.0.0	5/07/20	Python:Cycle 8/9	File format of FITS files for imaging updated from image cube to separate extensions. Extensions are now FLUX, ERROR, and EXPOSURE. ERROR now represents the standard deviation (sigma) rather than the variance (σ^2). Grism data formats also changed significantly. Grism images and spectra are stored in the same FITS file, under separate extensions. Final 1D spectra (CMB files, PRODTYPE=combined_spectrum) are still stored in the same format as before; the spectrum corresponds to the SPECTRAL_FLUX extension in the COA (PRODTYPE=coadded_spectrum) file.

4.2 DATA QUALITY

Data quality for FORCAST is recorded in the FITS keyword DATAQUAL and can contain the following values:

NOMINAL: No outstanding issues with processing, calibration, or observing conditions.
USABLE: Minor issue(s) with processing, calibration, or conditions, but should still be scientifically valid (perhaps with larger than usual uncertainties); see HISTORY records for details.
PROBLEM: Significant issue(s) encountered with processing, calibration, or observing conditions; may not be scientifically useful (depending on the application); see HISTORY records for details. In general, these cases are addressed through manual reprocessing before archiving and distribution.
FAIL: Data could not be processed successfully for some reason. These cases are rare and generally not archived or distributed to the GI but mentioned in emails and updates regarding program progress.

Any issues found in the data or during flight are recorded as QA Comments and emailed to the GI after processing and archiving. A permanent record of these comments is also directly recorded in the FITS files themselves. Check the FITS headers, near the bottom of the HISTORY section, under such titles as "Notes from quality analysis" or "QA COMMENTS".

4.3 DATA PRODUCTS AND NAMING CONVENTIONS

4.3.1 File Naming Conventions

Output files from SOFIA pipeline are named according to the following convention:

FILENAME = F[flight]_FO_IMA|GRI_AOR-ID_SPECTEL1|SPECTEL2_Code_FN1[-FN2].fits,

where *flight* is the SOFIA flight number, *FO* is the instrument identifier, *IMA* or *GRI* specifies that it is an imaging or grism file, *AOR-ID* is the AOR identifier for the observation, *SPECTEL1|SPECTEL2* is the keyword specifying the filter or grism used, *Code* is three letters identifying the product type (listed in Table 12 and Table 13), *FN1* is the file number corresponding to the input file. *FN1-FN2* is used if there are multiple input files for a single output file, where *FN1* is the file number of the first input file and *FN2* is the file number of the last input file.

4.3.2 Pipeline Products

The following tables list all intermediate products generated by the pipeline for imaging and grism modes, in the order in which they are produced. By default, for imaging, the undistorted, merged, telluric corrected, coadded, calibrated, and mosaic products are saved; for grism, the stacked, rectified image, merged spectrum, calibrated spectrum, coadded spectrum, and combined spectrum products are saved. For scientists, the imaging suffixes CAL and COA files and perhaps MOS file are most important. Early Cycles had only final coadds as COA where the calibration had to be applied manually from the headers by dividing by the CALFCTR. Later this was updated to CAL files which are the same as COA files with the calibration applied. Finally for LEVEL 4 data MOS files represented final calibrated mosaics of multiple images taken over several flights within a Cycle.

The final grism mode output product from the Combine Spectra or Combine Response steps are dependent on the input data: for INSTMODE=SLITSCAN, a spectral_cube product is produced instead of a coadded spectrum and combined spectrum; for OBSTYPE=STANDARD_TELLURIC, the instrument response is produced instead.

For most observation modes, the pipeline additionally produces an image in PNG format, intended to provide a quick-look preview of the data contained in the final product. These auxiliary products may be distributed to observers separately from the FITS file products.

Table 12: Intermediate Data products for Imaging Reductions

Step	Data type	PRODTYPE	PROCSTAT	Code	Saved	Extensions
Clean Images	2D image	cleaned	LEVEL_2	CLN	N	FLUX, ERROR
Correct Droop	2D image	drooped	LEVEL_2	DRP	N	FLUX, ERROR

Correct Nonlinearity	2D image	linearized	LEVEL_2	LNZ	N	FLUX, ERROR
Stack Chops/Nods	2D image	stacked	LEVEL_2	STK	N	FLUX, ERROR
Undistort	2D image	undistorted	LEVEL_2	UND	Y	FLUX, ERROR
Merge	2D image	merged	LEVEL_2	MRG	Y	FLUX, ERROR, EXPOSURE
Register	2D image	registered	LEVEL_2	REG	N	FLUX, ERROR, EXPOSURE
Telluric Correct	2D image	telluric_corrected	LEVEL_2	TEL	Y	FLUX, ERROR, EXPOSURE
Coadd	2D image	coadded	LEVEL_2	COA	Y	FLUX, ERROR, EXPOSURE
Flux Calibrate	2D image	calibrated	LEVEL_3	CAL	Y	FLUX, ERROR, EXPOSURE
Mosaic	2D image	mosaic	LEVEL_4	MOS	Y	FLUX, ERROR, EXPOSURE

Table 13: Intermediate Data Products for Spectroscopy Reduction

Step	Data type	PRODTYPE	PROCSTAT	Code	Saved	Extensions
Clean Images	2D spectral image	cleaned	LEVEL_2	CLN	N	FLUX, ERROR
Correct Droop	2D spectral image	drooped	LEVEL_2	DRP	N	FLUX, ERROR
Correct Nonlinearity	2D spectral image	linearized	LEVEL_2	LNZ	N	FLUX, ERROR
Stack Chops/Nods	2D spectral image	stacked	LEVEL_2	STK	Y	FLUX, ERROR
Make Profiles	2D spectral image	rectified_image	LEVEL_2	RIM	Y	FLUX, ERROR, BADMASK, WAVEPOS, SLITPOS, SPATIAL_MAP, SPATIAL_PROFILE
Locate Apertures	2D spectral image	apertures_located	LEVEL_2	LOC	N	FLUX, ERROR, BADMASK, WAVEPOS, SLITPOS, SPATIAL_MAP,

Step	Data type	PRODTYPE	PROCSTAT	Code	Saved	Extensions
						SPATIAL_PROFILE
Trace Continuum	2D spectral image	continuum_ traced	LEVEL_2	TRC	N	FLUX, ERROR, BADMASK, WAVEPOS, SLITPOS, SPATIAL_MAP, SPATIAL_PROFILE, APERTURE_TRACE
Set Apertures	2D spectral image	apertures_ set	LEVEL_2	APS	N	FLUX, ERROR, BADMASK, WAVEPOS, SLITPOS, SPATIAL_MAP, SPATIAL_PROFILE, APERTURE_TRACE, APERTURE_MASK
Subtract Background	2D spectral image	background_ subtracted	LEVEL_2	BGS	N	FLUX, ERROR, BADMASK, WAVEPOS, SLITPOS, SPATIAL_MAP, SPATIAL_PROFILE, APERTURE_TRACE, APERTURE_MASK
Extract Spectra	2D spectral image; 1D spectrum	spectra	LEVEL_2	SPM	N	FLUX, ERROR, BADMASK, WAVEPOS, SLITPOS, SPATIAL_MAP, SPATIAL_PROFILE, APERTURE_TRACE, APERTURE_MASK, SPECTRAL_FLUX, SPECTRAL_ERROR, TRANSMISSION
Merge Apertures	2D spectral image; 1D spectrum	merged_ spectrum	LEVEL_2	MGM	Y	FLUX, ERROR, BADMASK, WAVEPOS, SLITPOS, SPATIAL_MAP, SPATIAL_PROFILE, APERTURE_TRACE, APERTURE_MASK, SPECTRAL_FLUX, SPECTRAL_ERROR, TRANSMISSION
Calibrate Flux	2D spectral image; 1D spectrum	calibrated_ spectrum	LEVEL_3	CRM	Y	FLUX, ERROR, BADMASK, WAVEPOS, SLITPOS, SPATIAL_MAP, SPATIAL_PROFILE, APERTURE_TRACE,

Step	Data type	PRODTYPE	PROCSTAT	Code	Saved	Extensions
						APERTURE_MASK, SPECTRAL_FLUX, SPECTRAL_ERROR TRANSMISSION, RESPONSE, RESPONSE_ERROR
Combine Spectra	2D spectral image; 1D spectrum	coadded_ spectrum	LEVEL_3	COA	Y	FLUX, ERROR, EXPOSURE, WAVEPOS, SPECTRAL_FLUX, SPECTRAL_ERROR TRANSMISSION, RESPONSE
Combine Spectra	1D spectrum	combined_ spectrum	LEVEL_3	CMB	Y	FLUX
Combine Spectra	3D spectral cube	spectral_ cube	LEVEL_4	SCB	Y	FLUX, ERROR, EXPOSURE, WAVEPOS, TRANSMISSION, RESPONSE
Make Response	1D response spectrum	response_ spectrum	LEVEL_3	RSP	Y	FLUX
Combine Response	1D response spectrum	instrument_ response	LEVEL_4	IRS	Y	FLUX

4.4 FLUX CALIBRATION

This section describes the process for deriving imaging and spectral calibrations. For more information on flux calibration accuracy and the selection of flux calibrators, see Section 3.4.

4.4.1 Imaging

The reduction process, up through image coaddition, generates Level 2 images with data values in units of mega-electrons per second (Me/s). After Level 2 imaging products are generated, the pipeline derives the flux calibration factors (in units of Me/s/Jy) and applies them to each image. The calibration factors are derived for each FORCAST filter configuration (filter and dichroic) from observations of calibrator stars.

After the calibration factors have been derived, the coadded flux is divided by the appropriate factor to produce the Level 3 calibrated data file, with flux in units of Jy/pixel. The value used is stored in the FITS keyword CALFCTR.

The calibration is carried out in several steps. The first step consists of measuring the photometry of all the standard stars for a specific mission or flight series, after the images have been corrected for the atmospheric transmission relative to that for a reference altitude and zenith angle. The atmospheric transmission in each filter has been computed using the ATRAN code (Lord 1992) for a range of observatory altitudes (corresponding to a range of overhead precipitable water vapor values) and telescope elevations. The ratio of the transmission at each altitude and zenith angle relative to that at the reference altitude (41,000 feet) and zenith angle (45°) has been calculated for each filter and fit with a low order polynomial. The ratio appropriate for the altitude and zenith angle of each observation is calculated and applied to each image.

The pipeline performs aperture photometry on the reduced Level 2 images of the standard stars after the registration stage using a photometric aperture radius of 12 pixels (about 9.2″ for FORCAST). The telluric-corrected photometry of the standard star is related to the measured photometry of the star via

$$N_e^{std,corr} = N_e^{std} \frac{R_\lambda^{ref}}{R_\lambda^{std}}$$

where the ratio $R_\lambda^{ref}/R_\lambda^{std}$ accounts for differences in system response (atmospheric transmission) between the actual observations and those for the reference altitude of 41,000 feet and a telescope elevation of 45∘. Similarly, for the science target, we have

$$N_e^{obj,corr} = N_e^{obj} \frac{R_\lambda^{ref}}{R_\lambda^{obj}}$$

Calibration factors (in Me/s/Jy) for each filter are then derived from the measured photometry (in Me/s) and the known fluxes of the standards (in Jy) in each filter. These predicted fluxes were computed by multiplying a model stellar spectrum by the overall filter + instrument + telescope + atmosphere (at the reference altitude and zenith angle) response curve and integrating over the filter passband to compute the mean flux in the band. The adopted filter throughput curves (available at the IRSA FORCAST website) are those provided by the vendor or measured by the FORCAST team, modified to remove regions (around 6-7 µm and 15 µm) where the values were contaminated by noise. The instrument throughput is calculated by multiplying the transmission curves of the entrance window, dichroic, internal blockers, and mirrors, and the detector quantum efficiency. The telescope throughput value is assumed to be constant (85%) across the entire FORCAST wavelength range.

For most of the standard stars, the adopted stellar models were obtained from the *Herschel* calibration group and consist of high-resolution theoretical spectra, generated from the MARCS models (Gustafsson et al. 1975, Plez et al. 1992), scaled to match absolutely calibrated observational fluxes (Dehaes et al. 2011). For β UMi, the model was scaled by a factor of 1.18 in agreement with the results of the *Herschel* calibration group (J. Blommaert, private communication; the newer version of the model from the *Herschel* group has incorporated this factor).

The calibration factor, C, is computed from

$$C = \frac{N_e^{std,corr}}{F_\nu^{nom,std}\left(\lambda_{ref}\right)} = \frac{N_e^{std,corr}}{\langle F_\nu^{std}\rangle} \frac{\lambda_{piv}^2}{\langle\lambda\rangle\lambda_{ref}}$$

with an uncertainty given by

$$\left(\frac{\sigma_C}{C}\right)^2 = \left(\frac{\sigma_{N_e^{std}}}{N_e^{std}}\right)^2 + \left(\frac{N_{\langle F_\nu^{std}\rangle}}{\langle F_\nu^{std}\rangle}\right)^2$$

Here, λ_{piv} is the pivot wavelength of the filter, and $\langle\lambda\rangle$ is the mean wavelength of the filter. The calibration factor refers to a nominal flat spectrum source at the reference wavelength λ_{ref}.

Since the predicted fluxes of standards used to derive the calibration factors are tied to the atmospheric response curves at reference altitude (41,000 ft) and zenith angle (45°), the derived calibration factor is called the reference calibration factor. The reference calibration factors derived from each standard for each filter are then averaged. The pipeline inserts this value (REFCALFC) and its associated uncertainty (REFCALER) into the headers of the Level 2 data files for the flux standards and uses the value to produce calibrated flux standards. The final step involves examining the calibration values and ensuring that the values are consistent. Outlier values may come from bad observations of a standard star; these values are removed to produce a robust average of the calibration factor across the flight series. The resulting average values are then used to calibrate the observations of the science targets.

Using the telluric-corrected photometry of the standard, $N_e^{std,corr}$ (in Me/s), and the predicted mean fluxes of the standards in each filter, $\langle F_\nu^{std}\rangle$ (in Jy), the flux of a target object is given by

$$F_\nu^{norm,obj}(\lambda_{ref}) = \frac{N_e^{obj,corr}}{C}$$

where $N_e^{obj,corr}$ is the telluric-corrected count rate in Me/s detected from the source, C is the calibration factor (Me/s/Jy), and $F_\nu^{norm,obj}(\lambda_{ref})$ is the flux in Jy of a nominal, flat spectrum source (for which $F_\nu \sim \nu^{-1}$) at a reference wavelength λ_{ref}.

The values of C, σ_c, and λ_{ref} are written into the headers of the calibrated (PROCSTAT=LEVEL_3) data as the keywords CALFCTR, ERRCALF, and LAMREF, respectively. The reference wavelength λ_{ref} for these observations was taken to be the mean wavelengths of the filters, $\langle\lambda\rangle$.

Note that σ_c, as stored in the ERRCALF value, is derived from the standard deviation of the calibration factors across multiple flights. These values are typically on the order of about 6% (see Herter et al. 2013). There is an additional systematic uncertainty on the stellar models, which is on the order of 5-10% (Dehaes et al. 2011).

4.4.1.1 Color Correction

An observer often wishes to determine the true flux of an object at the reference wavelength, $F_\nu^{obj}(\lambda_{ref})$, rather than the flux of an equivalent nominal, flat spectrum source. To do this, a color correction K is defined such that

$$K = \frac{F_\nu^{norm,obj}(\lambda_{ref})}{F_\nu^{obj}(\lambda_{ref})}$$

where $F_\nu^{norm,obj}(\lambda_{ref})$ is the flux density obtained by measurement on a data product. Divide the measured values by K to obtain the "true" flux density. In terms of the wavelengths defined above,

$$K = \frac{\langle \lambda \rangle \, \lambda_{ref}}{\lambda_{piv}^2} \frac{\langle F_\nu^{obj} \rangle}{F_\nu^{obj}(\lambda_{ref})}$$

For most filters and spectral shapes, the color corrections are small (<10%). Tables listing K values and filter wavelengths are available in the Appendix B for Cycles 4 to 9.

4.4.2 Grism

The common approach to characterizing atmospheric transmission for ground-based infrared spectroscopy is to obtain, for every science target, similar observations of a spectroscopic standard source with as close a match as possible in both airmass and time. Such an approach is not practical for airborne observations, as it imposes too heavy a burden on flight planning and significantly lowers the overall science efficiency of a flight. Therefore, a calibration plan is employed that incorporates a few observations of a calibration star per flight and a model of the atmospheric absorption for the approximate altitude and airmass (and precipitable water vapor, if known) at which the science objects were observed.

Instrumental response curves are generated from the extracted spectra of calibrator targets. For the G063 and G111 grisms, the calibrator targets comprise the set of standard stars and the associated stellar models provided by the *Herschel* Calibration program and used for the FORCAST photometric calibration. For the G227 and G329 grisms, the calibrator targets consist of bright asteroids. Blackbodies are fit to the calibrated broadband photometric observations of the asteroids, and these serve as models of the intrinsic asteroid spectra. In either case, the extracted spectra are corrected for telluric absorption using the ATRAN models corresponding to the altitude and zenith angle of the calibrator observations, smoothed to the nominal resolution for the grism/slit combination, and sampled at the observed spectral binning. The telluric-corrected spectra are then divided by the appropriate models to generate response curves (with units of Me/s/Jy at each wavelength) for the various grism+slit+channel combinations. The response curves derived from the various calibrators for each instrumental combination are then combined and smoothed to generate a set of master instrumental response curves. The statistical uncertainties on these response curves are on the order of 5-10%.

Spectra of science targets are first divided by the appropriate instrumental response curve, a process that yields spectra in physical units of Jy at each wavelength.

Telluric correction of FORCAST grism data for a science target is currently carried out in a multi-step process:

Telluric absorption models have been computed, using ATRAN, for the entire set of FORCAST grism passbands for every 1000 feet of altitude between 35K and 45K feet, for every 5° of zenith angle between 30 and 70°, and for a set of precipitable water vapor (PWV) values between 1 and 50 microns. These values span the allowed ranges of zenith angle, typical range of observing altitudes, and the expected range of PWV values for SOFIA observations. The spectra have been smoothed to the nominal resolution for the grism and slit combination and are resampled to the observed spectral binning.

If the spectrum of the science target has a signal-to-noise ratio greater than 10, the best estimate of the telluric absorption spectrum is derived in the following manner: under the assumption that the intrinsic low-resolution MIR spectrum of most targets can be well-represented by a smooth, low-order polynomial, the telluric spectrum that minimizes $\chi 2$ defined as

$$\chi_j^2 = \sum_i^n \left(F_i^{obj} - P_i T_i(PWV_j)\right)^2 \Big/ \sigma_i^2$$

is determined. Here F_i^{obj} is the response-corrected spectrum at each of the n wavelength points i, σ_i is the uncertainty at each point, P_i is the polynomial at each point, and T_i is the telluric spectrum corresponding to the precipitable water vapor value PWV_j. The telluric spectra used in the calculations are chosen from the pre-computed library generated with ATRAN. Only the subset of ATRAN model spectra corresponding, as close as possible, to the observing altitude and zenith angle, are considered in the calculation. The free parameters determined in this step are the coefficients of the polynomial and the PWV value, which then yields the best telluric correction spectrum. The uncertainty on the PWV value is estimated to be about 1-2 microns.

If the science target spectrum has a S/N less than 10, the closest telluric spectrum (in terms of altitude and airmass of the target observations) with the default PWV value from the ATRAN model is selected from the pre-computed library.

To account for any wavelength shifts between the models and the observations, an optimal shift is estimated by minimizing the residuals of the corrected spectrum, with respect to small relative wavelength shifts between the observed data and the telluric spectrum.

The wavelength-shifted observed spectrum is then divided by the smoothed and re-sampled telluric model. This then yields a telluric-corrected and flux calibrated spectrum.

Analysis of the calibrated spectra of observed standard stars indicates that the average RMS (Root Mean Square) deviation over the G063, G227, and G329 grism passbands between the calibrated spectra and the models is about 5%. For the G111 grism, the average RMS deviation is found to be on the order of about 10%; the larger deviation for this grism is due primarily to the highly variable ozone feature at 9.6 µm, which the ATRAN models are not able to reproduce accurately. The Level 3 data product for any grism includes the calibrated spectrum and an error spectrum incorporating these RMS values. The adopted telluric absorption model and the instrumental response functions are also provided.

As for any slit spectrograph, highly accurate absolute flux levels from FORCAST grism observations (for absolute spectrophotometry, for example) require additional photometric observations to correct the calibrated spectra for slit losses that can be variable (due to varying image quality) between the spectroscopic observations of the science target and the calibration standard.

4.5 KNOWN ARTIFACTS & MITIGATION

FORCAST data is known to have some artifacts that affect the data quality to varying degrees. They consist of three main categories: those inherent to the instrument (e.g.; detector noise), those that are a normal part of observing (e.g.; clouds, user error), and technical issues (e.g.; vignetting, window degradation). This section covers many of these issues, notes their severity, occurrence, and if the issue is fixable. Some of these issues are specific to certain flights and series while others are generalized to categories:

Often: Happened almost every flight

Common: Happened almost every flight series

Rare: Happened once every several flight series

Very Rare: Only happened perhaps once a year or less.

Note that these terms are for a general overview and specifics are discussed in the description below when possible. The quality assessment (QA) comments that can be found in the HISTORY of the .fits file should always be checked for exact information on any data issues.

4.5.1 Imaging Artifacts

4.5.1.1 First Frame Effect/ Van Gogh Noise

Occurrence: Often. This happens when the instrument switched from some filters to others and the background change causes this effect on the first readout frame. It is sometimes referred to as the Van Gogh effect in QA comments, as the dark regions are similar to the foreground tree in Van Gogh's *Starry Night* (Figure 24).

Significance: The effect is most obvious in bright standard star observations where multiple filters were observed in rapid order. Given the brightness of the standard stars and the location of the noise it had no effect on the calibration data. On fainter science data it also had no effect as it occurred in only the first frame and easily medianed/averaged out after observing a few frames. It also only affected the right and lower edge of the unrotated array, and compact sources were nominally set up to be near the center of the array.

Fix: None, as it has little to no effect on the data.

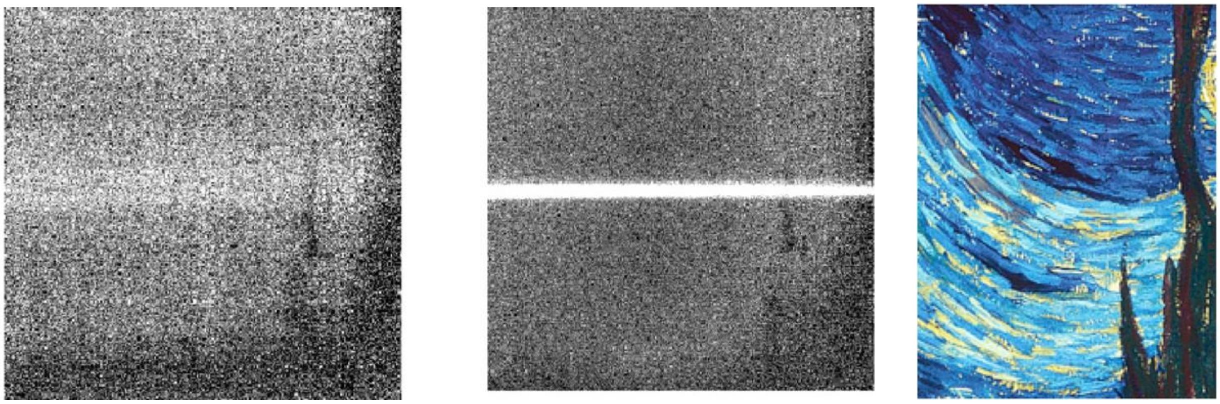

Figure 24 *Example of the effect in data imaging (Left) and spectroscopy (Middle) and a zoom in on Van Gogh's* Starry Night *(Right) showing why it is referred to as such.*

4.5.1.2 Crosstalk and Droop

Occurrence: Common. More often on bright standards.

Significance: The multiplexers used by FORCAST exhibited "droop" which caused the output voltages to sag when a signal was present (Figure 25). Also, like most mid-infrared detectors the array had issues with "crosstalk" which caused bright (or dark) pixels to echo through pixels sampled on the same output channel (Figure 26 and Figure 27). This effect is also sometimes referred to as ringing or "the hammer effect". Typically, this was only a small effect relative to calibration on bright standards or point sources <1-2%. It may be a problem if the effect was very bright or a bright source shared the frame with a faint source. In the case of a bright source near a faint source (or near extended emission) the array readout effects affected structure and flux measurements where they overlapped. In the very rare case of extremely bright targets (e.g., Jupiter, Eta Car, etc..) where the source might dominate over the background, the overall sensitivity of the array could be greatly suppressed by factors up to two or more.

Fix: None, as this is inherent of an array tuned to look at faint sources in general. It is seldom a problem except in rare cases of very bright targets or where faint extended emission was also nearby.

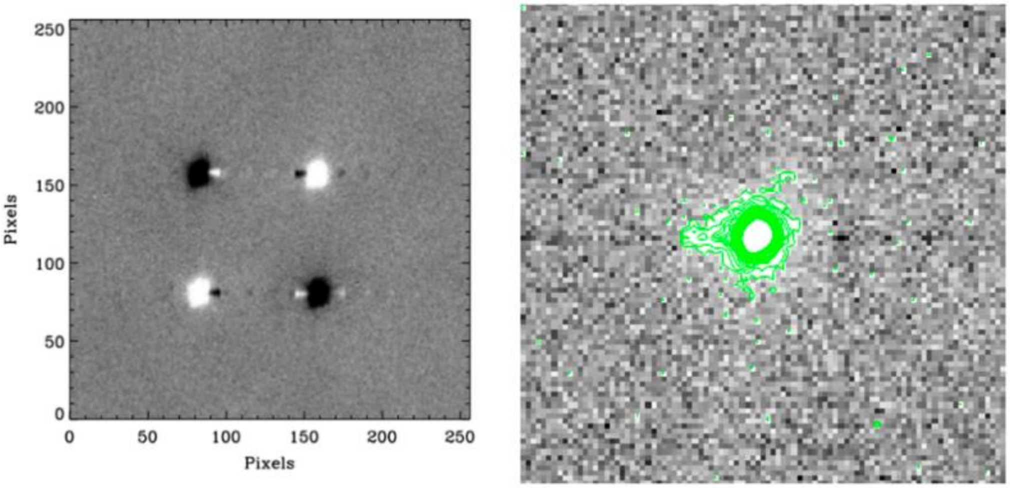

Figure 25 *Example of droop (Left) which can look similar to or be on top of crosstalk, but effects much closer to the source. (Right) Shows an overcorrection of the software of droop which can show a slight positive extension of the PSF. This overcorrection can occur slightly more often in the 8.6, 11.3, 11.8, 24.2 and 25.3 µm filters.*

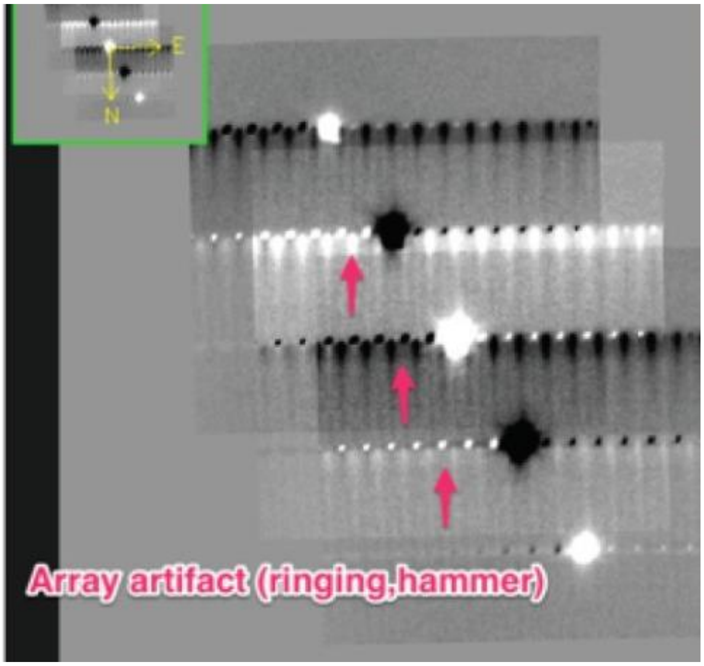

Figure 26 *Example of crosstalk.*

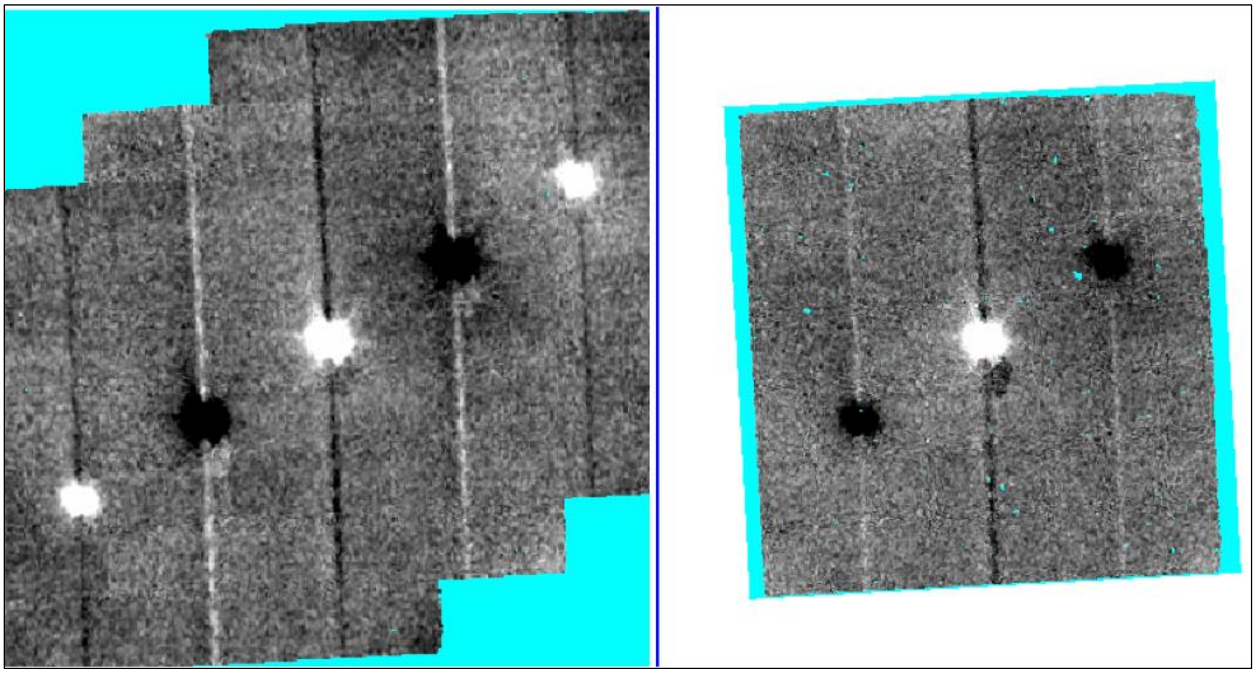

Figure 27 *Another example of crosstalk. This is always across the horizontal readout rows of the array (i.e., in the array coordinate frame), but appears vertical in this case due to this image being rotated to the proper sky position.*

4.5.1.3 Detector Bias

Occurrence: Only during parts of series OC2D and OC2F (FT 165-179)

Significance: The detector bias was normally set at distinct voltage values for both the SWC and LWC. In early flights these values were tuned to get the maximum response out of the detectors finalizing on values after Cycle 2 (of DETBIAS~1.7 for the SWC and ~1.2 for the LWC). However, during some flights in series OC2D and OC2F biases fluctuated in the LWC with values ~1.3 to 1.4 (Figure 28). Having the bias change during flights resulted in two conditions: the sensitivity/response of the detector changed, and mismatched bias level between standards and science sources made calibration impossible. Thus, some targets were not calibrated.

Fix: None. This was caught during post-processing, so calibration was done as best as possible. When looking at data from Flights 165 to 179, pay attention to the DETBIAS keywords and any notes in the HISTORY. Very early flights from Cycle 1 may have slightly different bias values but the main issue is consistency between standard calibrators and the science data, which was the problem on these flights.

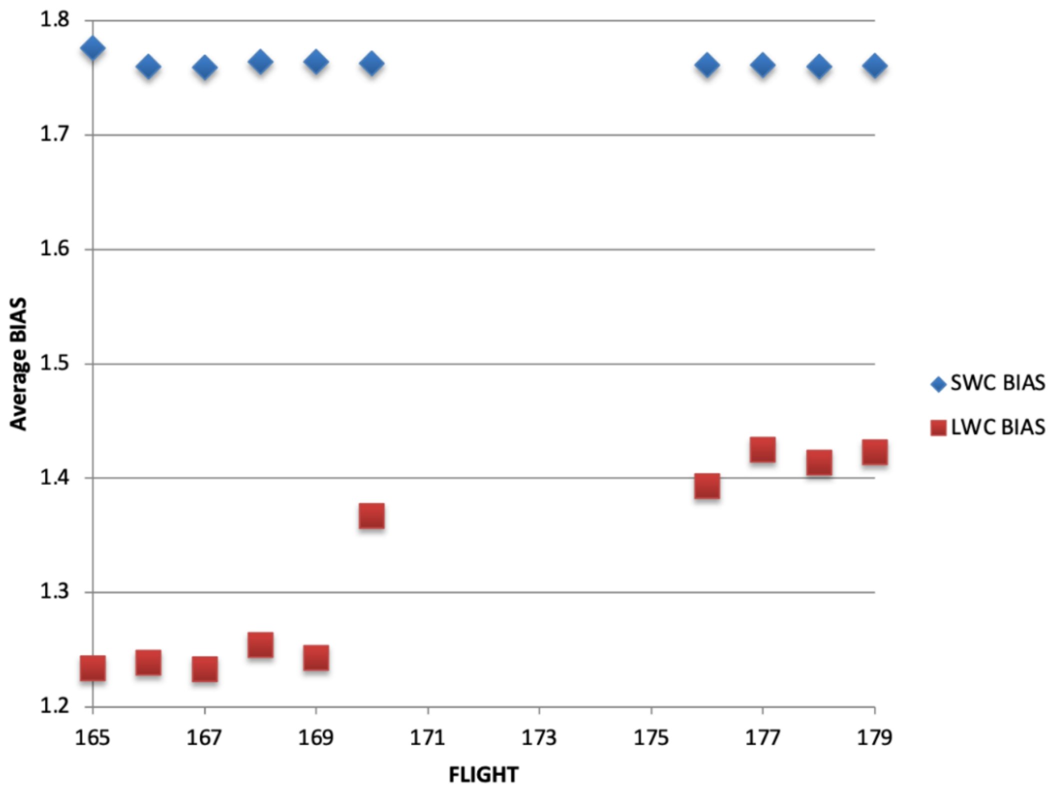

Figure 28 *Average BIAS voltage (DETBIAS) vs. Flight. Notice the large change for Flight 170 and beyond in the LWC.*

4.5.1.4 Saturation

Occurrence: Very Rare

Significance: Saturation is very rare on the FORCAST detector. There are only a few sources observed that have resulted in saturation, these being some of the brightest infrared targets in the sky (e.g., Eta Carinae, Jupiter, and the Moon; see Figure 29). In principle, the response of each of the pixels in the FORCAST detector arrays should be linear with incident flux. In practice, the degree to which the detector is linear depended on the level of charge in the wells relative to the saturation level. Response curves (response in analog-to-digital units, or ADU, as a function of well depth for varying background levels) have been measured that yield linearity correction factors. These multiplicative correction factors linearize the response for a much larger range of well depths (about 15% - 90% of saturation). In practical terms the background ADU of raw FORCAST frames can be examined. The full range runs between 0-16,000 ADU/pixel. Framerates/well depths are typically calculated to achieve about 6000-8000 ADU/pixel when observing. Issues and array effects only begin to arise roughly at values <2000 or >12,000 ADU/pixel. When this occurs, it will be noted in the HISTORY of the FITS files under QA comments and, as mentioned, will only happen on a few obvious bright targets or when mistakes in setup arise.

Fix: None, data will not be calibratable.

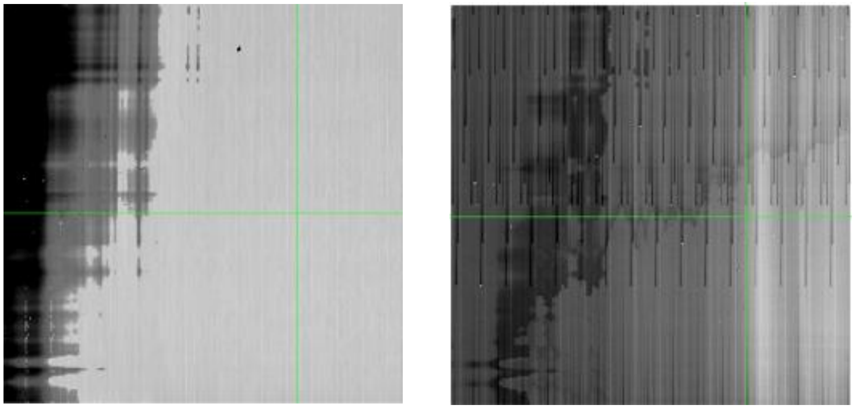

Figure 29 *Examples of fully saturated grism observations of the Moon that were erroneously taken with wrong frame times.*

4.5.1.5 Chop Smear

Occurrence: Very Rare.

Significance: This means timing was off while chopping and the instrument was taking data while the secondary mirror was still moving, potentially causing source elongations or trails in the chop direction (Figure 30). It happened often very early in FORCAST history (i.e., Cycle 1 in 2013) when the exact chop settle timing was being refined and happened occasionally when there were technical issues or very strong turbulence. The significance varies on the type of science being done. On a point source requiring only photometry a slightly larger aperture that includes the smear may be needed to recover all of the flux, but the science should not be affected. Even when the science goal was to resolve slightly extended emission in a source, the significance may not be much unless the expected angle of the intrinsic emission elongation is in the same direction as the chop angle.

Fix: None.

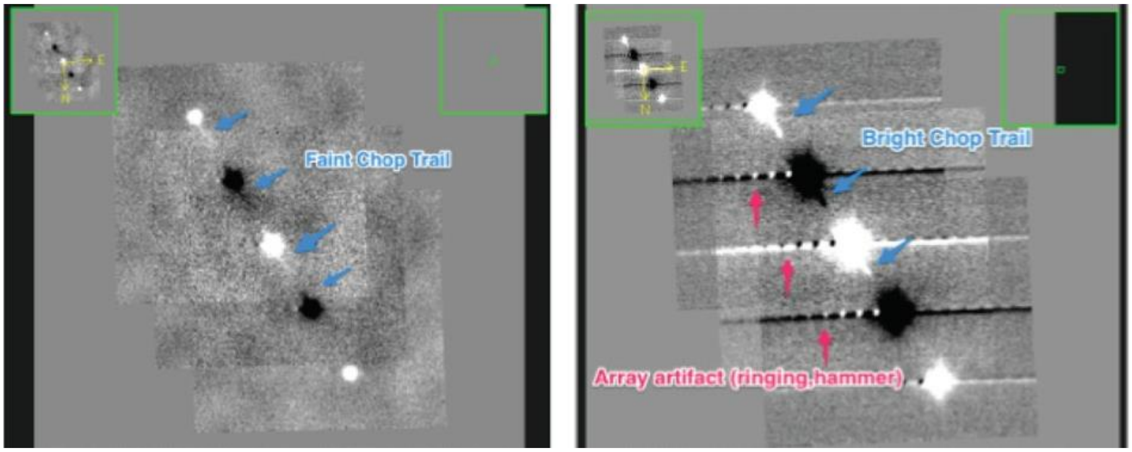

Figure 30 *Example of chop smear on a standard star which may not be obvious unless adjusting to see the background in better contrast. The chop smear may not be apparent when looking at the image with the default contrast (like when using SAO DS9 FITS viewer), however if the background is scaled properly the chop smear can be seen (Left). (Right) The smear is more obvious for brighter sources. Array crosstalk (a.k.a. ringing or hammer) can also be seen in this image (see Section 4.5.1.2).*

4.5.1.6 Large Chop

Occurrence: Occasionally in Cycles 1-4. Very rare in Cycles 6-9.

Significance: This only occurred in NMC mode (symmetric mode; see Appendix A). Since the mirror angles when chopping were symmetric about the optical axis, the target started to become distorted due to coma at large chop throws (e.g., mirror angles). In C2NC2 mode (asymmetric mode, see Appendix A), the on-source position of the mirror was always aligned with the optical axis, and the off-source mirror position was at a very large angle, but the data collected there was only used for background subtraction, and therefore any optical aberration had no effect on image quality. A chart showing the effect on image quality as a function of large chop throw is given in Section 3.1 (Figure 2). Large chops often are associated with large nods which also can cause Nod Misalignment issues (see Section 4.5.1.8), as these two phenomena are closely related.

Fix: None. For NMC data, look for the header keyword CHPAMP1, where the Chop Throw is 2 x CHPAMP1. Any values > 100"-120" begin to show noticeable coma.

4.5.1.7 Background Variability

Occurrence: Very often at 19.7 µm, common in other filters.

Significance: Even during clear conditions there can be some variability in the background which can be seen as large-scale (low spatial frequency) light and dark patches that vary from image to image (Figure 31). This is most prevalent in the 19.7 µm filter. These variations tend to even out to a flat background over large amounts of time (scales of 10-20 minutes), but can be seen as an uneven background in short exposures (<5-10minutes). If there are very strong (high amplitude) background variations, this may be due to clouds, but since it is often seen in almost all data at 19.7 µm, the background variability seems to be due to some other unknown phenomena. Increasing nod times or changing chop efficiencies had no effect. It is possible that the 19.7 µm filter in particular was picking up some extra atmospheric variability that had not been fully characterized (i.e., some highly variable telluric lines).

In addition, poor nod subtraction which showed mostly as diagonal high spatial frequency noise was also common in the 19.7 µm filter. This appeared as bands or cross-hatched bands of light and dark structures with peaks/troughs separated by 5-15 FORCAST pixels.

Fix: Possible fixes are described below.

This background variability occasionally can be modeled with a second or third order polynomial that can be subtracted off to leave a flat background, though this could affect the source emission if faint and extended.

The background can be improved by removing the individual files with significantly more variability than the other files from the final coadd. This should be done carefully, as removing too many or the wrong files causes an increase in an uneven background as there is now less data to average/median out over time. This is the step used in typical QA procedures as it is the easiest and least speculative method to remove a few bad files and improve the data. If this was done for a dataset it will be written in the QA comments in the HISTORY of the FITS file.

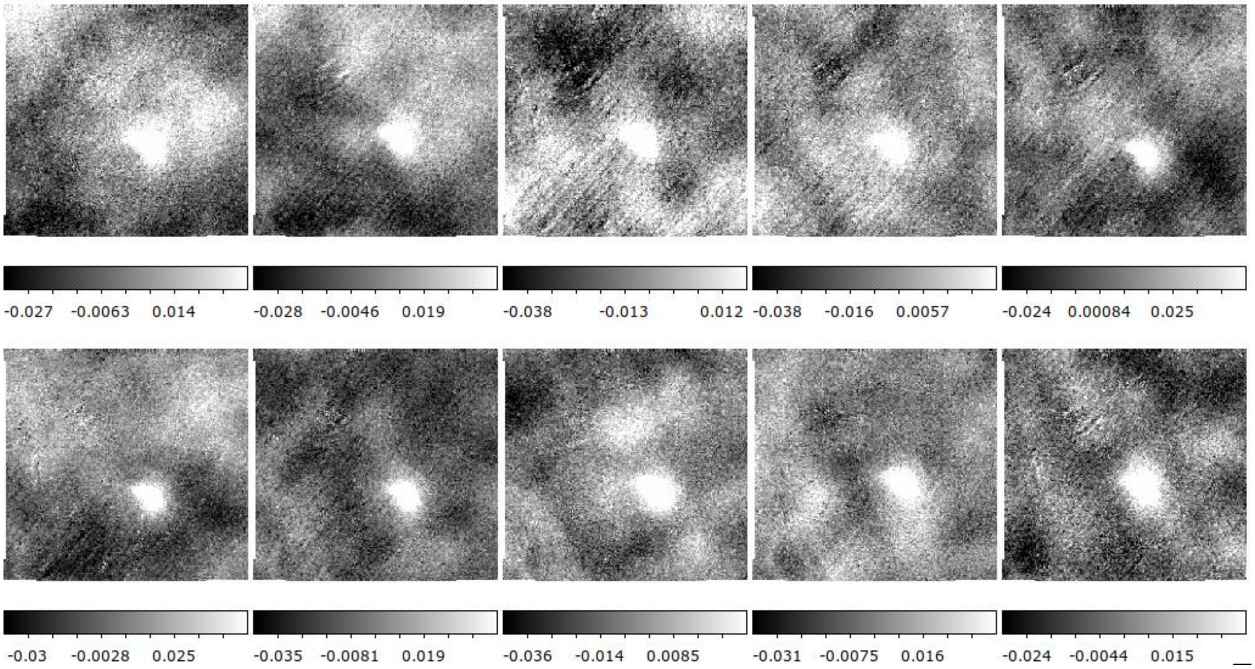

Figure 31 *Example showing several images taken in succession of an extended source. Notice how the background changes with low frequency bright and dark areas moving through the background. The higher frequency diagonal lines and structures seen are from the telescope emission due to poor nod subtraction.*

In the case of poor nod subtraction (high spatial frequency noise) using Fourier transforms to model and subtract may improve the overall background. An example of code produced by SOFIA for this can be found at (FORCAST-Periodic-Noise-Handling). However, one must note that the nod noise is not entirely diagonal and can be seen as curved in some part of the array. Therefore, though an improvement may be seen using the above code, a perfect subtraction is not possible (see Section 4.5.1.8 for other examples of nod noise).

4.5.1.8 Nod Misalignment

Occurrence: Occasionally in Cycle 3 and Cycle 4. OC5K however had a particular issue with this artifact. Very rare in Cycles 6-9. See Figure 32.

Significance: This typically occurred in cases of large nod throws (>100-120") in NMC mode (see Appendix A) when the telescope was not properly aligned. When this happened, the source observed in the two chop-beams did not align and when combined, resulting in anything from a slight elongation to double sources in the worst cases. This could also occur even in C2NC2 mode which could handle nod throws up to 1800″ easily, in the case where the nods were not properly aligned beforehand.

Fix: Correcting for this must be done on a case-by-case basis and is not done in normal processing. The three main fixes include:

1) Do Nothing: If the only concern is the flux of the target, then simply creating an aperture large enough to include all the flux from the elongated or peanut-shaped source will suffice.

Even in the worst case of a false double source, each will contain half the flux so enveloping both in an aperture will achieve the correct flux measurement (see Figure 33).

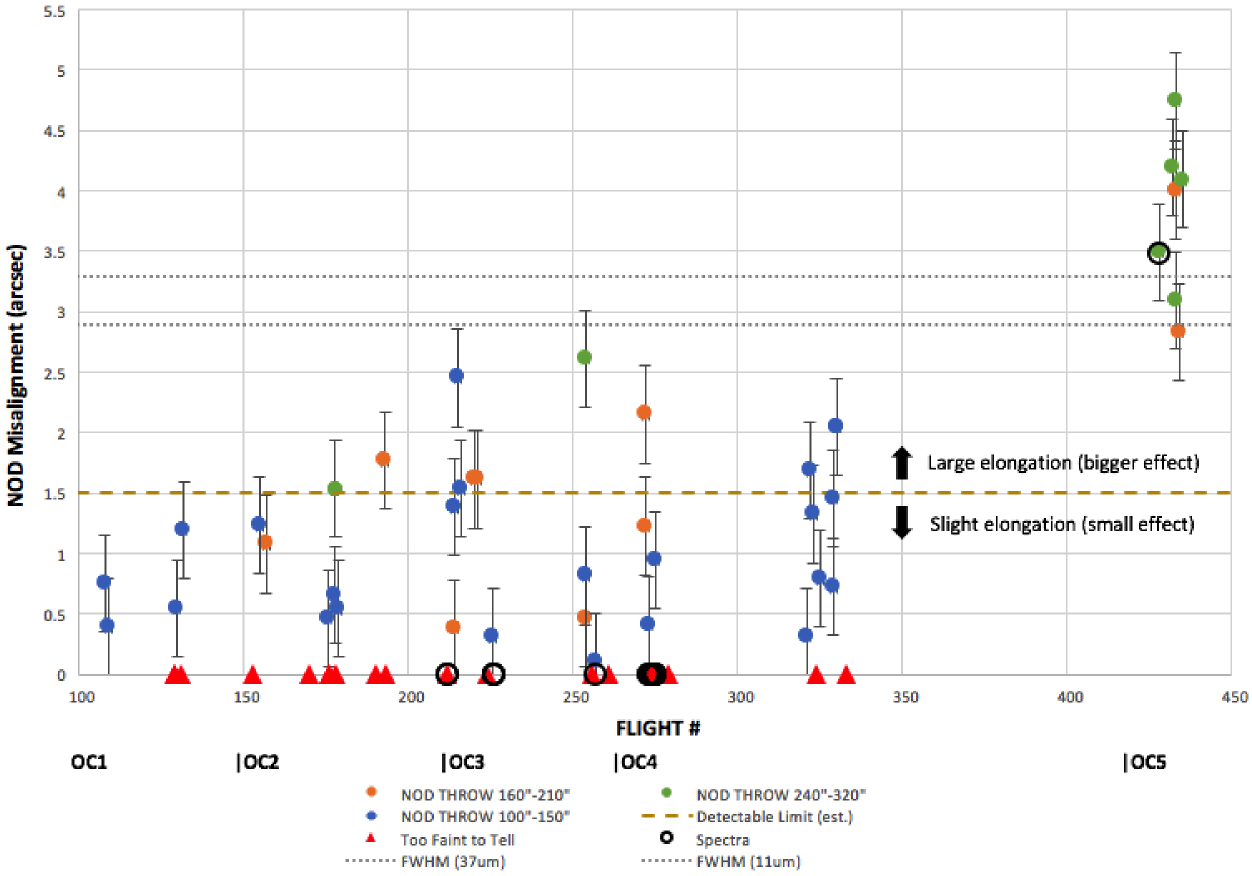

Figure 32 *Nod Misalignment in arcsec between Nod A and Nod B by flight/Series OC1-OC5. One FORCAST pixel is 0.768". Two FORCAST pixels (about 1.5") represent the approximate limit where the images become noticeably distorted and elongated in the final coadds (yellow dashed line). Error bars are +- about half a FORCAST pixel (0.4"). Colored circles represent Nod Throw length: Blue (100-150"). Orange (160-210"), Green (240-320"). This is also the same as the Chop Throw as all data was taken in NMC mode. Red Triangles represent observations that were too faint to measure in individual Nods. Black circles represent spectra which were assumed to have no issue as the corresponding acquisition image Nod misalignment was much less than the slit width. Dashed grey lines are the approximate FWHM range of FORCAST. Double sources are seen above this range.*

2) Shift Nods: If the source is bright enough to see in the individual nod frames then one nod can be shifted to align with the other. This should only be done in the case of very bright targets and will greatly increase the background. The image background will now look far less flat and look like images in Figure 34 or worse.

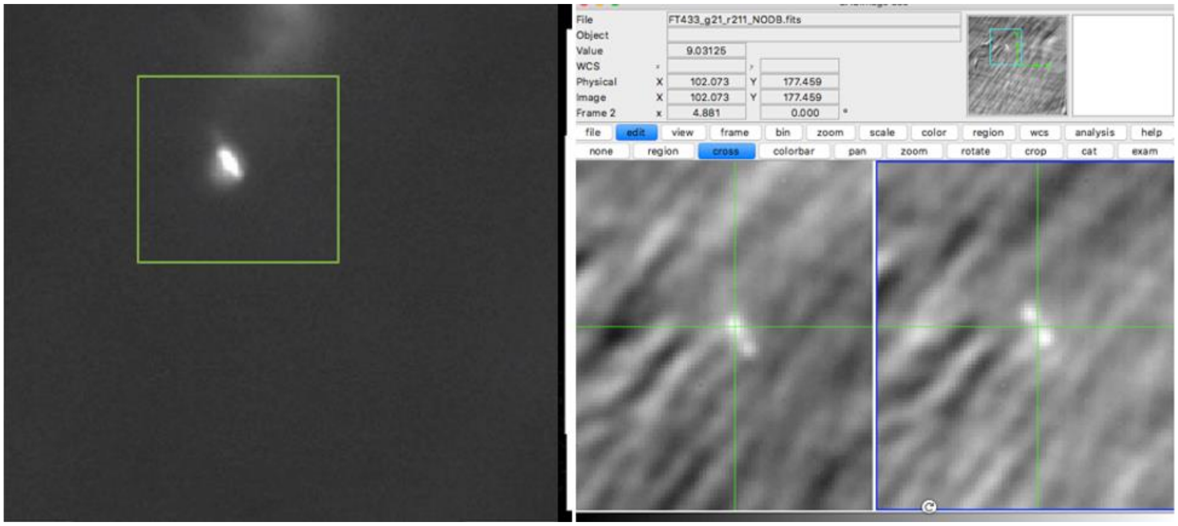

File FT433_g21_r211_NODB.fits
Object
Value 9.03125
WCS
Physical X 102.073 Y 177.459
Image X 102.073 Y 177.459
Frame 2 x 4.881 0.000 °

Figure 33 *(Left) Final image with an apparent elongated triple source. (Right) These two nod-only images (Nod A and Nod B) show that this is actually a double source that has misaligned nods (i.e., the green crosshair shows the same position in Nod A and Nod B) resulting in the false triple source seen on the left. This is an extreme case from OC5K showing a misalignment of 4 pixels (or 3.1"). Doing nothing but putting an aperture over the final image on the left will recover all the flux on the source though the actual morphology of the object will be incorrect.*

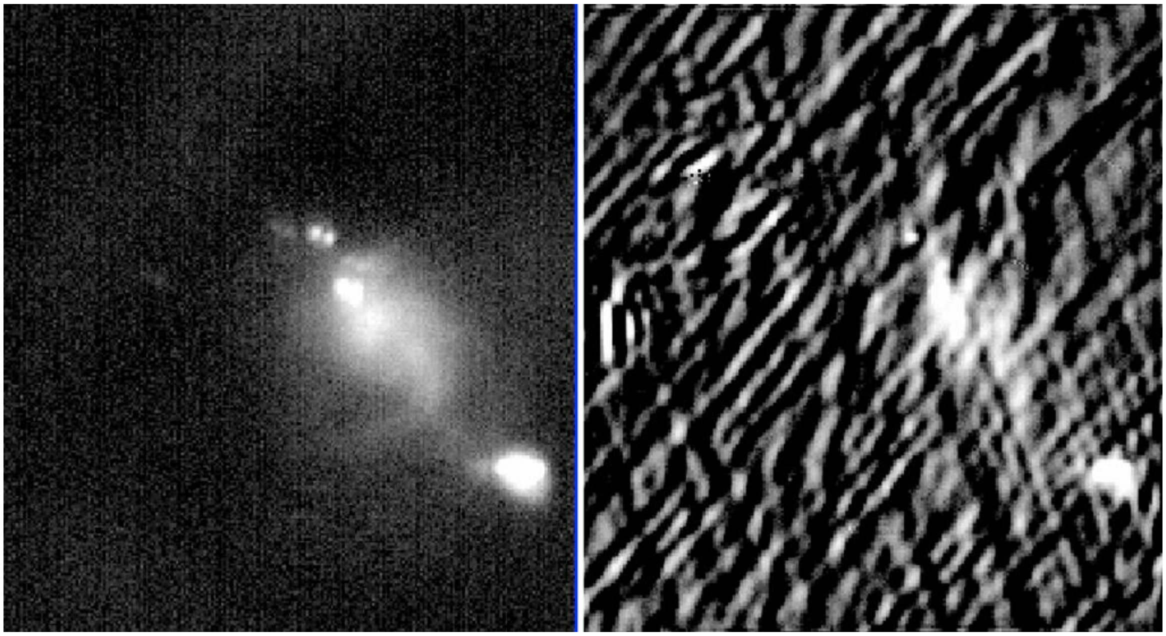

Figure 34 *(Left) A raw image with nod misalignment resulting in double sources. (Right) Image after the misalignment is removed by shifting the nod image pairs. The top source is now a single source but the misaligned nod (e.g., radiative offset) now dominates. The radiative offset (telescope emission) in FORCAST typically is a crosshatch pattern which can change in frequency based on zenith angle. In this case the target was not bright enough for this method to work.*

3) Deconvolve: If there is a known point source on the field (or the distorted PSF can be properly modeled), that can be used as a PSF to deconvolve the data and improve the image quality (see Figure 35).

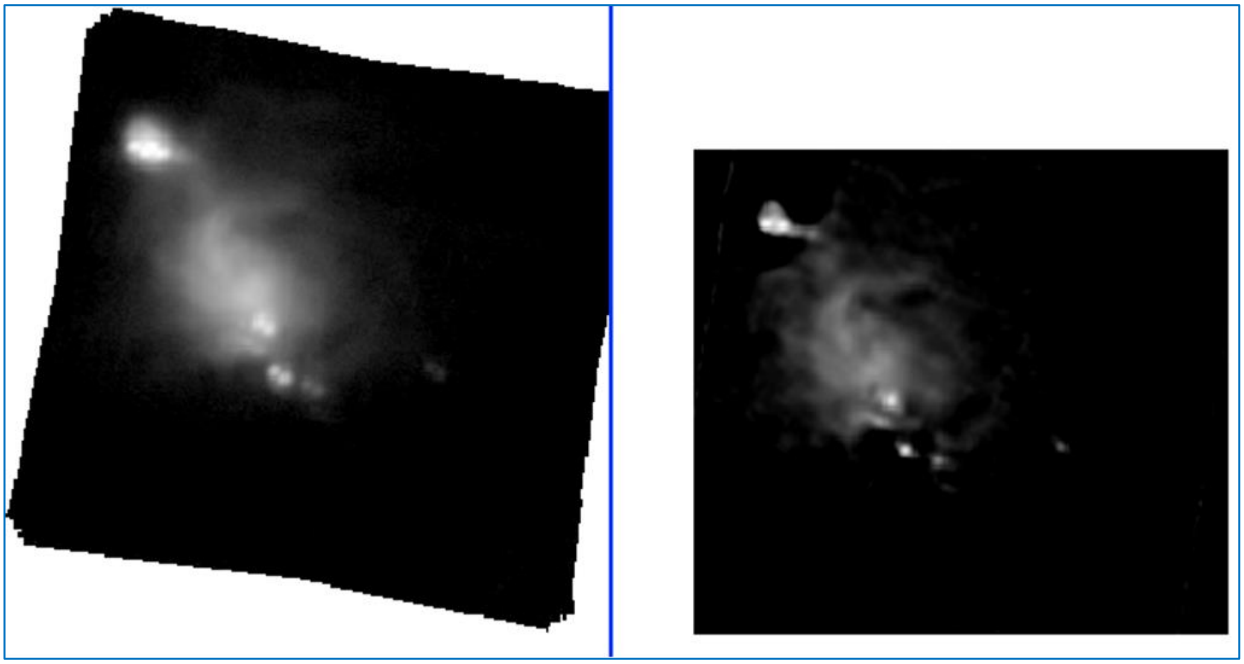

Figure 35 *(Left) A final CAL image with nod misalignment resulting in double sources (this is a rotated final version of the source in Figure 33). (Right) Image after deconvolution using the maximum likelihood method with 50 iterations using a model double PSF. This method appears more promising as double sources are now single sources. However, this was a quick reduction that still has some issues with the background and reproducing the proper fluxes. This method still may be the best alternative if done carefully.*

4.5.1.9 Dichroic Ghost at 11.2 µm

Occurrence: Always present for the 11.2 µm filter in dichroic mode.

Significance: When in single channel mode, there is no issue seen in the 11.2 µm filter. However, when 11.2 µm is used in dichroic mode, a ghost appears (Figure 36). This is primarily seen as a secondary source though for very bright targets even a tertiary ghost can be seen along the same angle. This ghost is very weak with a peak at 1-2% of the main flux peak. This filter was excluded for regular use because of this but brought back into service for some Cycles since it was the widest/most sensitive filter in the atmospheric window known as the “N-band” (8-13 µm). Thus, it was useful for detecting very faint sources where the ghost would not even be detectable.

Fix: There is no fix, this is just something to be aware of so there is no confusing this artifact with actual double sources. The effect on flux measurements is minor given that calibration uncertainty can be up to 10%.

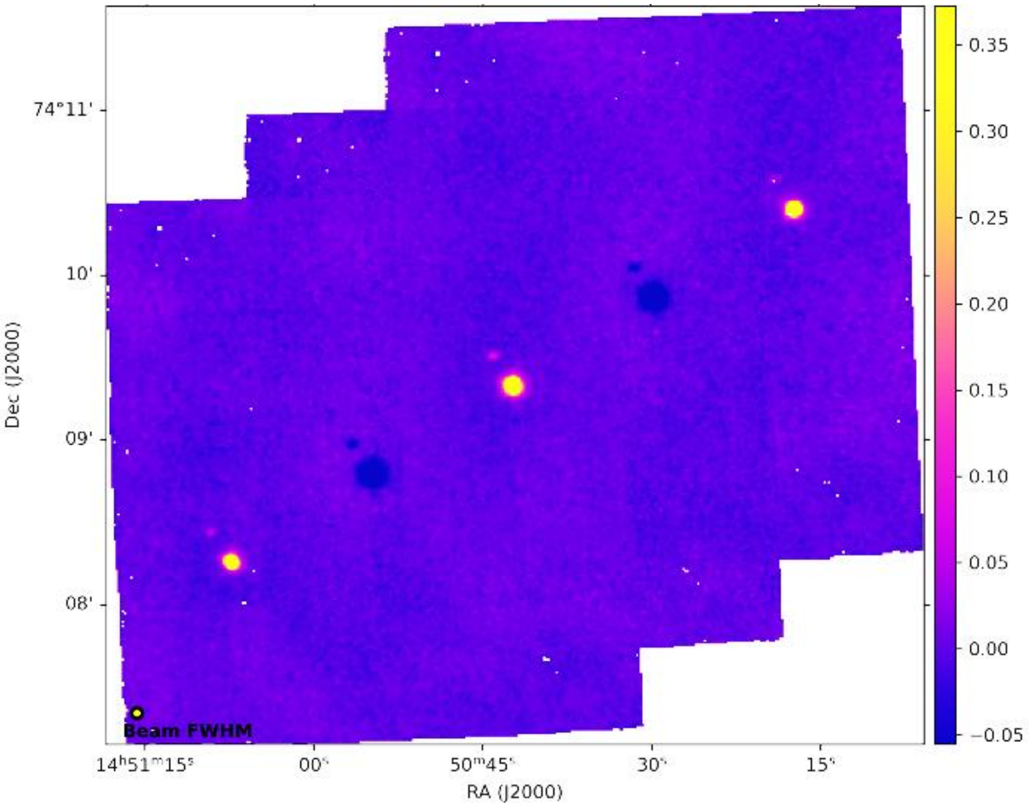

Figure 36 *Image of calibration star Beta Umi at 11.2 μm showing the faint ghost to the upper left of the central source.*

4.5.1.10 Vignetting

Occurrence: Common in Cycle 1 and 2, but Rare in later Cycles as flight/observing procedures were changed. Very Rare in Cycles 4-9.

Significance: The background becomes heavily unstable as the telescope begins to be occulted by the relatively warm top or bottom sides of the telescope cavity (Figure 37). This occurred at either high or low telescope zenith angles, where FITS keyword ZA_START or ZA_END <~32° or >~67° (Figure 38), though most often occurred at high zenith angles where observations at improved airmass conditions were prioritized. The exact zenith angle of the observation was dependent not only on the telescope zenith angle, but also on the direction and throw of the chop/nod setup (see Appendix A). This means for very large chop/nod throws that happen to also be predominantly in the telescope altitude direction, some observations could experience vignetting by the telescope cavity door even though the telescope zenith angle was in an acceptable range. With the telescope partially blocked from the sky, subtraction of the background became uneven resulting in high noise seen across the entire array in the SWC (Figure 39) and as a dark and/or bright edge region in the LWC (Figure 40).

Fix: There is no fix for the data, but in most cases, this occurred at the beginning or end of a leg. The typical fix performed during normal QA processing is the removal of the affected data from the final coadded image. In most cases this affects a small amount of data and does not significantly reduce the S/N.

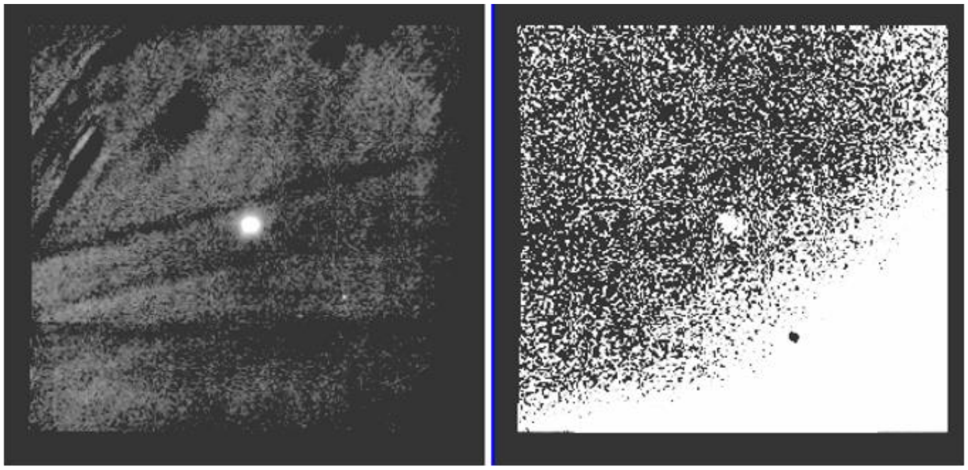

Figure 37 *An example of the vignetting effect on the standard star Alpha Boo. (Left) The SWC shows noise across the entire array similar to what is seen when clouds are present in the data. (Right) The LWC shows vignetting as a variable dark/bright region at the corner of the array that slowly covers the array as the vignetting gets worse.*

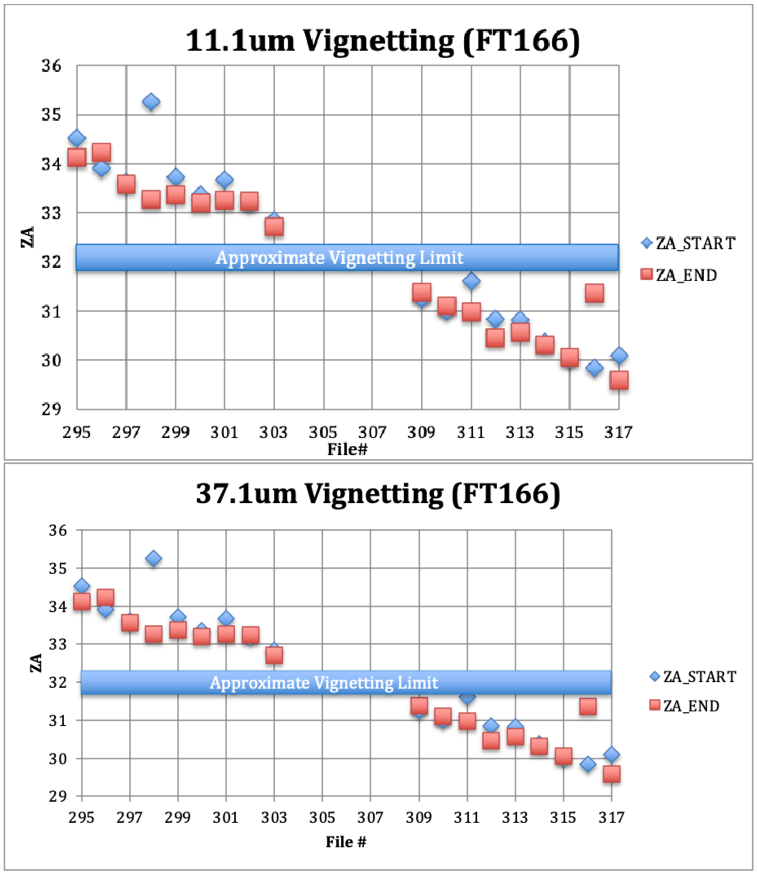

Figure 38 *Plots of the zenith angle header keywords (in the FORCAST FITS data) ZA_START, ZA_END vs file number for a set of observations of an IRAS object during Flight 166. File numbers 295-303 were taken above the vignetting limit of >~32°, while file numbers 309-317 are below. There was a pause in the observing between these two file ranges. As seen in the next two figures, the vignetting effects appeared on the array at both 11.1 µm (SWC) and 37 µm (LWC) since the data were taken simultaneously in dichroic mode.*

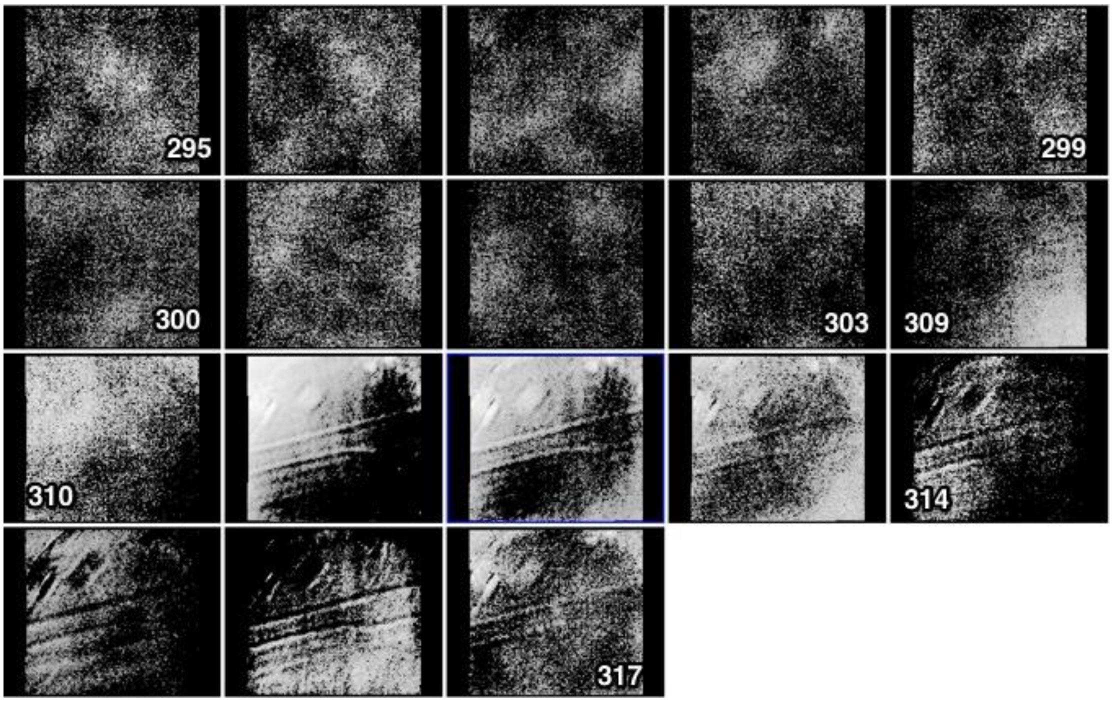

Figure 39 *The 11.1 µm images from Fight 166 (taken in dichroic mode with the 37.1 µm images below) in order from file number 295 to 303 and 309 to 317. The effects of vignetting can be seen starting at file 309 in the lower right corner of the array when ZA<32. With increasing file number the vignetting noise covers the entire array. The lines and structures seen are from the telescope emission due to poor nod subtraction.*

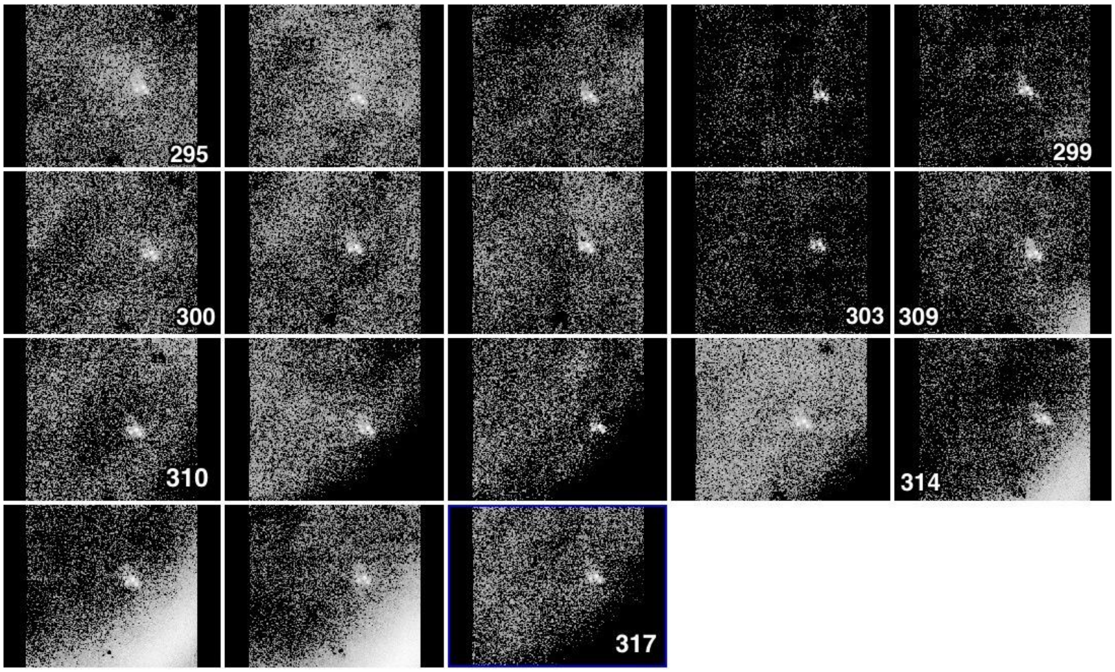

Figure 40 *Same as Figure 39, but for the 37.1 µm images. As in the 11.1 µm images above, the vignetting noise at the lower right corner appears at file number 309 when ZA<32 and slowly moves across the array. At this wavelength, however, the upper left of the array is less affected by the background instability caused by the vignetting.*

4.5.1.11 Clouds

Occurrence: Rare

Significance: Even at stratospheric altitudes clouds can occasionally be an issue. However, since FORCAST repeatedly took data on scales of minutes, if the clouds were transient during the leg, then files affected by clouds can be excluded from the final coadded data set. However, if the clouds were persistent there is not much to be done but analyze the severity of the contamination. Clouds will both attenuate the signal from the source while simultaneously increasing (and potentially saturating) the background, greatly affecting both source signal-to-noise and flux calibration.

Fix: In case of transient clouds, exclude affected data in final coadds. The best method for checking for contamination from clouds is using the FITS header keyword NLINSLEV which records the average background in ADU/pixel in each of the four chop/nod positions (i.e. Level 1 data extensions) of FORCAST data (see Figure 41 and Figure 42). Changes between background values in NLINSLEV in a single file >2% are usually indicative of cloud cover. This is more so in the SWC as the LWC can have higher variance. When at levels of 4-15%, however, cloud cover or some other technical issue is almost certainly taking place in the data.

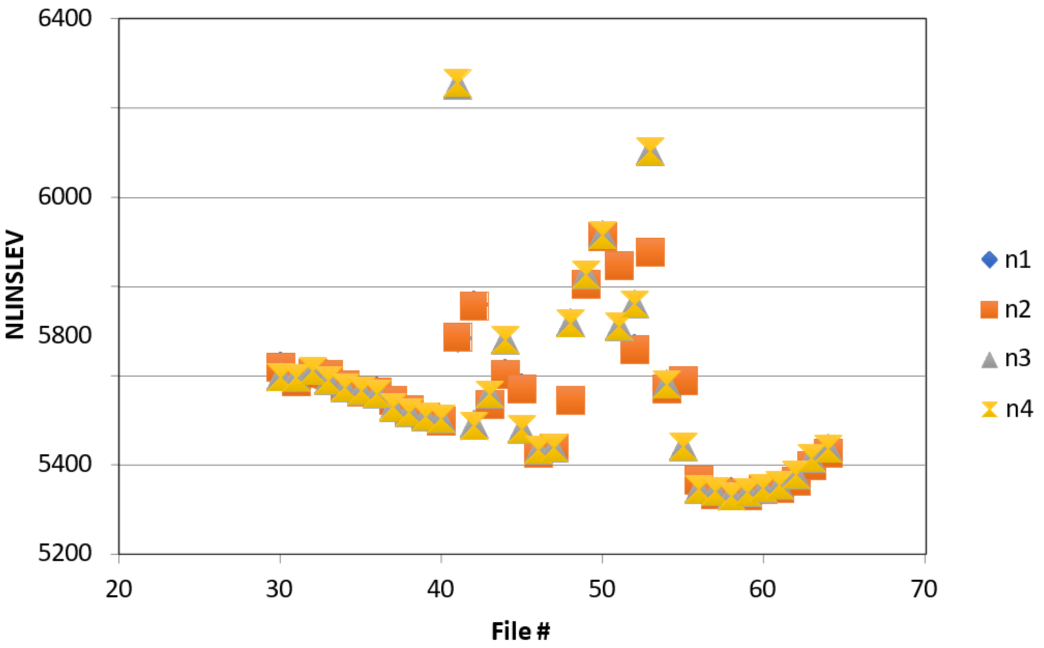

Figure 41 *The FITS header value for the NLINSLEV keyword (in ADU/pixel) vs. file number for a spectral dataset of a comet with intermittent cloud contamination. Notice all four values of NLINSLEV for file number 30 start around 5600 ADU/pixel and are within <2% of each other. The values slowly decrease over time as the airmass of the observation improves. Beginning at file 41 the difference in background values in NLINSLEV changes drastically from ~5500 ADU/pixel to as high as 6200 ADU/pixel and continues through to file 55, where it settles back again to values with a <2% variance and slowly changes due to increasing airmass.*

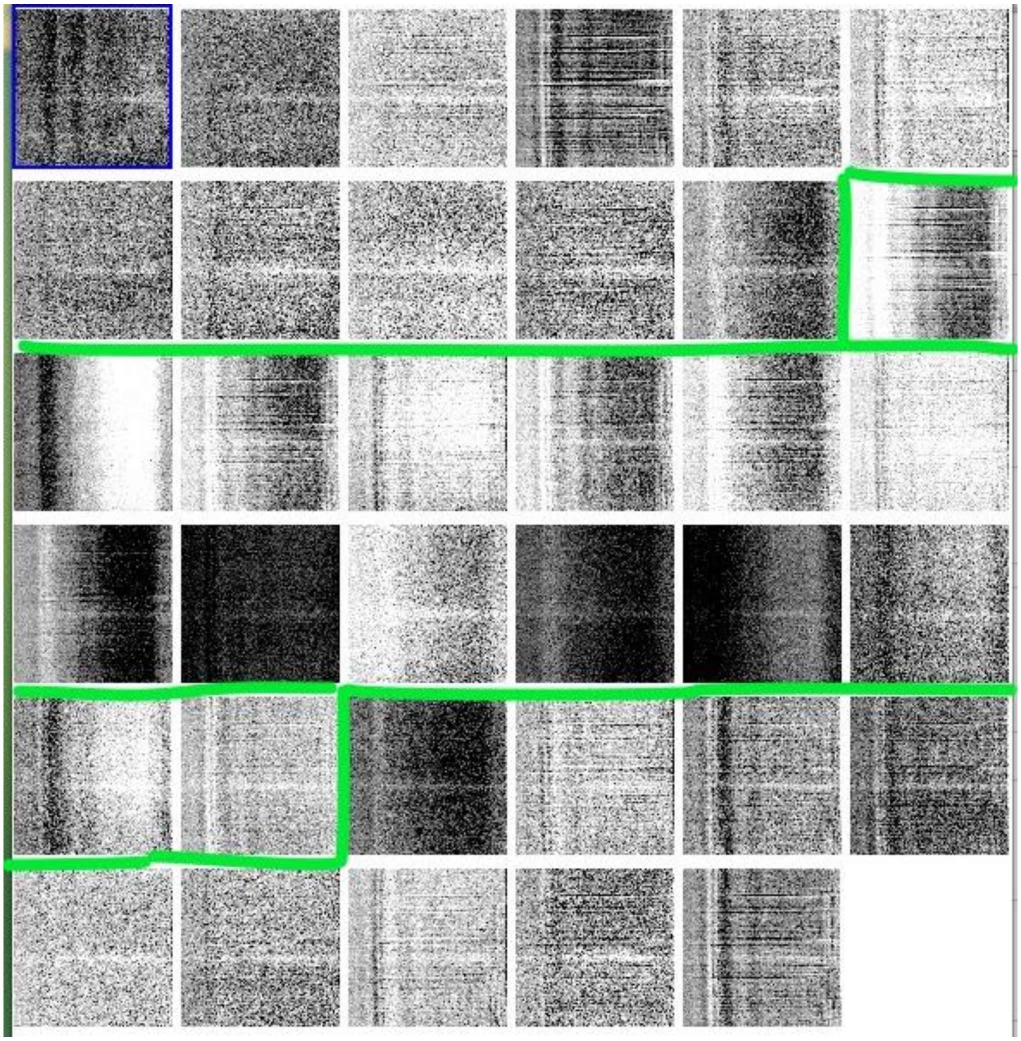

Figure 42 *The corresponding 2D spectral STK files for the comet data shown in Figure 41 above. The 2D spectra can be seen as a faint horizontal linear structure towards the middle of the array. The green outlines denote files 41 to 55, i.e., those known to be affected by clouds based on the varying NLINSLEV plot in Figure 41. Much higher background variability can be seen in these images of files 41 to 55, which is also indicative of the presence of clouds.*

4.5.1.12 High Frequency Noise

Occurrence: Common

Significance: This is intermittent electronic noise at a high spatial frequency seen as linear structures (Figure 43 and Figure 44). It can be seen in all filters and modes but is common in the 11.1 µm imaging filter, especially during short acquisitions (i.e., ACQ files) for spectroscopy observations.

Fix: There are a few possible fixes:

If it affects only a few images in a large data set that is to be coadded, those noisy images may be excluded with minimal effect to the overall S/N (Figure 44).

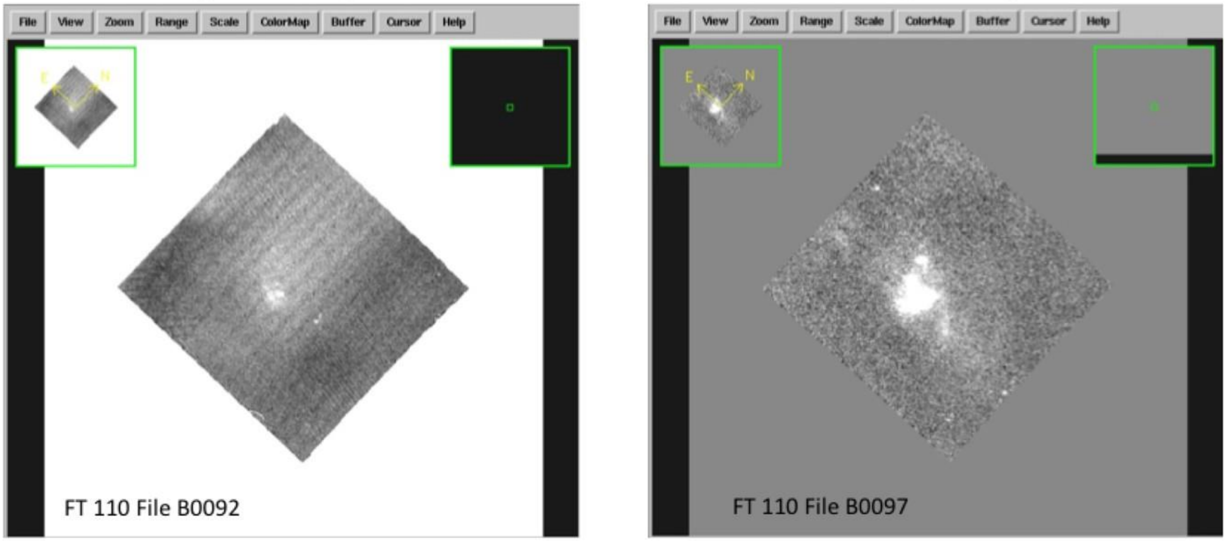

Figure 43 *An example of imaging data affected by cloud cover (Left) vs imaging data of the same source without clouds (Right). Higher background with low spatial frequency variations and linear structure residuals caused by poor subtraction of the biases of the 16 channels of the array are typically seen.*

A Fourier transform can be used to isolate the noise in frequency space and remove it (FORCAST-Periodic-Noise-Handling) from the images. For spectroscopy, however, the noise is along the rows of the array similar to the spectra, so extra caution should be used to avoid the removal of data.

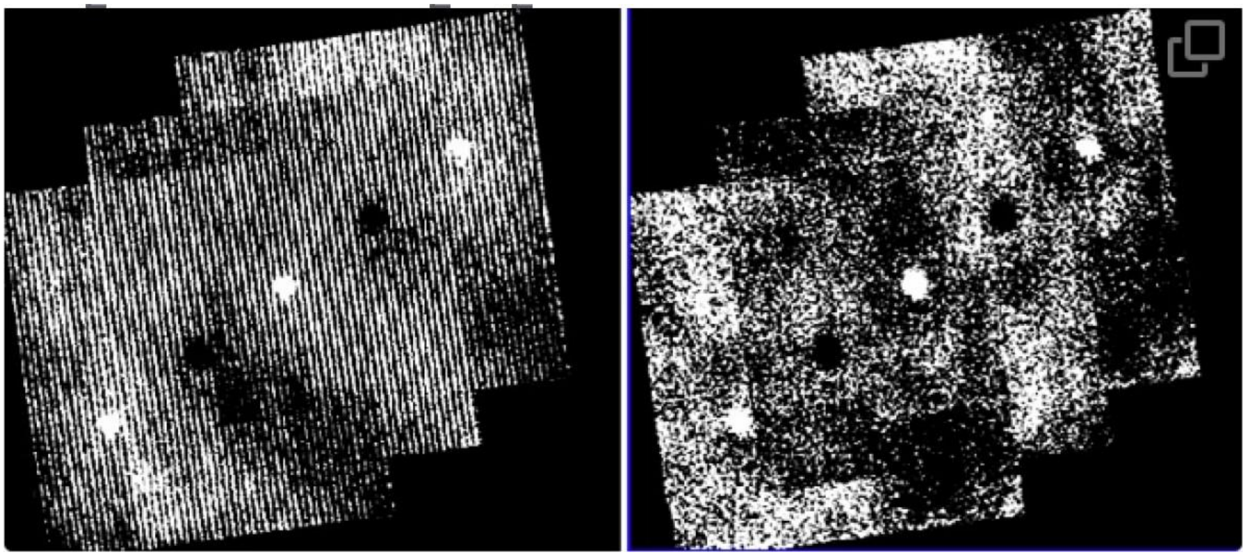

Figure 44 *Two consecutive images of a calibrator at 11.1 µm. (Left) An image containing high frequency noise. (Right) An image without the high frequency noise taken right after. The noise is horizontal across the rows of the array (i.e., in the x-direction in array coordinates), but appears almost vertical in this example because the data have been rotated so that north is up and east is left.*

4.5.1.13 The 16-pixel Shift Issue

Occurrence: Occasionally

Significance: There is an error in the FORCAST software that occasionally had a strange effect where it took the last (i.e. 16th) readout channel of the array and placed it in the first channel position, thereby shifting the array to the right in the saved FITS image (Figure 45). The FORCAST REDUX software package automatically corrects for this so it should not be seen by the user. However, this is something to be aware of if reducing FORCAST data using other software.

Fix: This is automatically fixed by using FORCAST REDUX, which searches for the position of known bad pixel clumps and detects any shift. However, this issue will have to be corrected by shifting the array manually if using other software.

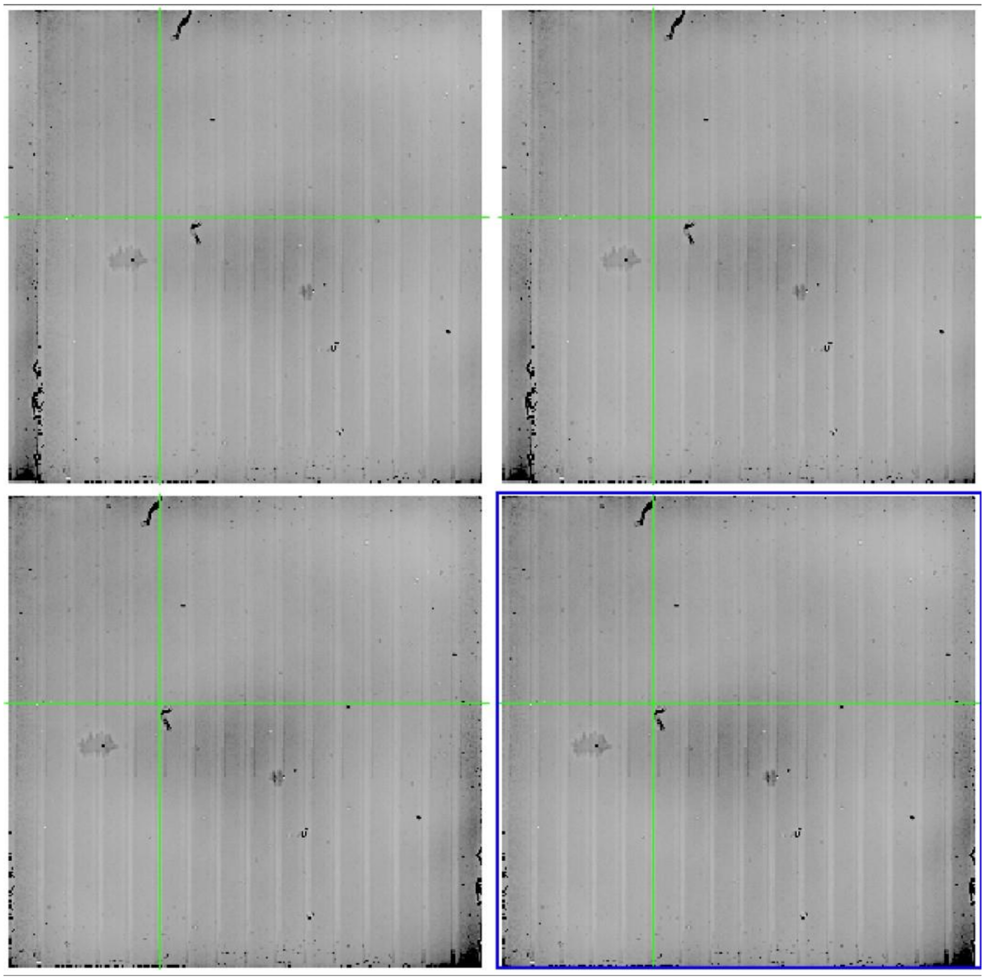

Figure 45 *Example of 16-pixel shift. Top row shows two images suffering from 16-pixel shift where the first of 16 repeating column structures should be the last column structure. Bottom row shows the same data after the SOFIA REDUX fix. In these corrected images, the bad pixel clump that looks like a backwards "7" is now near the center of the green crosshairs.*

4.5.1.14 Field Distortion

Occurrence: Often

Significance: Distortion is present and was measured throughout the optic system. This was done using a pinhole mask within the FORCAST instrument (see Figure 46) that resided in the aperture wheel along with the spectroscopic slits. This grid of pinholes was created at equal spacing, so any distortions within FORCAST could be measured and accounted for. These measured values changed little throughout the lifetime of FORCAST. However, it was found when LEVEL 4 mosaics began to be created that there were slight misalignments of overlapping regions taken at different sky angles. In addition, slight inconsistencies in astrometry were seen when comparing data taken at other telescopes. This was hypothesized to be caused by the CsI (cesium iodide) entrance window which is relatively soft and would distort (i.e., sag) over time. The window is also hygroscopic, and thus the window deteriorated non-uniformly due to humidity over time, and these effects may also contribute to the field distortion. Since the window was forward of the pinhole mask in the optical path, the pinhole mask could not be used to measure these distortions. Using FORCAST science data containing multiple infrared sources across the array, and comparing it to Spitzer data at similar wavelengths, the typical magnitude of positional uncertainty across the entire array was found to be up to 1-3 pixels (0.77-2.3″). Thus LEVEL 4 mosaics suffer from some slight distortion at the edges of overlapping regions and were aligned as best as possible to minimize any offsets.

Fix: Be cautious of astrometry when comparing multiple data sets from other telescopes/wavelengths noting the error of 1-3 pixels (0.77-2.3″) as the distance increases from the center of the array in the case of complex/multiple sources. The effect is essentially zero for compact sources near the center of the array. In theory, if there is a sufficiently dense starfield observed in the same series with accurate astrometry at other wavelengths it may be possible to calculate the distortion. There are a few sources such as RSGC1 and Westerlund 1 that have been observed that may be able to be used for this purpose. However, given that the effect is on the scale of 1-3 pixels and changes over time, it may be difficult to correct completely.

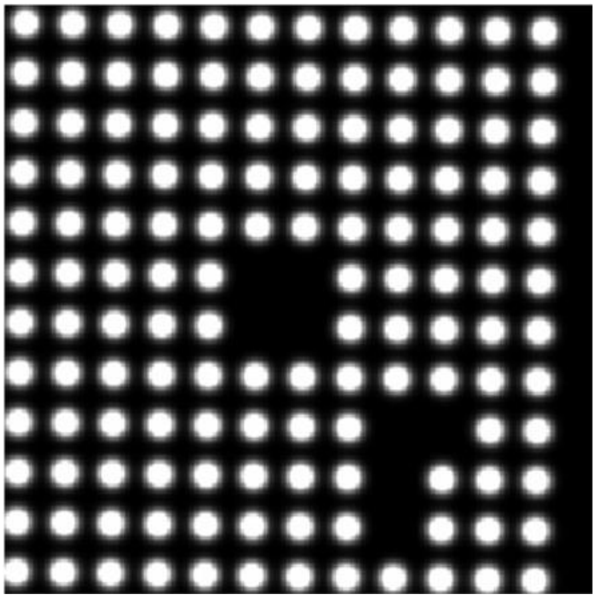

Figure 46 *Image of the pinhole mask in FORCAST.*

4.5.1.15 Window Degradation/Changes

Occurrence: OC6J, OC7D, and OC7G

Significance: As discussed in Section 4.5.1.14 above, the entrance window for FORCAST was constructed of a relatively soft material CsI (cesium iodide). Over several vacuum pump cycles this material can become distorted and can also receive damage from high humidity. Supply chain issues made it difficult to regularly replace the window as often as was desired and in the OC6J flight series (Aug 2018) the window showed significant degradation. This resulted in significant distortions at the edges of the field of view and large-scale noise structures across the images obtained (Figure 47).

The degradation of the FORCAST window in OC6J resulted in:

- High variable backgrounds which could not be adequately subtracted (Figure 48)
- Poor flux calibration, with values up to 35% off from previous series
- Positional distortion of the field at levels >5″ at the edges (Figure 49)

A new window was installed for the next flight series (OC7D, July 2019) resulting in improved backgrounds and much improved distortion. However, a change in the sensitivity in the LWC occurred, as was discussed in Section 3.4.3, and continued for the remainder of the FORCAST flight series (OC7D to OC9V).

Fix: None. The data in OC6J is heavily affected. The following data observed using a new window in OC7D-OC9V were greatly improved with the caveat of lower sensitivity in the LWC.

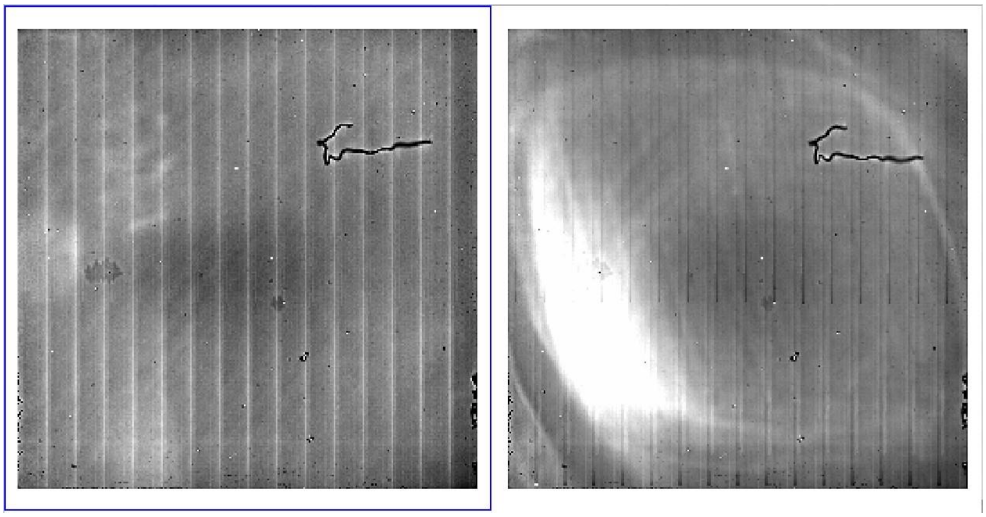

Figure 47 *(Left) A single 11 μm FITS extension from Level 1 data from the last flight in OC5K (Flight 435, Sept 2017) before the severe window degradation. (Right) A single 11 μm FITS extension from Level 1 data from the first flight of OC6J (Flight 492, Aug 2018) showing the oval-shaped noise area termed the "Cat's Eye" effect. The "Squiggle" (debris) in the upper right corner also moved and continued to shift between flights. It also had a variable effect likely due to the extra noise and could not be adequately removed even with a custom bad pixel mask, though dithering helped.*

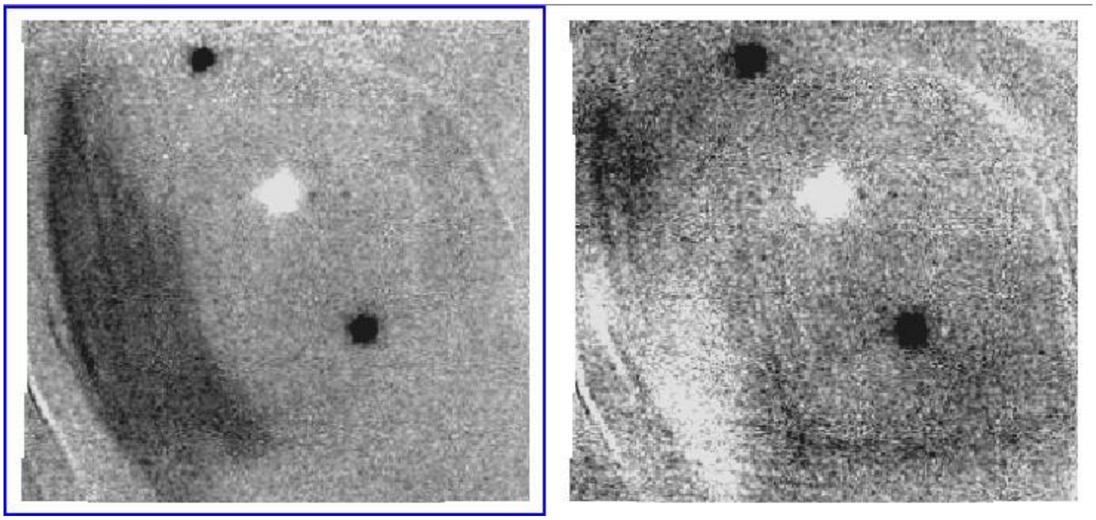

Figure 48 *Two processed and undistorted 11 μm images (Level 2 data) from OC6J taken sequentially showing the variability of the noise. The background issues were worse in shorter wavelength data and improved toward longer wavelengths with much less noticeable problems at the longest wavelength 37 μm.*

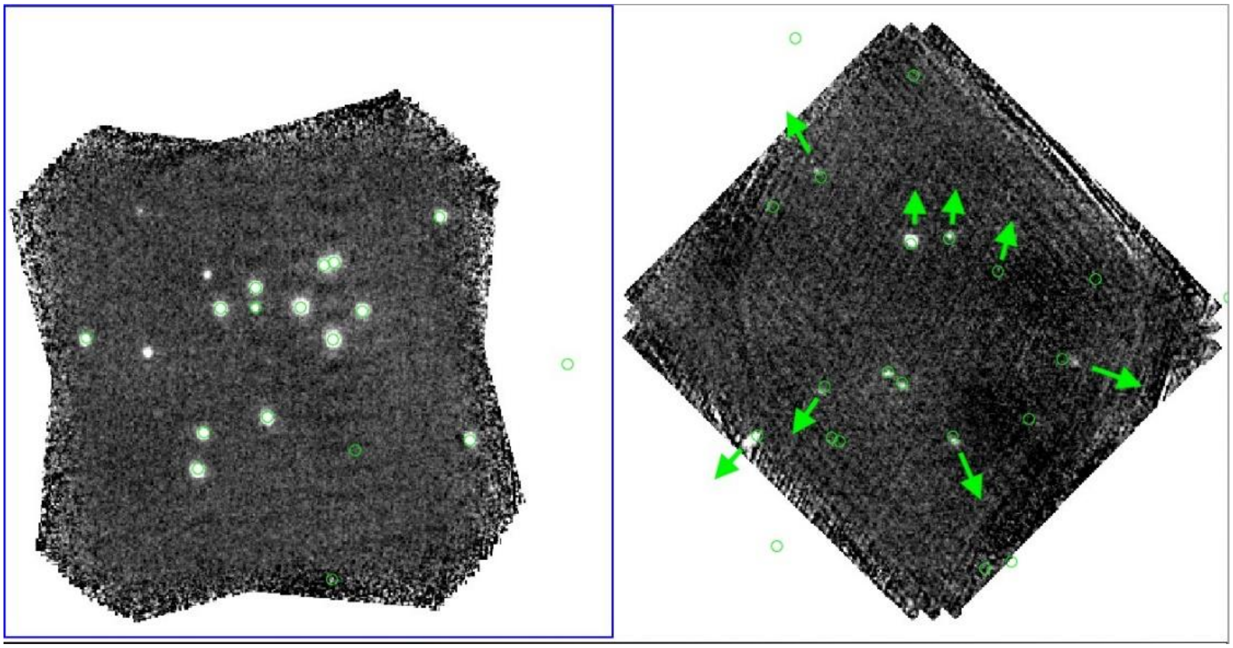

Figure 49 *(Left) Image from OC5J (Flight 425, Aug 2017) of cluster RSGC1 at 7.7 μm with green circles representing 2MASS star positions with Jmag<11. (Right) Cluster RSGC2A at 7.7 μm from OC6J (Flight 499; Aug 2018) with green circles representing 2MASS star positions with Jmag<10. Arrows roughly represent the position and direction that the stars seem to be off from the 2MASS source astrometry, showing the distortion across the field due to the window degradation.*

4.5.1.16 Boresight Misaligned

Occurrence: Often in Cycle 1 to early Cycle 4 and in-flight series OC5J; rarer in later series/cycles.

Significance: The boresight was the position on the FORCAST array matched to the center of where the telescope was pointing (i.e., the optical axis). The setup of the boresight for both imaging and spectroscopy was important for several reasons, most importantly:

- This position needed to be aligned so the astrometry was accurate and both FORCAST and telescope put the target on a known expected position on the array.
- The sky rotated on FORCAST as objects were observed overtime at different rates based on location in the sky. If the boresight was off on FORCAST the center of rotation would be off and objects would appear to slightly smear in the reduced and coadded images. This effect was larger for objects rotating relatively fast on the sky and worsened toward the array's edges. For spectroscopy, the source might partially rotate out of the slit during long observations reducing S/N or losing the target completely.

In the beginning of a flight the FORCAST boresight was aligned to the telescope's pointing using the 11.1 µm imaging filter as described in Section 3.2.1. There are additional offsets due to which filter/dichroic was being used for a particular observation (see tables in Section 3.2.1), though the SOFIA REDUX pipeline software corrected these in the Level 3 and 4 data in all but the earliest SOFIA cycles.

In general, boresights were less accurate in Cycles 1-4 than Cycles 5-9. Some series such as OC5J as well as others had known technical issues and the boresight/astrometry were corrected by hand. Quality assessment (QA) comments throughout the lifetime of FORCAST highlight specific issues with boresights due to technical issues by observation. The boresight values have an intrinsic accuracy of ~1 pixel from all filters which includes the error in measurement as well as the repeatability/accuracy of the filter/slit wheel positioning. In addition, observationally it has been noticed that the boresight position on FORCAST may change over a flight by 1-2″, possibly due to the telescope cooling at stratospheric temperature.

Fix: Typically none. Most boresight issues have already been fixed or at least documented in QA comments in the HISTORY of the data FITS files. This does not include other positional errors due to inaccurate WCS astrometry issues, as discussed above in Section 3.2. Cycles 1-4 as mentioned have the most issues and likely suffer from some slight offsets and/or smearing at the edges of array. Any fixes require careful analysis and technical knowledge of FORCAST.

4.5.1.17 Bad Pixels

Occurrence: Often

Significance: Bad pixels are elements of the detector array that are either dead (no signal) or have a much higher or lower response than average. A mask is used to select each bad pixel and replace its value with a median value derived from the values of the surrounding good pixels, or (with the more recent versions of the FORCAST Redux package) replace them with NaN values. In earlier SOFIA Cycles the REDUX software had issues calculating bad pixels at the edges of the array, causing some very bad edge effects that are now fixed in the most recent versions of REDUX. This fix greatly improved image mosaicking (a Level 4 data product). Bad pixel masks were updated for each flight series as needed and as additional pixels showed poor/no response. The

SWC array occasionally showed drastic changes from Cycle to Cycle and even sometimes from flight to flight (Figure 50). This is hypothesized to be due to the position of the SWC in the bottom of the cryostat while the LWC array was situated at the top. Consequently, in comparison, the LWC array changed very little during the entire SOFIA lifetime (Figure 51), so the bad pixel masks evolved with only minor updates.

Debris internal to the instrument (e.g., metal shavings from gear wear, paint flecks from deteriorating anti-reflection coatings) increased over FORCAST's lifetime and it was more likely that this debris would land on the SWC array. Though the arrays and internal surfaces of FORCAST were cleaned when possible, this problem could not be avoided. Thus, the bad pixel masks were updated often for the SWC.

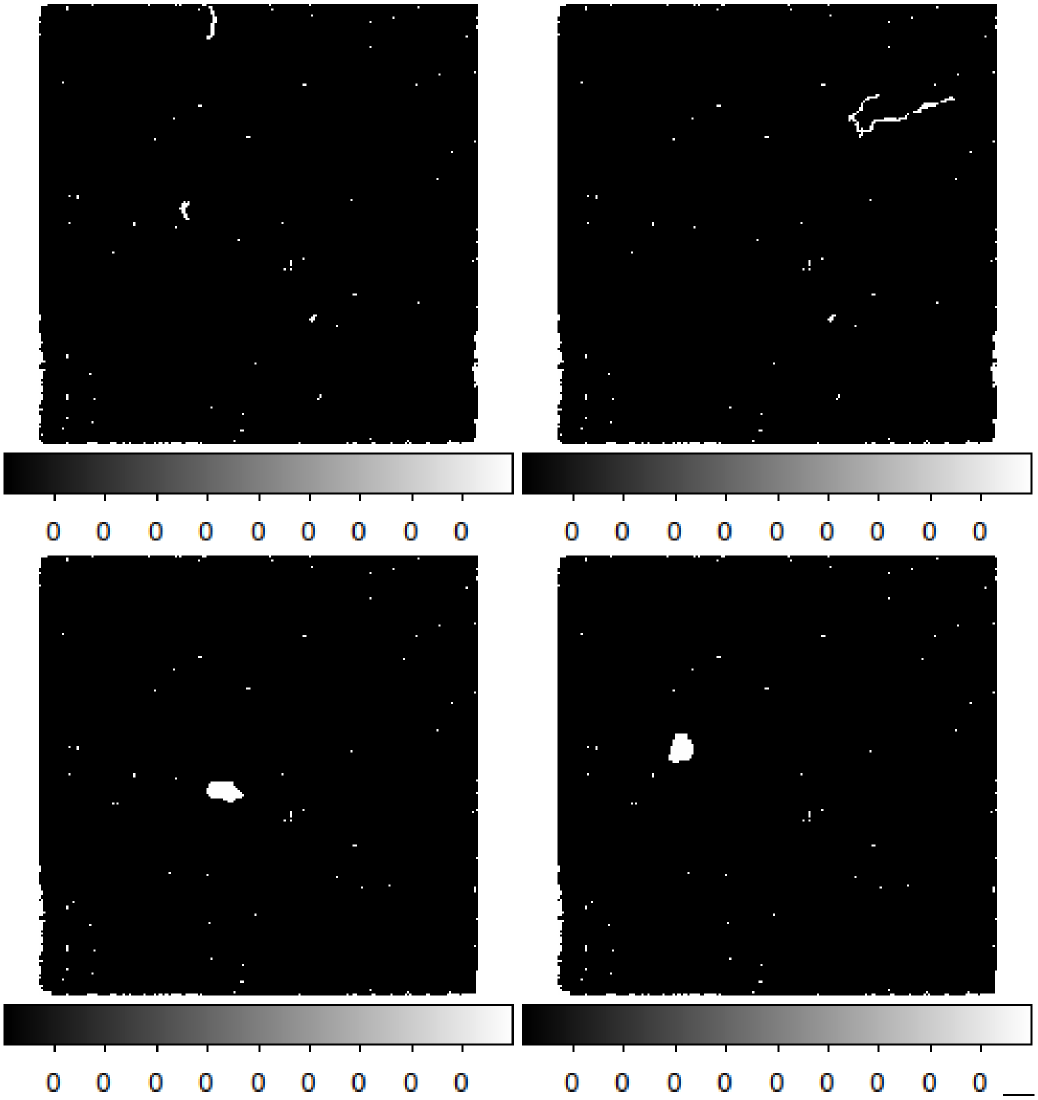

Figure 50 *Some examples of the varying bad pixel masks for the SWC from flight series OC4G (upper left), OC5J (upper right), OC8I (lower left), and OC9P (lower right). The lint-like structure can be seen to move from the upper edge of the array in OC4G to the upper right quadrant of the array in OC5J. The large paint fleck can be seen in the OC8I data, and it also moved with time, as demonstrated by the OC9P data.*

For several Cycles there was a linear hair-like structure on the array (likely lint), while the largest effect came from a large piece of debris that fell on the detector in OC8I (likely a paint chip). Though these debris stayed in one place throughout a flight series, they would often move after a cryocycle, likely due to the vacuum-pumping performed when cooling/warming the instrument between uses. The specific bad pixel maps per flight/cycle can be found in the FORCAST Pipeline software available at the SOFIA REDUX Github repository.

Fix: Use the correct bad pixel mask for the flight series.

Figure 51 *The relatively clean LWC bad pixel mask from OC9P that changed little over time.*

4.5.1.18 The 25 µm Issue

Occurrence: Often

Significance: Many standard stars observed using the FOR_F253 and FOR_F242 filters show a streak-like structure that was worse on one side of the chop pattern. The overall flux of the streak varied from a few percent to as much as ~10% of the peak of the star and affected spatial structure more than the source flux. This structure was NOT observed in asteroid calibrators indicating that it may have been associated with a short wavelength light leak in the filter, however it could be inconsistent across multiple observations which implies a possible configuration error in chop/nod timing. Corresponding standards should be looked at to evaluate the effect on the data on a case-by-case basis. Data obtained with these filters are set to USABLE.

Fix: The effect is relatively small with regards to flux calibration, so simply employing a larger photometry aperture to be sure to capture all of the source flux should be sufficient. For morphology, since it appears most predominantly in one chop beam, the off-source negative beam can be used where the effect is not obvious to confirm structure (though at a lower S/N). For instance, see the very round right-most instance of the source in Figure 52 compared to the other instances on the frame.

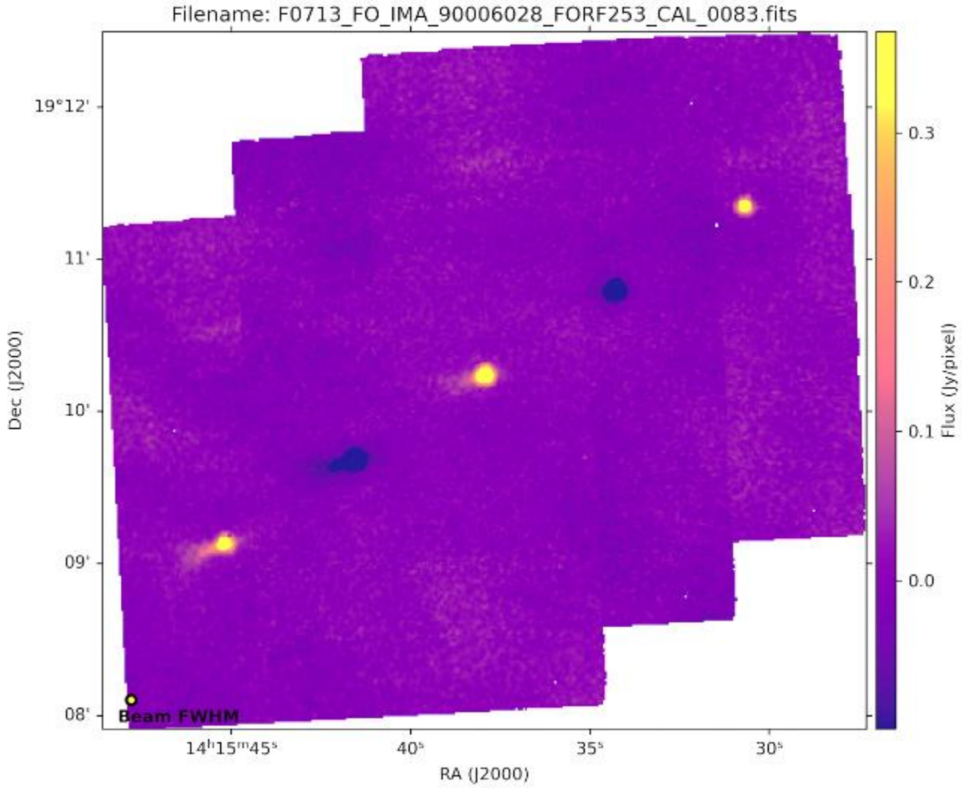

Figure 52 *An image of the calibration star Alpha Boo in the 25.3 μm filter in which the negative sources were shifted and added to the positive after multiplying by -1.0 to slightly increase S/N. In this case the rightmost chop image of the source appears fine, but the middle and leftmost chop images have a significant streak. This can also be seen in non-calibrators without any shift and add and appears to be associated with one of the chops.*

4.5.2 Spectroscopy Artifacts

4.5.2.1 Ghosting in FOR_G329

Occurrence: Always

Significance: The G329 grism suffered from significant ghosting from bright sources, which showed up as a faint spectrum just above the main source in the 2D image (Figure 53). Furthermore, analysis of both stellar and asteroid response curves (i.e., those used for SWC and LWC, respectively) indicates that, if there is an effect on the flux calibration, it is less than 5%.

Fix: A fix for this issue is implemented in the pipeline, where the extraction parameters are set in such a way that the ghosted region is excluded to minimize its effect on the final spectra.

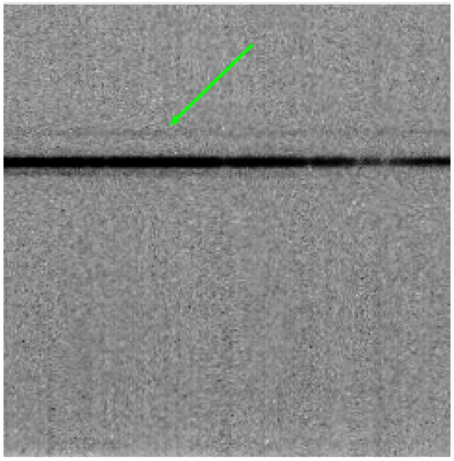

Figure 53 *A 2D spectral image with the G329 grism. The dark horizontal line is the main spectrum of the source being observed and the green arrow points to the ghost image.*

4.5.2.2 First Frame Artifact

Occurrence: Occasional

Significance: Below is an example of a noise that is also seen occasionally in imaging (see Section 4.5.1.1). A dark two-pronged structure is seen on the right side of the array. This only occurs in the first image file of a set and disappears in the second image. This may be due to a settling of the array temperature when changing frame times, though the exact cause is still be explored. The effect is small and mostly inconsequential in both imaging and spectroscopy for bright objects; however, it may cause significant issues with the faint spectra (such as shown below). Such data are usually marked as USABLE since background subtraction during extraction should mitigate this issue, but close attention should be paid to the 2D profile to decide if this file should be excluded from processing. The file should be excluded if the background in the 2D profile varies wildly along the spatial (horizontal) direction.

Fix: Exclude from processing if source is faint or the 2D profile shows strange (extremely variable along the spatial direction) background.

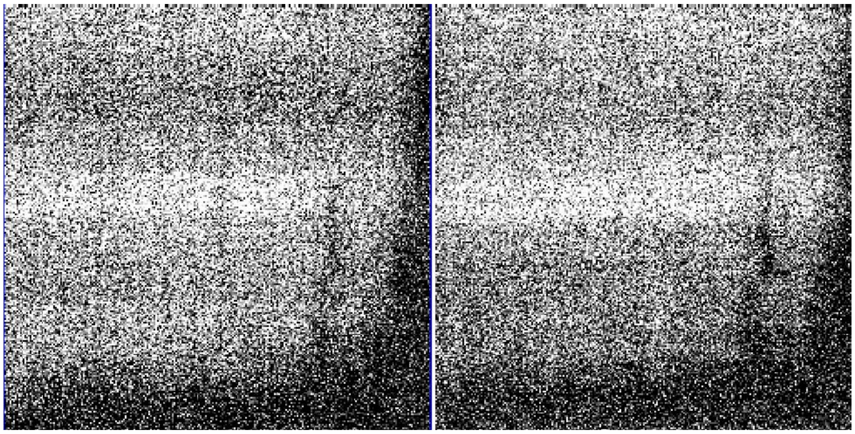

Figure 54 *Two 2D spectral images showing the First Frame Artifact. See also Figure 24.*

4.5.2.3 Dark Vertical Bands

Occurrence: Occasional

Significance: This artifact (Figure 55) usually occurs in FOR_G111 and FOR_LS47 grism/slit data. These vertical bands are caused by telluric atmospheric absorption features. The leftmost two vertical bands (as seen in Figure 55) are not an issue as they are caused by the highly variable telluric ozone absorption feature, and that part of the spectrum can never be recovered and used for data analysis. However, the two bands near the middle and on the right (in Figure 55) can be an issue on occasion. Looking at the reduced spectrum in Figure 56, these artifacts can appear as dips in the flux, though the dips are very small, almost within the error bars.

Fix: Exclude from processing if the dips in the spectra are larger than the error bars.

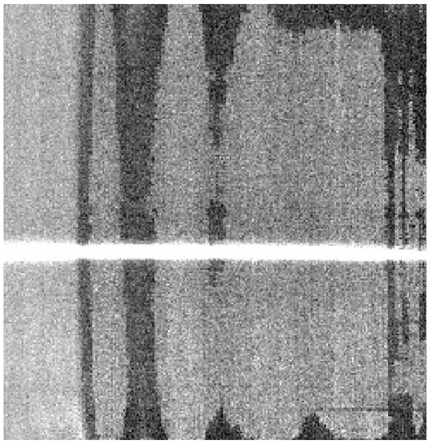

Figure 55 *(Left) A 2D spectral image using G111 and the 4.7" slit showing the Dark Vertical Bands effect.*

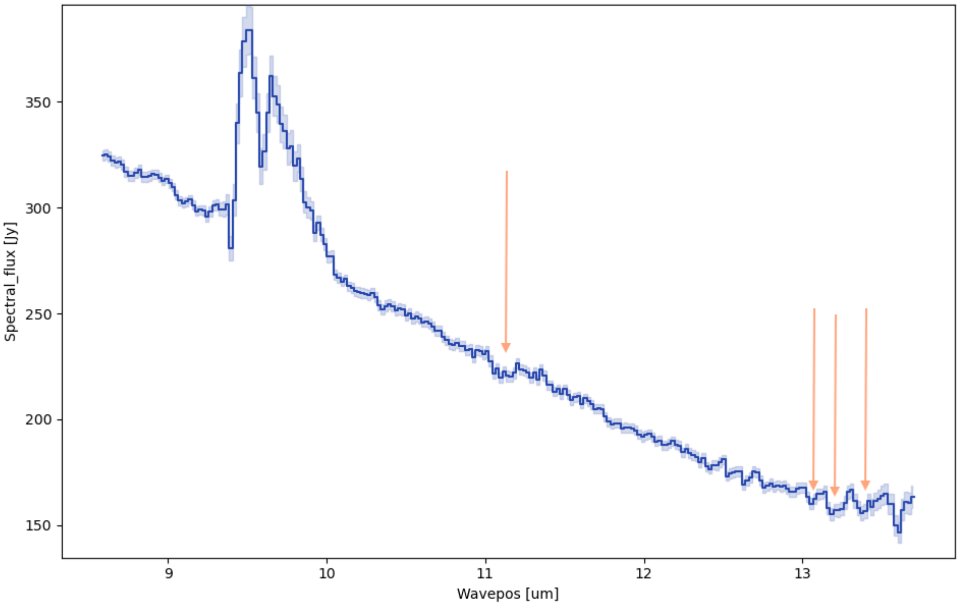

Figure 56 *A reduced spectrum with error bars from the data shown in Figure 55. The red arrows show the Dark Vertical Bands locations and how they may affect the spectrum. The large feature from 9.4-10 μm is the telluric ozone feature (and is usually discarded from the spectral data), which coincides with one of the strong vertical bands.*

4.5.2.4 Source Off Slit

Occurrence: Occasional

Significance: During an observation, for various reasons, the source may move off the slit. Most of the time these observations get flagged by the pipeline and are excluded from processing, but occasionally when there are structures in the background regions the SOFIA REDUX pipeline may extract it as shown in the image below. Figure 57 shows nine consecutive observations of a fairly bright source but during the observation the source was off the slit for one of these observations and is not visible in the 2D image (see middle panel). However, the SOFIA REDUX pipeline extracted a spectrum (as shown by the green aperture line) of some random background region. This can also be seen in the extracted spectra where the flux values for just this one observation are close to zero (Figure 58). This issue can also be diagnosed by looking at the runtime log for the "Locate Aperture" module where the location of the aperture is 22.96″ (see log output in Figure 59) instead of the value of all the other apertures around 85″.

Fix: Exclude the bad (source off slit) file from the input manifest and re-run the reduction.

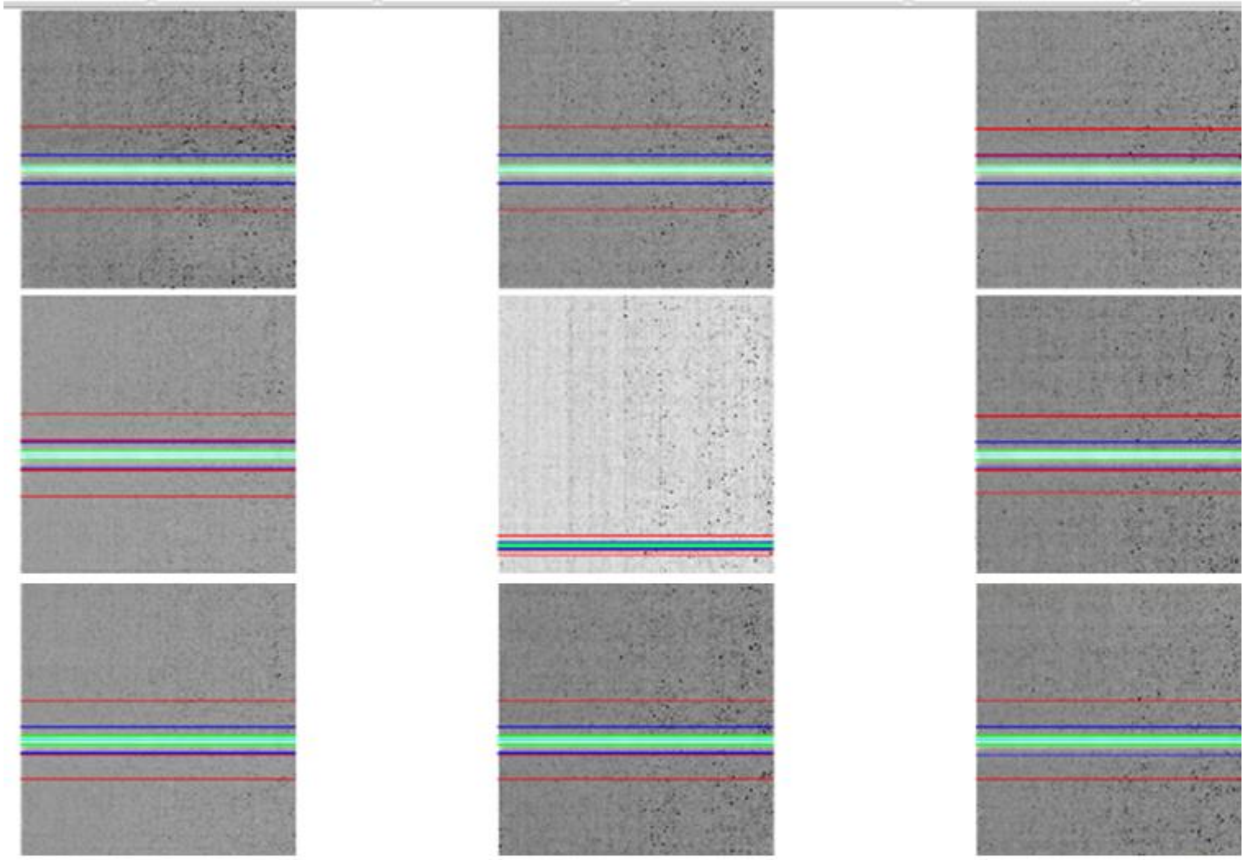

Figure 57 *Nine 2D spectral images to be coadded to create a final spectrum. The central 2D image has no spectrum because the source was off the slit. However, the SOFIA REDUX software chose a random background location and extracted a spectrum there (highlighted in green).*

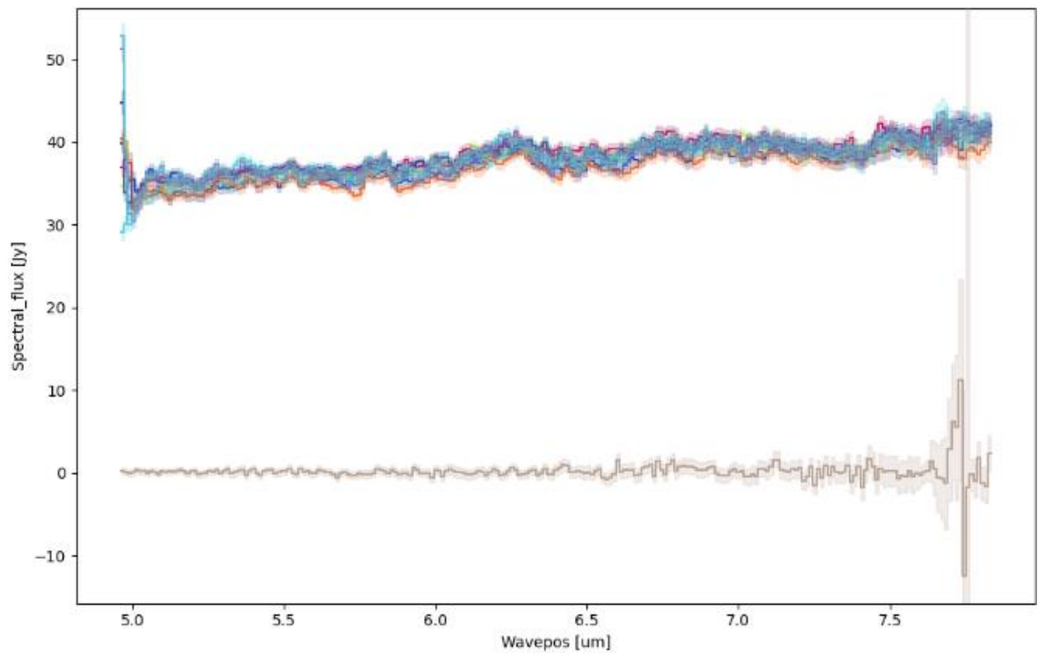

Figure 58 *The extracted spectra from each of the panels of Figure 57, each with a different color and overlaid on top of each other. The spectrum created from the middle panel of Figure 57 can be seen as the outlier at the bottom with a flux near zero.*

```
2023-07-12 13:34:14,550 - sofia_redux.pipeline.sofia.forcast_spectroscopy_reduction - INFO -
F0333_FO_GRI_040129177_FORG063_LOC_0250.fits

2023-07-12 13:34:14,550 - sofia_redux.pipeline.sofia.forcast_spectroscopy_reduction - INFO -    85.059 arcsec (sign: 1, fit FWHM: 4.325)

2023-07-12 13:34:14,550 - sofia_redux.pipeline.sofia.forcast_spectroscopy_reduction - INFO -

2023-07-12 13:34:14,552 - sofia_redux.pipeline.sofia.forcast_spectroscopy_reduction - INFO -
F0333_FO_GRI_040129177_FORG063_LOC_0251.fits

2023-07-12 13:34:14,552 - sofia_redux.pipeline.sofia.forcast_spectroscopy_reduction - INFO -    85.053 arcsec (sign: 1, fit FWHM: 4.358)

2023-07-12 13:34:14,553 - sofia_redux.pipeline.sofia.forcast_spectroscopy_reduction - INFO -

2023-07-12 13:34:14,556 - sofia_redux.pipeline.sofia.forcast_spectroscopy_reduction - INFO -
F0333_FO_GRI_040129177_FORG063_LOC_0264.fits

2023-07-12 13:34:14,556 - sofia_redux.pipeline.sofia.forcast_spectroscopy_reduction - INFO -    22.964 arcsec (sign: 1, fit FWHM: 1.809)

2023-07-12 13:34:14,556 - sofia_redux.pipeline.sofia.forcast_spectroscopy_reduction - INFO -

2023-07-12 13:34:14,558 - sofia_redux.pipeline.sofia.forcast_spectroscopy_reduction - INFO -
F0333_FO_GRI_040129177_FORG063_LOC_0267.fits

2023-07-12 13:34:14,559 - sofia_redux.pipeline.sofia.forcast_spectroscopy_reduction - INFO -    84.928 arcsec (sign: 1, fit FWHM: 4.191)

2023-07-12 13:34:14,559 - sofia_redux.pipeline.sofia.forcast_spectroscopy_reduction - INFO -

2023-07-12 13:34:14,561 - sofia_redux.pipeline.sofia.forcast_spectroscopy_reduction - INFO -
F0333_FO_GRI_040129177_FORG063_LOC_0268.fits

2023-07-12 13:34:14,561 - sofia_redux.pipeline.sofia.forcast_spectroscopy_reduction - INFO -    84.895 arcsec (sign: 1, fit FWHM: 4.176)

2023-07-12 13:34:14,561 - sofia_redux.pipeline.sofia.forcast_spectroscopy_reduction - INFO -
```

Figure 59 *A snippet from the SOFIA REDUX runtime log for the "Locate Aperture" module when run on the data in Figure 57. The aperture of the observation with no source in the slit was found to be 22.964" (red) instead of a value similar to all the other data around 85".*

4.5.2.5 Edge Effect/Artifact

Occurrence: Often

Significance: These artifacts are observed in the FOR_G063 and FOR_G111 grisms. The first artifact can be seen in the 2D images of FOR_G063, where it manifests as a small (~5 pixel) bright dot close to the PSF of the source (Figure 60, left). This results in enhancement of flux in the first 5 pixels (i.e for wavelengths < 5.0 µm) of the spectra (Figure 60, right). The second edge effect is seen in the FOR_G111 grism data, but instead of enhancement of flux, there is a drop in the flux (Figure 61) for the *last* 5 pixels (i.e., wavelengths > 13.5 µm).

Fix: None. Users should determine if their data is affected by this artifact and if the edges of the spectra should be excluded from analysis.

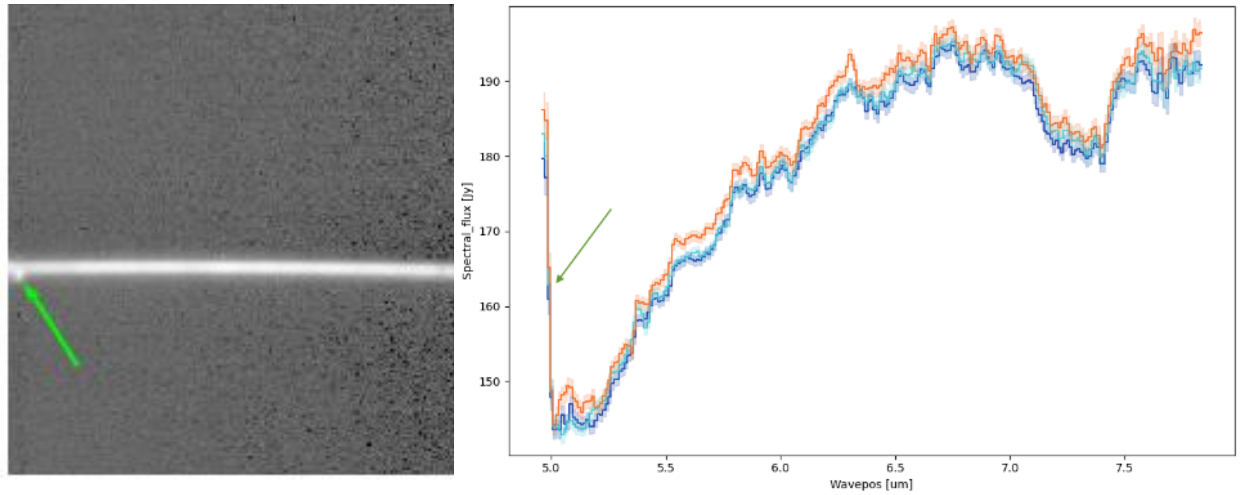

Figure 60 *(Left) Small bright dot artifact that can be seen often at the leftmost part of a 2D spectrum using the G063 grism (delineated by the green arrow). (Right) A spectral extraction of the data on the left showing how this affects the resultant spectra.*

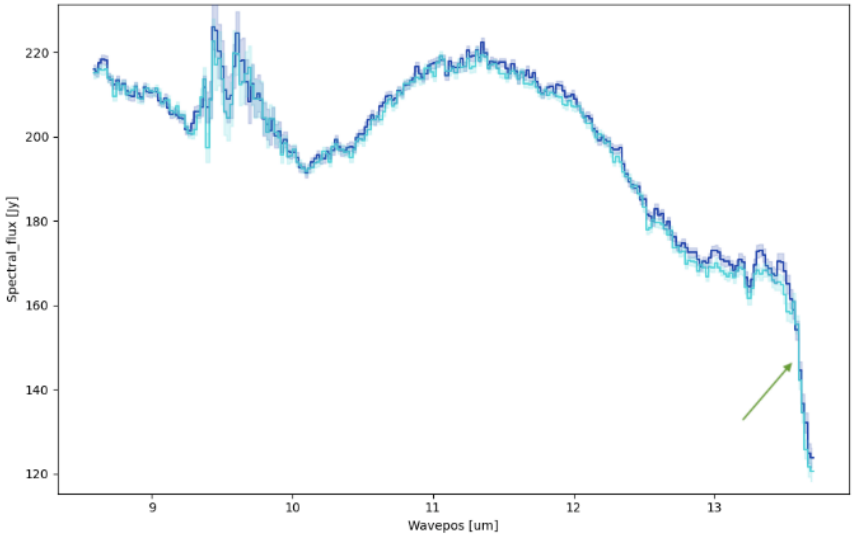

Figure 61 A 2D spectrum using the G111 grism showing the long wavelength drop in flux (delineated by the green arrow).

5. SCIENTIFIC RESULTS

FORCAST was originally designed to be a mid-infrared camera with imaging capabilities from 5 to 40 μm. The imaging mode of this instrument provided a great value to the SOFIA community for studies of protostellar environments, young star clusters, molecular clouds, planetary bodies, and galaxies. The large filter suite in FORCAST provided access to multicolor information that allowed the determination of dust temperatures, dust optical depths, dust mass, and dust composition of these astronomical sources. Its relatively large field of view (~3′x3′) and ability to chop and nod up to 10′ allowed for imaging of extended emission regions with no reference beam contamination, something not possible from ground-based telescopes. Although FORCAST was not as sensitive as its space-based counterparts like Spitzer and WISE, it had essentially no saturation issues and therefore allowed observations of the brightest infrared objects of the Galaxy and the study of Solar System bodies (even the Moon itself).

The inclusion of grisms in FORCAST shortly before commissioning allowed for R~200 spectral studies of a wide range of objects. Both molecules and grains have distinctive mid-infrared (5–40 μm) spectral signatures that can be used to identify them, determine their abundance, study their environments, and understand under what conditions they are created and destroyed. For instance, hydrocarbons with prominent spectral signatures from 3–16 μm, such as polycyclic aromatic hydrocarbons (PAHs), are frequently observed near regions of star formation (in emission and occasionally in absorption) and characteristics of ionized PAHs in the 6–9 μm region can be used to diagnose radiation environments. In the 5–40 μm wavelength range, interstellar mineral grains also display a variety of spectral features. Silicates seen in the interstellar medium, circumstellar environments, and on solar system body surfaces have prominent features seen from 8 to 13 μm, as well as from 17-20 μm, which can be used to understand the mineral composition of astronomical sources. Strong mid-IR excitation lines like 4.05 μm HI Br α, 4.49 μm [Mg IV], 4.53 μm [Ar VI], 5.61 μm [Mg V], 6.99 μm [Ar II], 7.65 μm [Ne VI], and 8.99 μm [Ar III], for instance, are more reliable abundance indicators in planetary nebulae (PNe) than ultraviolet and optical diagnostic lines because they are less sensitive to extinction and temperature variations. Additionally, heavier elements, such as Al, Si, Ne, and S from 3-38 μm and Ni and Co at 6-16 μm, are visible in novae and supernovae (SNe) by means of mid-IR spectroscopic excitation lines; it is possible to track the generation of iron-group elements in SNe using the Ni and the 20–30 μm Fe lines.

Detailed below are several FORCAST science results highlighting its unique imaging capabilities and spectroscopic diagnostic abilities. The first result (Section 5.1) demonstrates FORCAST's unique ability to map large areas and observe extremely bright objects without saturation in our Galactic Center. The second result (Section 5.2) demonstrates FORCAST's ability to perform spectroscopy on the brightest infrared object in the night sky – the Moon – to observe water in a wavelength range not observable from the ground and not available or impossible to do from previous infrared satellite missions. Perhaps the most requested observing scenario for FORCAST's imaging mode was multi-wavelength mid-infrared science, and the third result (Section 5.3) demonstrates the application of that technique on a large dataset of high-mass protostars. And the final science result (Section 5.4) shows an example of the power of using FORCAST's entire complement of grisms (i.e., all four grisms covering a range from 5 to 40 μm) to better understand the nature and evolution of astronomical objects, in this case the monitoring of the temporal fluctuations in the mass transfer between two stars in the symbiotic binary R Aquarii.

5.1 GALACTIC CENTER LEGACY IMAGING SURVEY

- Principle Investigator: *M. Hankins (California Institute of Technology)*
- Plan ID: 07_0189, 09_0217

Publications:

- SOFIA/FORCAST Galactic Center Legacy Survey: Overview, M. Hankins et al. (2020), ApJ, 894, 55
  DOI: 10.3847/1538-4357/ab7c5d

The original science driver for this Legacy program was to understand why the dense inner region of our Galaxy has a global star formation rate that is more than an order of magnitude lower than expected. Indeed, the inner 200 pc of the Milky Way does have some of the most extreme conditions for star formation in our Galaxy, including high molecular gas concentrations, high gas and dust temperatures, substantial turbulence, and a powerful gravitational potential well. However, comparable environments are thought to exist in other galaxies similar to our Milky Way, and these galaxies seem to have much higher rates of star formation near their centers. Especially given the molecular gas reservoir of the Milky Way's Central Molecular Zone (CMZ), theoretical models predict much higher star formation rates than what is observed. To study this issue further, the Galactic Center Legacy Survey was designed to image the CMZ at mid-infrared wavelengths which can penetrate through the high levels of extinction of our Galaxy's central region and directly observe the star formation presently occurring there.

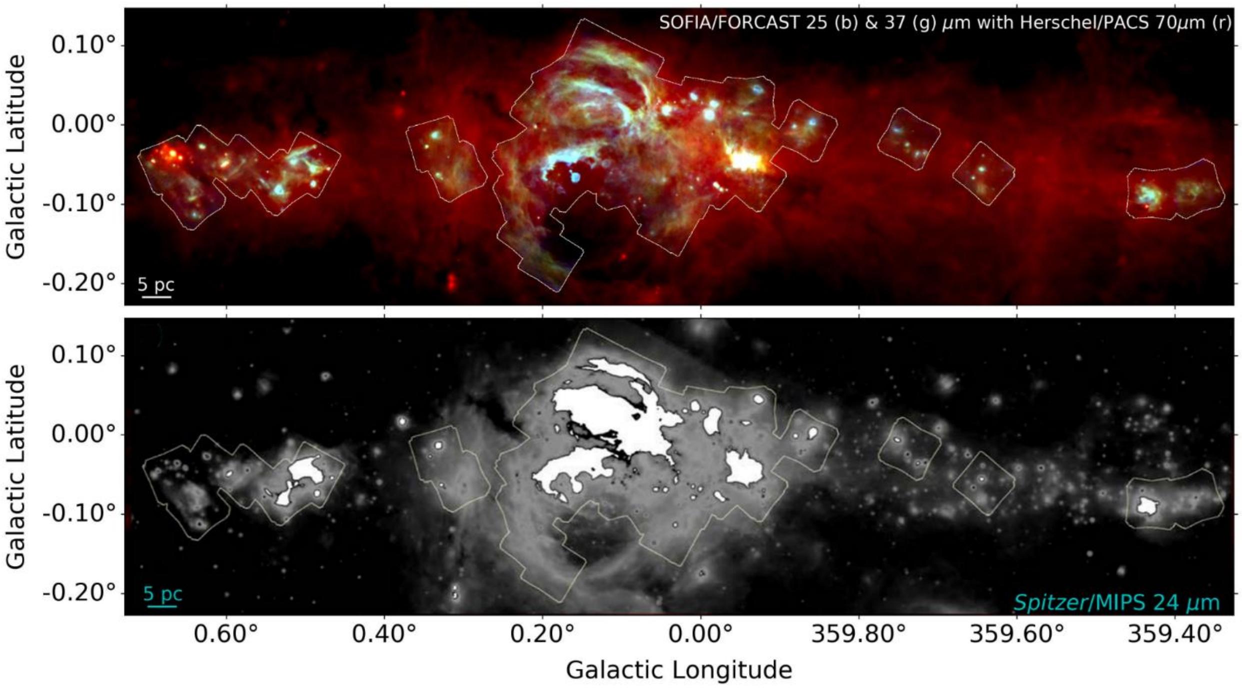

Figure 62 *(Top) A three-color RGB image of the central ~200 pc of the Milky Way with FORCAST 25 μm shown as blue, FORCAST 37 μm as green, and Herschel 70 μm as red. The areas mapped by FORCAST are delineated by the light white lines. (Bottom) An image of the same region from Spitzer at 24 μm showing that much of the region is saturated (bright white areas) and unusable for science.*

The FORCAST observations cover many important regions within the CMZ like Sagittarius A, B, and C which were badly saturated in the Spitzer/MIPS 24 µm observations (Figure 62). Because of this, previous studies of these regions relied on earlier observations from the Midcourse Space Experiment (MSX), which had very coarse spatial resolution of about 18″ at 21 µm. The FORCAST images for the Legacy project were obtained at 25 and 37 µm and at a resolution of about 2.3″ and 3.2″, respectively, allowing for the first-time detailed study of small-scale structure and individual star forming cores throughout the CMZ at these wavelengths. An overview of the survey and some preliminary results are given in Hankins et al. (2020). Further papers related to the main goals of the project are in progress as of the writing of this handbook.

A total of 42 FORCAST fields were observed, each ~3′x3′, and stitched together to form large-scale maps covering 403 arcmin^2 (2180 pc^2) at a physical resolution of ~0.07 pc at 25 µm and ~0.1 pc at 37 µm (see Figure 62). These data had nominal point source sensitivities of ~250 mJy at 25 µm and ~400 mJy at 37 µm. The maps cover many areas of interest, including the circumnuclear ring around our Galaxy's supermassive blackhole, Sgr A*, the Arches cluster region, the Sickle HII region, the Quintuplet cluster, and the Pistol star, as well as the Sgr A, B, and C star-forming complexes.

The complete science-ready maps are available from the IRSA archive.

5.2 MAPPING THE 6 MICRON MOLECULAR WATER LINE ACROSS THE LUNAR SURFACE

- Principle Investigator: *P. Lucey (University of Hawaii)*
- Plan IDs: 07_0061, 08_132, 09_0171

Publications:

- Molecular water detected on the sunlit Moon by SOFIA, C. Honniball et al. (2020), Nature Astronomy, 5, 121
  DOI: 10.1038/s41550-020-01222-x
- Regional Map of Molecular Water at High Southern Latitudes on the Moon Using 6 µm Data From SOFIA, C. Honniball et al. (2022), GRL, 49, e97786
  DOI: 10.1029/2022GL097786
- SOFIA+FORCAST Lunar Legacy Project Processing Procedure, A. Arredondo et al. (2023), PASP, 135, 024501
  DOI: 10.1088/1538-3873/acb1d6
- The Distribution of Molecular Water in the Lunar South Polar Region Based upon 6 µm Spectroscopic Imaging, W. Reach et al. (2023), PSJ, 4, 45
  DOI: 10.3847/PSJ/acbdf2

Signs of water had been detected on the Moon previously as ice in the permanently shadowed craters near the lunar poles, though most previous observations used the near-infrared spectral signature of water at 3 µm where the signals for H_2O and OH (hydroxyl) are blended. In this way, previous observations, including spacecraft observations, could not unambiguously separate water from hydroxyl, and it was often unclear how much or if any of the signal was due to water. Therefore, despite many observations, there existed no direct detection of water on the lunar surface, and the amount and locations of lunar water were still unclear. However, the fundamental bending vibration of the H-O-H molecular bond of water occurs at 6.1 µm in the infrared and does not suffer from blending from other OH-related compounds, providing a clear and unambiguous spectral signature. Furthermore, unlike space-based infrared telescopes like Spitzer and WISE, FORCAST could safely be pointed at the Moon to directly observe spectroscopically in this wavelength range. Moreover, such observations are not possible from ground-based telescopes because this region of the spectrum is completely obscured from the ground by water in the Earth's atmosphere.

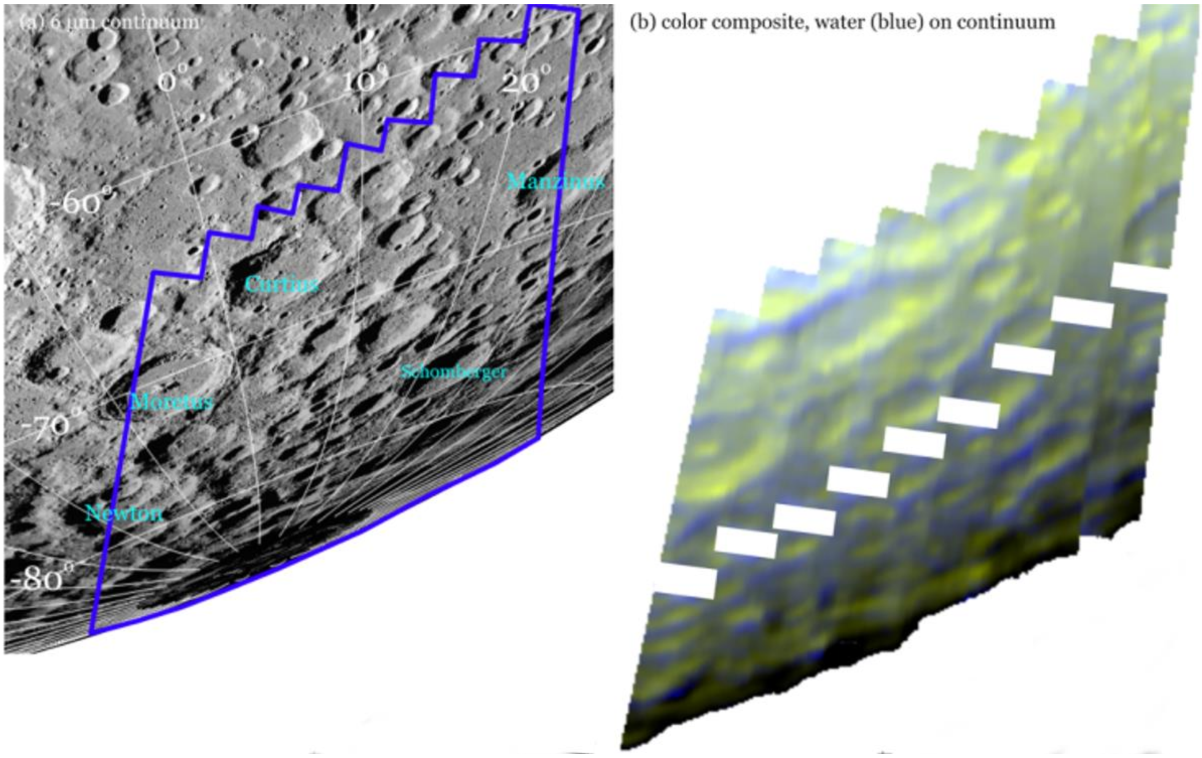

Figure 63 *(Left) Lunar Reconnaissance Orbiter Wide Angle Camera optical image of the southern limb of the Moon, oriented with the celestial pole at the top as appropriate for 2022 February 17, with lunar coordinate grid overlaid and an outline of the region observed with SOFIA (blue lines). (Right) Color rendition of FORCAST water and continuum emission. The color image combines the 6 μm continuum surface brightness (green) and the 6 μm water feature strength (blue). The diagonal empty regions on the water image mask a partially transparent defect on the surface of the detector that leads to significantly higher noise.*

Using FORCAST, Honniball et al. (2020) made the first-ever direct detection of the water molecule (H_2O) on the sunlit surface of the Moon. This discovery refines our understanding of the behavior of water and how volatile elements and compounds interact with airless bodies throughout the Solar System and beyond. After the success of this proof-of-concept observation, the team was awarded a SOFIA Legacy project to map out this water feature across large areas of the lunar surface. By stepping the spectral slit of FORCAST across large areas of the Moon, the team was able to construct spectral and spatial maps centered on the 6.1 μm water line. From this data Reach et al. (2023) published a map of a 90,000 square mile area near the South Pole with a resolution of about 3 miles (Figure 63). In this first-ever detailed map of water on the surface of the Moon, comparisons with the lunar landscape show that the water emission is strongest on the shady sides of deep craters and high mountains (Figure 63).

Observing the Moon posed some unique challenges, and the resultant data were non-standard, requiring special reduction techniques which are described in Arredondo et al. (2023). For more information about the Lunar Legacy program and data, see the Lunar Legacy Program web page at IRSA.

5.3 THE SOFIA MASSIVE (SOMA) STAR FORMATION SURVEY

- Principle Investigator: *J. Tan (Chalmers University/ University of Virginia)*
- Plan IDs: 01_0045, 02_0074, 03_0109, 04_0077, 06_0042, 06_0058, 09_0085

Publications:

- The SOFIA Massive (SOMA) Star Formation Survey: I. Overview and First Results, J. De Buizer et al. (2017), ApJ, 843, 33
  DOI: 10.3847/1538-4357/aa74c8
- The SOFIA Massive (SOMA) Star Formation Survey: II. High Luminosity Protostars, M. Liu et al. (2019), ApJ, 874, 16
  DOI: 10.3847/1538-4357/ab07b7
- The SOFIA Massive (SOMA) Star Formation Survey: III. From Intermediate- to High-mass Protostars, M. Liu et al. (2020), ApJ, 904, 75
  DOI: 10.3847/1538-4357/abbefb
- The SOFIA Massive (SOMA) Star Formation Survey: IV. Isolated Protostars, R. Fedriani et al. (2023), ApJ, 942, 7
  DOI: 10.3847/1538-4357/aca4cf

Compared to our present knowledge of how stars like our Sun form, much less is known about how star formation proceeds for stars with very large masses. One hypothesis is that massive star formation occurs in a manner very similar to how we think our own Sun formed: at the center of a molecular core there was a swirling disk of gas that fed a growing protostar. This was accompanied by the launching of powerful, magnetized winds that flow out from above and below that disk, which blow cavities through the dense, dusty core within which the star formed. Theoretical models of high-mass star formation based upon this “core accretion” scenario have been developed, predicting the integrated flux and flux distribution (i.e., observed source geometry) as a function of infrared wavelength.

To test these theoretical models and learn more about mass star formation in general, the **SO**FIA **MA**ssive (SOMA) Star Formation Survey aimed to characterize a large sample (~50) of high- and intermediate-mass protostars over a range of evolutionary stages and environments. By measuring the ∼7–37 μm fluxes of these protostars using FORCAST, the Legacy team has been testing whether or not the flux behavior as a function of wavelength can be fit by their models. In Paper I of the survey (De Buizer et al. 2017), the first eight sources were presented, which were mostly massive protostars. In Paper II (Liu et al. 2019), seven additional high-luminous sources were presented, corresponding to some of the most massive protostars in the survey. In Paper III (Liu et al. 2020), 14 intermediate-mass sources were presented and analyzed, and the results were compared and contrasted to the high-mass sample. In Paper IV of the series (Fedriani et al. 2023), 11 sources were selected for study based on the fact that they appeared to be relatively isolated in the 37 μm images. As of the writing of this handbook, another set of eight regions that are relatively crowded in their 37 µm images (i.e., clustered sources), will be presented in Paper V in this series (Z. Telkamp et al. 2022, in preparation). These will be studied and compared to the isolated sources from Paper IV.

The imaging data for all of the massive protostars in the survey were performed with four FORCAST filters: 7.7, 19.7, 31.5, and 37.1 µm. The last two of these filters proved to be very valuable since they sample near the peak of the spectral energy distribution (SED) of the protostellar sources and help to accurately estimate the measured source luminosity (Figure 64). Combined with data at other infrared wavelengths, including data from Spitzer-IRAC and from Herschel, SEDs across the entire infrared were generated for all protostars. It was determined that these SEDs could indeed be well-fit with the Core Accretion models, and thus estimates of many physical properties could be ascertained (e.g., core mass, extinction, disk accretion rate, etc.). Future papers will take into account source geometry as a function of wavelength to further test the validity and accuracy of the models.

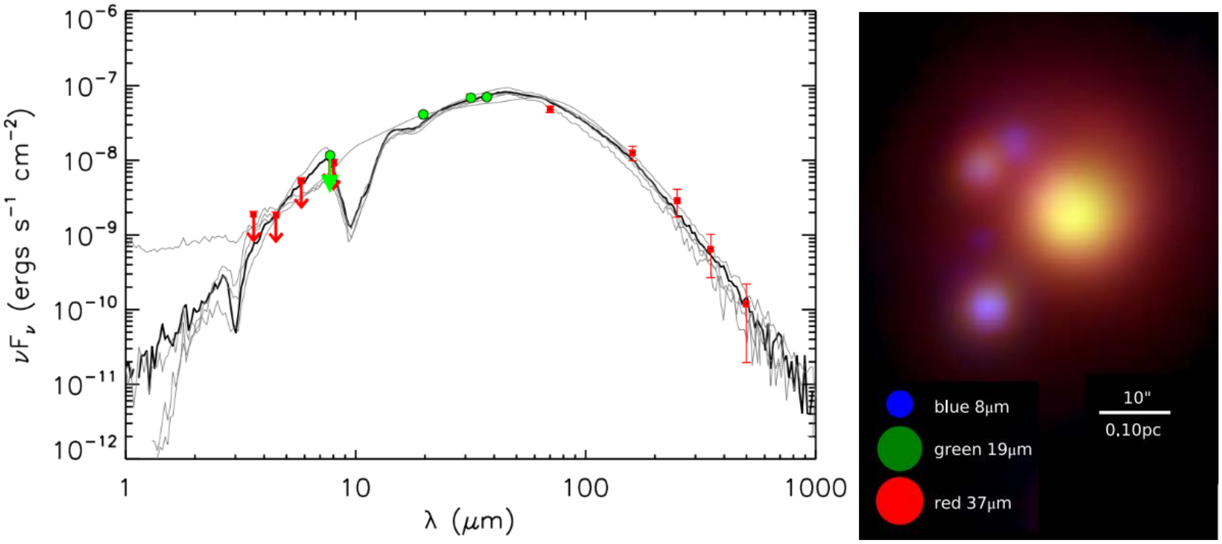

Figure 64 *(Left) An SED for protostar AFGL 437 (from De Buizer et al. 2017). The green data points are flux measurements from SOFIA-FORCAST at 7.7, 19.7, 31.5, and 37.1 µm, and the red data points are from Spitzer-IRAC and Herschel-PACS/SPIRE. Plotted on top of the data are several well-fitting massive protostellar models, with the black line showing the model with the best fit to the data. Downward arrows denote data that were used as upper limits in the model fits due to the possible presence of PAH (Polycyclic Aromatic Hydrocarbon) contamination. (Right) A 3-color image from FORCAST data at 8, 19, and 37 µm of AFGL 437 region. The larger, brighter, red source is the source that is being studied in the SED (left panel).*

5.4 MONITORING OF THE DUST EMISSION FROM R AQUARII

- Principle Investigator: *E. Omelian (Space Science Institute)*
- Plan IDs: 04_0049, 05_0094, 06_0005, 07_0097, 09_0077

Publications:

- SOFIA/FORCAST Monitoring of the Dust Emission from R Aqr: Start of the Eclipse, R. Sankrit et al. (2022), ApJ, 926, 177

DOI: 10.3847/1538-4357/ac4792

- SOFIA/FORCAST Observations of R Aqr: Monitoring the Dust Emission, E. Omelian et al. (2020), ApJ, 898, 31
  DOI: 10.3847/1538-4357/ab9824

R Aquarii (R Aqr) is the closest dusty symbiotic star at a distance of 218 pc and consists of a mass-losing Mira variable star and a hot accreting white dwarf. Emanating from the binary is a spectacular jet which is expelled material from the accretion flow from the Mira star onto the white dwarf. It is also surrounded by two extended shells of material that were created by explosive nova-like mass-loss events that happened several hundred years ago. The Mira star in R Aqr, like many AGB (Asymptotic Giant Branch) stars, is surrounded by a shell of circumstellar material and its infrared spectrum shows the prominent silicate features at 10 and 18 µm on top of the thermal dust emission. These features are known to change in their shape with the Mira pulsation period (which is 387 days). Furthermore, the optical emission from the binary has also been seen to vary on longer timescales related to the orbital period of the binary (which is 44 years).

In 2016 and 2017, FORCAST 5-40 µm spectra were obtained of R Aqr for the first time since the observations made by the Infrared Space Observatory (ISO) in 1996. At the time of the ISO observations, the stars in the binary were near their furthest orbital separation from one another (i.e., apastron), and these new FORCAST data were taken as the system approached periastron; a time in the orbit when an increase in activity was expected. From the FORCAST data it could be seen that the mid-IR flux decreased between the time of the ISO observations and the 2016 observations just before periastron, but by 2017, the flux had started increasing again (Figure 65). Since the 2016 and 2017 observations coincided with the same phase of the Mira pulsation period, changes in the mid-infrared flux and silicate feature due to pulsation phase could be ruled out. Omelian et al. (2020) suggested initial increase in infrared flux was due to an increase in the dust production rate in the Mira star as it reached closer to apastron, and the later decrease in flux was due to the two stars becoming close enough together that the hot white dwarf winds inhibited dust formation in the circumstellar shell and winds of the Mira star.

At periastron, the white dwarf was predicted to eclipse in front of the Mira star. FORCAST 5-40 µm spectroscopic data were again obtained in 2018 and 2019 after the system had started this eclipse, and at a time during which the system became two magnitudes fainter in the optical. The mid-IR flux in 2018, in particular the 10 µm silicate feature, had strengthened compared with the previous observing epochs (Figure 65). However, the 2019 observations showed a decrease in silicate feature strength and mid-infrared flux, returning to values similar to the 2017 epoch (Figure 65). Radiative transfer models for the circumstellar dust emission were calculated by Sankrit et al. (2022) for the new spectra and they determined that the brightness variation from the Mira pulsation phase was not affected by the onset of the eclipse, and that the increase in the mid-IR flux and strength of the silicate feature in 2018 were due to a higher dust density. This higher dust density was caused by both the enhancement of the accretion flow rate from the Mira star to the white dwarf, and the orbital geometry which makes this flow and the circumstellar accretion disk around the white dwarf visible to us. It was also concluded that the extinction caused by this enhanced flow of intervening material is responsible for the accompanying decrease in visual brightness that was observed.

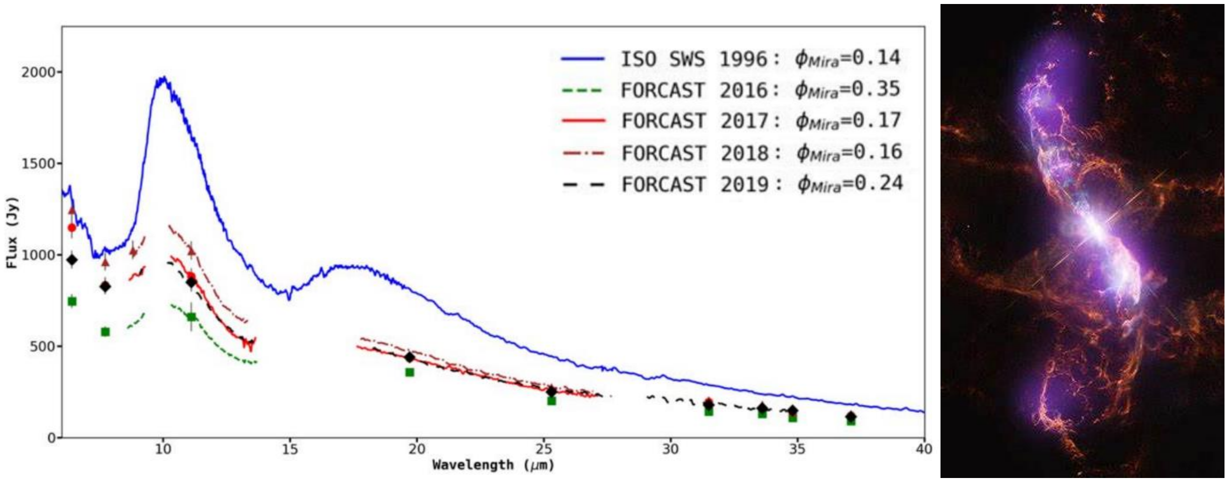

Figure 65 *(Left) Infrared spectra of R Aqr obtained with ISO and with FORCAST. The gaps in the FORCAST spectra from 9.5-10.5 μm and 14-17 μm are wavelengths where atmospheric transmission is highly variable of essentially zero. The symbols are additional FORCAST imaging photometry data with the color of these symbols matching the color of the spectral data at the same epoch (see the image legend). The phase of the pulsation period of the Mira variable at the epoch of each observation is also given in the legend. The broad peaks at 19 and 18 μm in the spectra are due to silicates. (Right) A composite image from Hubble and Chandra observatories of R Aqr showing the S-shaped outflowing jet (purple); the bright white star at the center is the optical emission from the Mira star (the white dwarf is too faint to contribute to this optical emission).*

6. REFERENCES

- Arredondo, A. et al. (2023), PASP, 135, 024501, doi: 10.1088/1538-3873/acb1d6
- De Buizer, J. et al. (2017), ApJ, 843, 33, doi: 10.3847/1538-4357/aa74c8
- Dehaes, S. et al. (2011), A&A, 533, 17, doi: 10.1051/0004-6361/200912442
- Fedriani, R. et al. (2023), ApJ, 942, 7, doi: 10.3847/1538-4357/aca4cf
- Gustafsson, B. et al. (1975), A&A, 42, 407, website: https://articles.adsabs.harvard.edu/pdf/1975A%26A....42..407G
- Gustafsson, B. et al. (2008), A&A, 486, 951, doi: 10.1051/0004-6361:200809724
- Hankins, M. et al. (2020), ApJ, 894, 55, doi: 10.3847/1538-4357/ab7c5d
- Herter, T. et al. (2013), PASP, 125, 1393, doi: 10.1086/674144
- Herter, T. et al. (2018), JAI, 7, 1840005, doi: 10.1142/S2251171718400056
- Honniball, C. et al. (2020), Nature Ast., 5, 121, doi: 10.1038/s41550-020-01222-x
- Honniball, C. et al. (2022), GRL, 49, e97786, doi: 10.1029/2022GL097786
- Liu, M. et al. (2019), ApJ, 874, 16, doi: 10.3847/1538-4357/ab07b7
- Liu, M. et al. (2020), ApJ, 904, 75, doi: 10.3847/1538-4357/abbefb
- Lord, S. (1992), NASA Technical Memorandum 103957, website: https://ntrs.nasa.gov/citations/19930010877
- Omelian, E. et al. (2020), ApJ, 898, 31, doi: 10.3847/1538-4357/ab9824
- Plez, B. et al. (1992), A&A, 256, 551, website: https://articles.adsabs.harvard.edu/pdf/1992A%26A...256..551P
- Reach, W. et al. (2023), PSJ, 4, 45, doi: 10.3847/PSJ/acbdf2
- Sankrit, R. et al. (2022), ApJ, 926, 177, doi: 10.3847/1538-4357/ac4792

APPENDIX

A. CHOPPING AND NODDING

Because the sky is so bright in the mid-infrared (MIR) relative to astronomical sources, the way in which observations are made in the MIR is considerably different from the (more familiar) way they are made in the optical. Any raw image of a region in the MIR is overwhelmed by this sky "background" emission. (The situation is like trying to observe in the optical during the day. The bright daylight sky swamps the detector and makes it impossible to see astronomical sources in the raw images.) In order to remove the background from the MIR image and detect the faint astronomical sources, observations of another region (free of sources) are made and the two images are subtracted. However, the MIR is highly variable, both spatially and – more importantly – temporally. It would take far too long (on the order of seconds) to reposition a large telescope to observe this "sky background" region: by the time the telescope had moved and settled at the new location, the sky background level would have changed so much that the subtraction of the two images would be useless. In order to avoid this problem, the secondary mirror (which is considerably smaller than the primary mirror) of the telescope is tilted, rather than moving the entire telescope. This allows observers to look at two different sky positions very quickly (on the order of a few to 10 times per second), because tilting the secondary by an angle θ moves the center of the field imaged by the detector by θ on the sky. Tilting the secondary between two positions is known as "chopping". FORCAST observations were typically made with a chopping frequency of 4 Hz. That is, every 0.25 sec, the secondary was moved between the two observing positions.

Chopping can be done either symmetrically or asymmetrically. "Symmetric chopping" means that the secondary mirror is tilted symmetrically about the telescope optical axis (also known as the boresight) in the two chop positions (Figure 66). The distance between the two chop positions is known as the chop throw. The distance between the boresight and either chop position is known as the chop amplitude and is equal to half the chop throw.

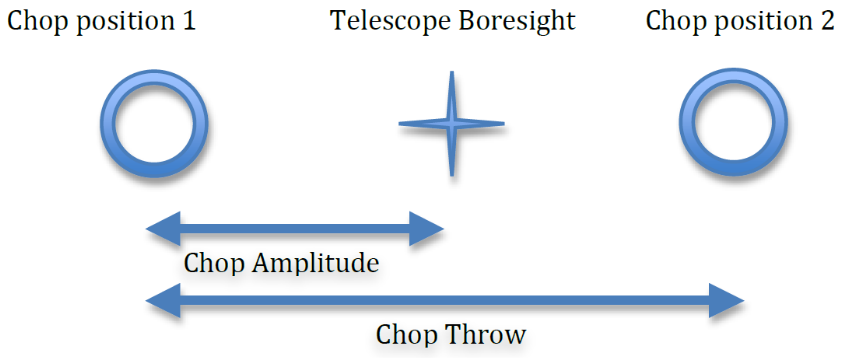

Figure 66 *Symmetric chop schematic.*

"Asymmetric chopping" means that the secondary is aligned with the telescope boresight in one position, but is tilted away from the boresight in the chop position (Figure 67). The chop amplitude is equal to the chop throw in this case.

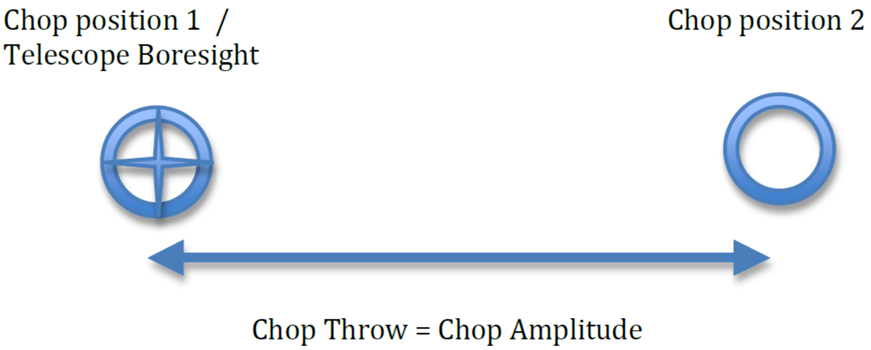

Figure 67 *Asymmetric chop schematic.*

Unfortunately, moving the secondary mirror causes the telescope to be slightly misaligned, which introduces optical distortions (notably the optical aberration known as coma) and additional background emission from the telescope (considerably smaller than the sky emission but present nonetheless) in the images. The optical distortions can be minimized by tilting the secondary only tiny fractions of a degree. The additional telescopic background can be removed by moving the entire telescope to a new position and then chopping the secondary again between two positions. (Subtracting the two chop images at this new telescope position will remove the sky emission but leave the additional telescopic background due to the misalignment; subtracting the result from the chop-subtracted image at the first telescope position will then remove the background.) Since the process of moving to a new position is needed to remove the additional background from the telescope, not the sky, it can be done on a much longer timescale. (The variation in the telescopic backgrounds occurs on timescales on the order of tens of seconds to minutes, much slower than that of the variation in the sky emission.) This movement of the entire telescope, on a much longer timescale than chopping, is known as nodding. The two nod positions are usually referred to as Nod A and Nod B. The distance between the two nod positions is known as the nod throw or the nod amplitude. For FORCAST observations, nods were done every 5 - 30 sec. The chop-subtracted images at nod position B were then subtracted from the chop-subtracted images at nod position A. The result was an image of the region, without the sky background emission or the additional emission resulting from tilting the secondary during the chopping process. The sequence of chopping in one telescope position, nodding, and chopping again in a second position is known as a chop/nod cycle.

Again, because the MIR sky is so bright, deep images of a region cannot be obtained (as they are in the optical) by simply observing the region for a long time with the detector collecting photons (integrating) continuously. As stated above, the observations require chopping and nodding at fairly frequent intervals. Hence deep observations are made by “stacking” a series of chop/nod images. Furthermore, MIR detectors are not perfect, and often have bad pixels or flaws. In order to avoid these defects on the arrays, and prevent them from marring the final images, observers employ a technique known as “dithering”. Dithering entails moving the position of the telescope slightly with respect to the center of the region observed each time a new chop/nod cycle is begun, or after several chop/nod cycles. When the images are processed, the observed region will appear in a slightly different place on the detector. This means that the bad pixels do not appear in the same place relative to the observed region. The individual images can then be registered and averaged or medianed, a process that will eliminate (in theory) the bad pixels from the final image.

A.1 Symmetric Chopping with FORCAST

FORCAST acquired astronomical observations in two symmetric chopping modes: two-position chopping with no nodding (C2) and two-position chopping with nodding (C2N). Dithering could be implemented for either of them; two-position chopping with nodding and dithering is referred to as C2ND. The most common observing methods used were C2N and C2ND. Since C2ND simply involved slight movements of the telescope position after each chop/nod cycle, the C2N mode will primarily be discussed here. FORCAST was able to make two types of C2N observations: Nod_Match_Chop and Nod_Perp_Chop. The positions of the telescope boresight, the two chop positions, and the two nod positions for these observing types are described below. FORCAST primarily used Nod_Match_Chop when chopping symmetrically.

A.1.1 Nod_Match_Chop (NMC)

In this case, the telescope was pointed at a position half of the chop throw distance away from the object to be observed and the secondary chops between two positions, one of which was centered on the object. The nod throw had the same magnitude as the chop throw (hence the name "Nod_Match_Chop") and was in a direction exactly 180° from that of the chop direction (Figure 68). The final image generated by subtracting the images obtained for the two chop positions at Nod A and those at Nod B and then subtracting the results produced three images of the star, one positive and two negatives, with the positive being twice as bright as the negatives (see also the introduction to Section 4 and Figure 22).

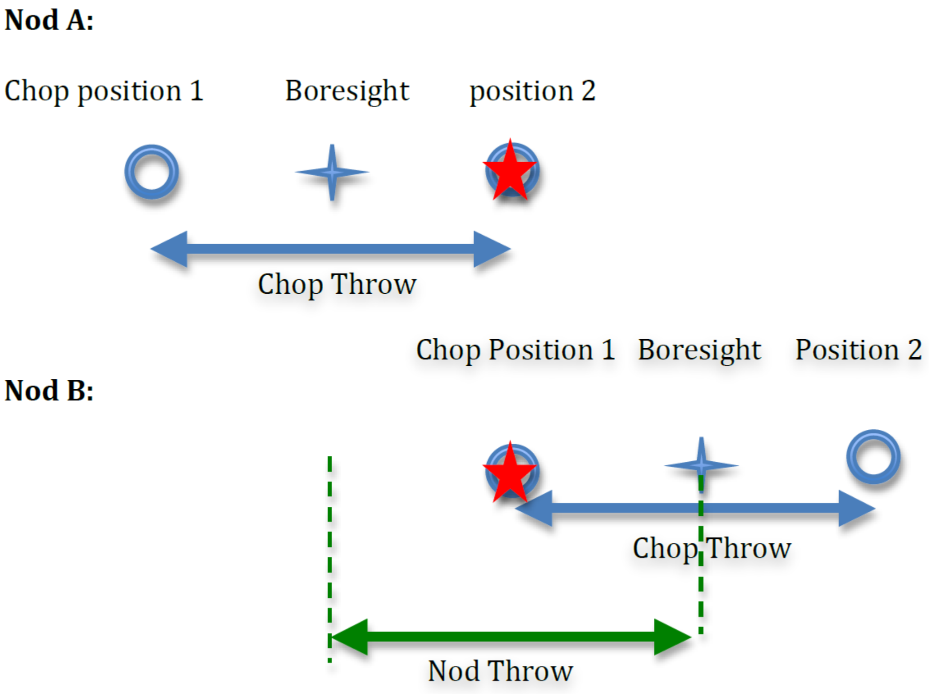

Figure 68 *Schematic of FORCAST's Nod_Match_Chop (NMC) observing mode.*

A.1.2 Nod_Perp_Chop (NPC)

In this case the telescope was offset by half the nod throw from the target in a direction perpendicular to the chop direction, and the secondary chopped between two positions. The nod throw usually (but not necessarily) had the same magnitude as the chop but was in a direction perpendicular to the chop direction (hence the name "Nod_Perp_Chop"; see Figure 69). The final image was generated by subtracting the images obtained for the two chop positions at Nod A and those at Nod B and then subtracting the results; it therefore had four images of the star in a rectangular pattern, with the image values alternating positive and negative. This method was only used in Cycles 0-2, and only very occasionally; most symmetrically chopped data were NMC.

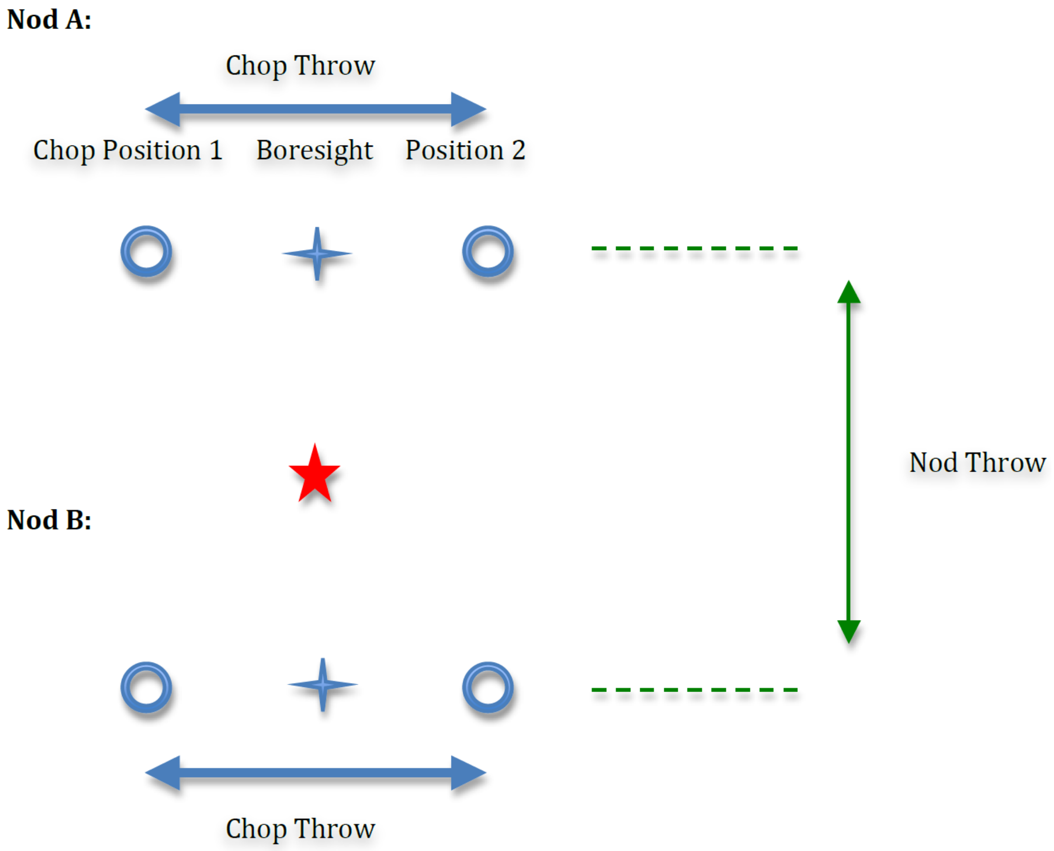

Figure 69 *Schematic of FORCAST's Nod_Perp_Chop (NMC) observing mode.*

A.2 Asymmetric Chopping with FORCAST (C2NC2)

FORCAST also had an asymmetric chop mode, known as C2NC2. In this mode, the telescope was first pointed at the target (position A). In this first position, the secondary was aligned with the optical axis (or boresight) for one observation and then was tilted some amount (often 180-480 arcseconds) for the second (asymmetrically chopped) observation. This was an asymmetric C2 mode observation. The telescope was then slewed some (usually large) amount away from the target, typically to some sky region without sources (position B), and the asymmetric chop pattern was repeated (Figure 70). C2NC2 observations were taken as a series of up to 8 (C2) files in the sequence A B A A B A A B. Again, the time between slews was typically 30 seconds.

For more on how the data are saved in these symmetric and asymmetric modes see the introduction to Section 4.

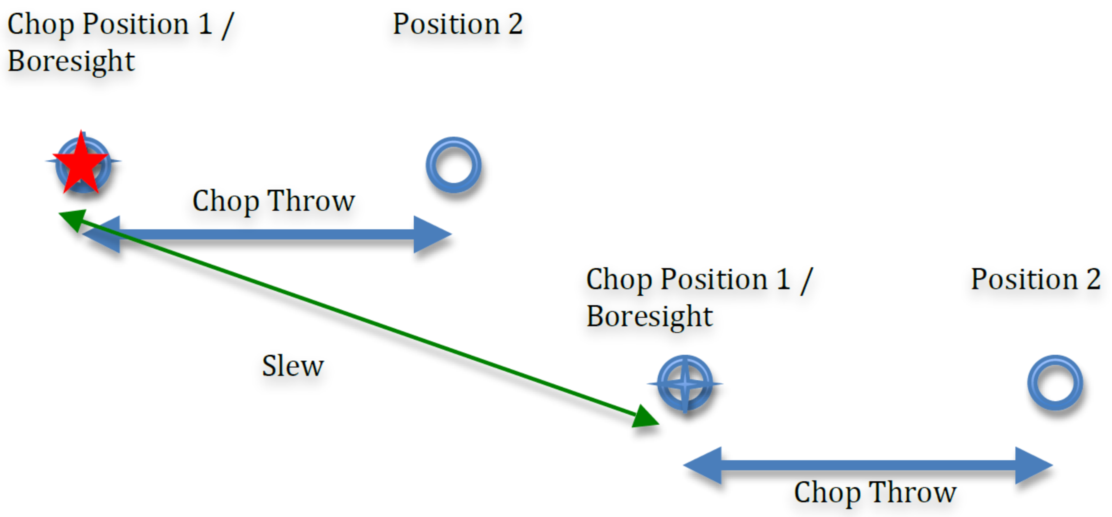

Figure 70 *Schematic of FORCAST's C2NC2 observing mode.*

B. FORCAST FILTER COLOR CORRECTIONS AND CENTRAL WAVELENGTHS

Table 14: Color Corrections, K, for FORCAST Filters

	Single channel (λ) (μm)																	
	F054	F056	F064	F066	F077	F086	F088	F111	F112	F113	F118	F197	F242	F253	F254	F315	F336	F348	F371
α = -4	1.000	1.000	1.000	1.000	1.000	1.000	1.131	1.002	1.014	1.000	1.001	1.018	1.013	1.002	1.002	1.012	1.007	1.009	1.007
α = -3	1.000	1.000	1.000	1.000	1.000	1.000	1.027	1.001	1.005	1.000	1.000	1.006	1.004	1.001	1.001	1.004	1.002	1.003	1.002
α = -2	1.000	1.000	1.000	1.000	1.000	1.000	1.000	1.000	1.000	1.000	1.000	1.000	1.000	1.000	1.000	1.000	1.000	1.000	1.000
α = -1	1.000	1.000	1.000	1.000	1.000	1.000	1.000	1.000	1.000	1.000	1.000	1.000	1.000	1.000	1.000	1.000	1.000	1.000	1.000
α = 0	1.000	1.000	1.000	1.000	1.000	1.000	1.011	1.001	1.005	1.000	1.000	1.006	1.004	1.001	1.001	1.004	1.003	1.003	1.003
α = 1	1.000	1.000	1.000	1.000	1.001	1.000	1.026	1.002	1.014	1.000	1.001	1.017	1.012	1.002	1.002	1.013	1.010	1.011	1.010
α = 2	1.001	1.000	1.000	1.001	1.002	1.000	1.046	1.004	1.029	1.000	1.003	1.034	1.025	1.004	1.004	1.027	1.023	1.024	1.022
α = 3	1.001	1.001	1.000	1.001	1.004	1.001	1.070	1.007	1.049	1.000	1.005	1.053	1.044	1.007	1.007	1.053	1.048	1.049	1.049
T = 10000 K	1.001	1.000	1.000	1.001	1.002	1.000	1.044	1.004	1.027	1.000	1.003	1.033	1.025	1.004	1.004	1.026	1.023	1.024	1.022
T = 5000 K	1.000	1.000	1.000	1.001	1.002	1.000	1.042	1.004	1.026	1.000	1.003	1.032	1.024	1.004	1.004	1.026	1.022	1.023	1.021
T = 3000 K	1.000	1.000	1.000	1.000	1.001	1.000	1.039	1.003	1.024	1.000	1.003	1.031	1.023	1.004	1.004	1.025	1.022	1.022	1.021
T = 1000 K	1.000	1.000	1.000	1.000	1.001	1.000	1.024	1.002	1.015	1.000	1.002	1.026	1.020	1.003	1.003	1.021	1.018	1.019	1.018
T = 750 K	1.000	1.000	1.000	1.000	1.000	1.000	1.016	1.001	1.010	1.000	1.001	1.023	1.018	1.003	1.003	1.019	1.017	1.018	1.016
T = 500 K	1.000	1.000	1.000	1.000	0.999	1.000	1.001	1.000	1.001	1.000	1.000	1.016	1.014	1.002	1.002	1.016	1.013	1.015	1.013
T = 300 K	1.001	1.000	1.000	1.000	0.999	1.000	0.974	0.999	0.990	1.000	0.999	1.003	1.007	1.001	1.001	1.010	1.008	1.009	1.008
T = 200 K	1.003	1.002	1.001	1.002	1.017	1.000	0.961	0.999	0.993	1.000	0.999	0.991	0.999	1.000	1.000	1.003	1.002	1.003	1.003

	Dual channel (λ) (μm)																	
	F054	F056	F064	F066	F077	F086	F088	F111	F112	F113	F118	F197	F242	F253	F254	F315	F336	F348	F371
α = -4	1.000	1.000	1.000	1.001	1.000	1.000	1.002	1.002	1.011	1.000	1.001	1.018	1.005	1.002	1.002	1.011	1.003	1.007	1.005
α = -3	1.000	1.000	1.000	1.000	1.000	1.000	1.000	1.001	1.004	1.000	1.000	1.006	1.002	1.001	1.001	1.004	1.001	1.002	1.002
α = -2	1.000	1.000	1.000	1.000	1.000	1.000	1.000	1.000	1.000	1.000	1.000	1.000	1.000	1.000	1.000	1.000	1.000	1.000	1.000
α = -1	1.000	1.000	1.000	1.000	1.000	1.000	1.000	1.000	1.000	1.000	1.000	1.000	1.000	1.000	1.000	1.000	1.000	1.000	1.000
α = 0	1.000	1.000	1.000	1.000	1.000	1.000	1.000	1.001	1.004	1.000	1.000	1.006	1.002	1.001	1.001	1.004	1.001	1.002	1.002
α = 1	1.000	1.000	1.000	1.001	1.001	1.000	1.001	1.002	1.011	1.000	1.001	1.017	1.006	1.002	1.002	1.011	1.003	1.007	1.006
α = 2	1.001	1.001	1.000	1.001	1.002	1.000	1.002	1.003	1.022	1.000	1.002	1.034	1.012	1.004	1.004	1.021	1.006	1.014	1.011
α = 3	1.001	1.001	1.000	1.002	1.004	1.001	1.004	1.005	1.038	1.000	1.004	1.053	1.022	1.007	1.007	1.032	1.010	1.024	1.020
T = 10000 K	1.001	1.000	1.000	1.001	1.002	1.000	1.002	1.003	1.021	1.000	1.002	1.033	1.011	1.004	1.004	1.020	1.006	1.014	1.011
T = 5000 K	1.000	1.000	1.000	1.001	1.002	1.000	1.002	1.003	1.020	1.000	1.002	1.032	1.011	1.004	1.004	1.020	1.006	1.013	1.011
T = 3000 K	1.000	1.000	1.000	1.001	1.001	1.000	1.002	1.003	1.019	1.000	1.002	1.031	1.011	1.004	1.004	1.020	1.006	1.013	1.011
T = 1000 K	1.000	1.000	1.000	1.000	1.001	1.000	1.001	1.002	1.012	1.000	1.001	1.026	1.009	1.003	1.003	1.018	1.005	1.012	1.010
T = 750 K	1.000	1.000	1.000	1.000	1.000	1.000	1.000	1.001	1.008	1.000	1.001	1.023	1.008	1.003	1.003	1.017	1.005	1.011	1.009
T = 500 K	1.000	1.000	1.000	1.000	0.999	1.000	1.000	1.000	1.001	1.000	1.000	1.016	1.007	1.002	1.002	1.014	1.004	1.010	1.008
T = 300 K	1.001	1.000	1.000	1.000	0.999	1.000	0.999	0.999	0.992	1.000	0.999	1.003	1.004	1.001	1.001	1.009	1.003	1.007	1.006
T = 200 K	1.003	1.002	1.001	1.003	1.018	1.000	1.001	0.999	0.995	1.000	0.999	0.991	1.000	1.000	1.000	1.003	1.001	1.003	1.003

Note - The factor K converts an input flux density to that of a nominal 'flat spectrum' source at the mean wavelength of the filter. The input spectral shape is described by a power law ($F_\nu \propto \nu^\alpha$*) or a blackbody with temperature T.*

Table 15: Mean and Pivot Wavelengths for FORCAST Filters

	Single channel (λ) (μm)																		
	F054	F056	F064	F064	F077	F086	F088	F111	F112	F113	F118	F197	F242	F253	F254	F315	F336	F348	F371
Pivot λ	5.356	5.609	6.348	6.613	7.702	8.604	8.757	11.085	11.211	11.342	11.794	19.642	24.869	25.233	25.400	31.333	33.380	34.619	37.071
Meanλ	5.356	5.610	6.348	6.613	7.700	8.605	8.803	11.089	11.237	11.342	11.796	19.699	24.920	25.241	25.409	31.397	33.430	34.677	37.124
	Dual channel (λ) (μm)																		
	F054	F056	F064	F064	F077	F086	F088	F111	F112	F113	F118	F197	F242	F253	F254	F315	F336	F348	F371
Pivot λ	5.363	5.613	6.351	6.619	7.723	8.662	8.641	11.008	11.117	11.305	11.894	19.642	27.653	25.233	26.243	31.305	33.551	34.601	36.949
Meanλ	5.363	5.614	6.351	6.620	7.721	8.662	8.643	11.011	11.137	11.305	11.897	19.699	27.679	25.241	26.252	31.362	33.567	34.640	36.983

C. IMPORTANT FORCAST HEADER KEYWORDS

Some of the more important header entries for FORCAST are explained below. The common values the header keywords have for science data are also provided. Other values may be possible, but only in engineering data. Review of other general keywords in the header that are not specific to FORCAST or not covered below are in the *SOFIA FITS Keyword Dictionary* available at the IRSA SOFIA Data Processing website.

The header information below is divided into major subsections of the FORCAST header, which are demarcated in the headers with the same names as the table titles. FORCAST was one of the first instruments used for commissioning the observatory, and as the observatory software changed over time, housekeeping data and FITS keywords were added or modified. Old keywords were kept for backwards compatibility, but over time became antiquated. Keywords below that may not be reliable or have been changed over time are marked with an asterisk and a comment containing further information.

--- DCS DATA COLLECTION ---		
FITS Keyword	Value	Description
CHOPPING	T/F	T if telescope was chopping during observation (should never be F)
NODDING	T/F	T if telescope was nodding during observation (this will rarely be F)
DITHER	T/F	T if telescope was dithering during observation
MAPPING	T/F	Should always be F (FORCAST does not utilize the telescope's default mapping functionality)
SCANNING	T/F	Should always be F (FORCAST does not utilize the telescope's default scanning functionality)
NONSIDE	T/F	This will be set to T if the target being observed is a non-sidereal target
--- DCS INSTRUMENT ---		
FITS Keyword	Value	Description
DATATYPE	IMAGE SPECTRAL OTHER	IMAGE for imaging observations, SPECTRAL for grism observations. Other may include special modes.
INSTCFG	IMAGING_SWC	FORCAST instrument configuration: IMAGING_SWC is single-channel SWC imaging,

	IMAGING_LWC IMAGING_DUAL GRISM_SWC GRISM_LWC	IMAGING_LWC is single-channel LWC imaging, IMAGING_dual is dual-channel simultaneous imaging with dichroic, GRISM_SWC is single-channel grism observing in the SWC, GRISM_LWC is single-channel grism observing in the LWC
INSTMODE	C2N C2NC2 NXCAC SLITSCAN	Mode of data collection: 2-position chop and nod symmetrical (C2N, or NMC), 2-position chop and nod asymmetrical with large chops (C2NC2), Spectroscopic version of C2NC2 (NXCAC), and stepping across sky using the slit.(SLITSCAN)
*TOTINT	[FLOAT]	Total integration time in seconds. If SKYMODE is C2NC2 or NXCAC, then TOTINT = DETITIME * 0.5, otherwise TOTINT = DETITIME*2.0. This time was used to account for times calculated in SITE and SSPOT tool. EXPTIME should be used for science.
*EXPTIME	[FLOAT]	Nominal on-source integration time, include throwaways. This is the time that should be used for science. Tracked as of FORCAST Redux v1.0.4 (2015-05-14).
DETITIME	[FLOAT]	Detector integration time, discounting chop transition throw away frames.
*INTTIME	[FLOAT]	Deprecated timekeeping device similar to DETITIME, but calculated incorrectly for several cycles. Use DETITIME instead.
FRMTIME	[FLOAT]	Time for a single frame readout in milliseconds. The fastest possible is 1.966 ms (~508Hz). These frames are then co-added in hardware by the number of coadds (NCOADDS) at each chop position.
SPECTEL1	FOR_F054 FOR_F056 FOR_F064 FOR_F066 FOR_F077 FOR_F088 FOR_F111 FOR_F112 FOR_F197 FOR_F242 FOR_F253	Filter or grism present in SWC during observation

	FOR_G063 FOR_G111	
SPECTEL2	FOR_F113 FOR_F118 FOR_F242 FOR_F254 FOR_F315 FOR_F336 FOR_F348 FOR_F371 FOR_G227 FOR_G329	Filter or grism present in LWC during observation
SLIT	NONE FOR_LS24 FOR_LS47	Spectroscopic slit present during observation
WAVELNTH	[FLOAT]	Nominal filter or grism central wavelength (usually same as filter name)
WAVECENT	[FLOAT]	Calculated mean wavelength of the filter or grism based upon instrument throughput
*DETCHAN	SW, LW	Detector channel used for this image, either LWC (LW) or SWC (SW). Prior to FORCAST Redux v1.0.7 (2015-09-03), this keyword was set to 0 (SW) or 1 (LW).
BANDWDTH	[FLOAT]	Approximate filter or grism bandwidth (see Section 2.2)
--- DCS ARRAY DETECTOR ---		
FITS Keyword	Value	Description
DETECTOR	As-010, Sb-083	As-010 is the SWC detector name, Sb-083 is the LWC detector name
PIXSCAL	[FLOAT]	The pixel scale for FORCAST should always be 0.768 arcseconds per pixel after distortion correction
--- DCS CHOPPING ---		
FITS Keyword	Value	Description
CHPFREQ	[FLOAT]	Full cycle chop rate in Hz

*CHPSYM	SYM ASYM	Chop symmetry: SYM means chopping symmetrically about optical axis, ASYM is asymmetrically chopping. However, this keyword was deprecated and is incorrect for later cycles. Use INSTMODE as C2, C2N are SLITSCAN are symmetrical while C2NC2 and NXCAC are asymmetrical.
CHPAMP1	[FLOAT]	Amplitude of chop with respect to the optical axis in arcseconds. If CHPSYM=ASYM, then CHPAMP1 and CHPAMP2 will have different values for the amplitude to one side of the optical axis and the other. If CHPSYM=SYM, then CHPAMP1 gives the amplitude to both sides of the optical axis and CHPAMP2 is set to 0. The total “Chop Throw” is 2X CHPAMP1
CHPAMP2	[FLOAT]	
CHPCRSYS	ERF SIRF	This the coordinate systems the chopping is being defined in: ERF is the Equatorial Reference Frame (aka Sky coordinates) and SIRF is the Science Instrument Reference Frame (aka Array coordinates)
CHPANGLE	[FLOAT]	Actual chop angle in degrees in the CHPCRSYS coordinate system measured by telescope encoders
CHPCOORD	0, 1, 2	Redundant with the CHPCRSYS keyword. 0=SIRF 1=TARF 2=ERF
CHPANGLR	[FLOAT]	Deprecated header value. Use CHPANGLE keyword for actual chop angle used during observation
CHPASYM	T/F	T is chopping is asymmetric. Redundant with CHPSYM
--- DCS NODDING ---		
FITS Keyword	Value	Description
NODTIME	[FLOAT]	Integration time at each nod position. Because of inefficiencies, this will be less than the “nod dwell time” which is the wallclock time spent in each nod position.
NODN	[INTEGER]	Number of nods requested
NODAMP	[FLOAT]	Total distance telescope nodded in arcsec (aka “nod throw” since it is not really an amplitude)

NODPATT	AB ABBA ABA	Nod cycle pattern between the two nod positions, A and B.
*NODSTYLE	NMC NPC C2NC2 NXCAC	Deprecated keyword. SKYMODE keyword essentially replaced this keyword for keeping track of observing mode, but this may be useful for very old data.
NODCRSYS	ERF SIRF	This is the coordinate system the nodding is being defined in: ERF is the Equatorial Reference Frame (aka Sky coordinates) and SIRF is the Science Instrument Reference Frame (aka Array coordinates)
NODANGLE	[FLOAT]	Actual nod angle in degrees in the NODCRSYS coordinate system measured by telescope encoders
NODCOORD	0, 1, 2	Redundant with the NODCRSYS keyword. 0=SIRF 1=TARF 2=ERF
NODANGLR	[FLOAT]	Deprecated header value. Use NODANGLE keyword for actual nod angle used during observation
--- NON-DCS —		
FITS Keyword	Value	Description
BORESITE	IMAGING LONGSLIT	Position of alignment between telescope and instrument. IMAGING and LONGSLIT was set by Tables in Section 4.5.1.16 (Boresight Misaligned). IMAGING was set near center of array while LONGSLIT was set towards the top of the array to avoid some bad pixels. LONGSLIT was the position used for imaging setup to align the source on the slit and the following grism observations.
TRACKING	T/F	T means that guiding (tracking) was on during observation.
TRACKCAM	FPI FFI WFI	Guide camera used for tracking. FPI has the greatest stability (sub-arcsecond accuracy), the FFI has a couple arcsecond accuracy, and WFI has many arcseconds accuracy.
SKYMODE	NMC NPC C2NC2	The chop-nod style: NMC is Nod Match Chop (C2N), NPC is Nod Perpendicular to Chop (C2N), C2NC2 is

	NXCAC	asymmetric mode for imaging while NXCAC is asymmetric mode for spectroscopy.
SKY_ANGL	[FLOAT]	Direction the y-axis of the FORCAST array (i.e. “up”) is oriented with respect to North on the sky
--- PIPELINE RELATED KEYWORDS (IMAGING) —		
FITS Keyword	Value	Description
ASSC_AOR	STRING	All input AOR-IDs. Added with FORCAST Redux v1.0.4 (2015-05-14)
ASSC_OBS	STRING	All input OBS-IDs. Added with FORCAST Redux v1.3.1 (2018-03-08)
ASSC_MSN	STRING	All input MISSN-IDs. Added with FORCAST Redux v1.3.1 (2018-03-08) for mosaics.
CALFCTR	[FLOAT]	Calibration factor (Me/s/Jy), same as the “reference calibration factor” given in the HISTORY section of the header. Used as a divider for COA imaging files to convert to CAL files.
ERRCALF	[FLOAT]	Calibration factor uncertainty (Me/s/Jy)
LAMREF	[FLOAT]	Reference wavelength (microns), as given in Table 15.
LAMPIVOT	[FLOAT]	Pivot wavelength (microns), as given in Table 15.
COLRCORR	[FLOAT]	Color correction factor
--- PIPELINE RELATED KEYWORDS (GRISM) —		
FITS Keyword	Value	Description
SLIT	FOR_LS24 FOR_LS47	Grism slit identification. Long (LS) or short (SS). Narrow (24) or wide (47).
SLTW_ARC	[FLOAT]	Slit width on sky in arcsec
SLTW_PIX	[FLOAT]	Slit width on array in pixels
RP	[FLOAT]	Resolving power of grism and slit being used
APPOS001	[FLOAT]	Aperture centroid measured in arcsec used to extract the spectrum.

APFWHM01	[FLOAT]	Assumed FWHM used to extract the spectrum
APRAD01	[FLOAT]	Extraction aperture radii in arcsec
PSFRAD01	[FLOAT]	Extraction aperture PSF radii in arcsec
BGR	STRING	Location of the regions used for background subtraction
ORDERFILE	STRING	Filename used to identify the spectral order edges
WAVEFILE	STRING	Filename identifying the wavelength calibration map used to calibrate the data.
SLITFILE	STRING	Filename identifying the spatial calibration map used to calibrate the data.
ATRNFILE	STRING	Filename identifying the ATRAN model file used to do telluric subtraction
WAVSHIFT	FLOAT	Wavelength shift used to shift the MRG file compared to the ATRAN model for optimal telluric subtraction.
RSPNFILE	STRING	Filename identifying the response curve used to flux calibrate the data
XUNITS	STRING	Units of the wavelength axis e.g., µm
YUNITS	STRING	Units of the spatial axis e.g., arcsec

C1. HISTORY Section of Imaging Headers

Below is an example of selected parts of the HISTORY section at the bottom of the FORCAST imaging headers containing information that may be of importance or require further explanation. This section of the FITS headers is annotated with explanations.

```
HISTORY Reference ZA=45.0, altitude=41.0
HISTORY Telluric correction factor for ZA=40.16, altitude=38.583:
HISTORY   1.0089188334485866

HISTORY Flux calibration information:
HISTORY   Using reference file: forcast/ref_calfctr/refcalfac_20220219.txt
HISTORY   Average reference calibration factor:
HISTORY     0.163834 +/- 0.002273
HISTORY Data has been divided by cal factor to convert
HISTORY   from Me/s to Jy

DATAQUAL= 'USABLE  '
CALQUAL = 'NOMINAL '
HISTORY
```

< The data in Me/s were multiplied by this value to correct for airmass.

< The data in Me/s were divided by this number to get the calibrated data in Jy. The error provided here is the measurement error from all calibrators used in the calculation.

```
HISTORY Headers updated by jradomsk, 2022-04-25T10:12:39
HISTORY
HISTORY Notes from quality analysis
HISTORY ---------------------------
HISTORY Files #2-3 lost position and alignment resulting in multiple
HISTORY sources,  these files were excluded from processing. All standard
HISTORY stars observed using the FOR_F253 filters show a streak-like
HISTORY structure that becomes worse on the lower portion of the array.
HISTORY The overall flux of the streak varies from a few percent to as
HISTORY much as ~10% of the peak of the star. This structure is NOT
HISTORY observed in asteroid calibrators indicating that it may be
HISTORY associated with a short wavelength light leak in the filter.
HISTORY Observations of sources with SEDs that peak at wavelengths
HISTORY shorter than 25.3 microns may be most affected. Users are
HISTORY cautioned to look at corresponding standards to evaluate the
HISTORY effect on their data on a case by case basis. Please see the
HISTORY Known Issues documentation for more details.
HISTORY
HISTORY   DATAQUAL: None -> USABLE
HISTORY   CALQUAL: None -> NOMINAL
```

< This section has detailed notes of any problems with the data. Refer to the descriptions of Known Issues in Section 434.5.1 and check the data issues by Cycle/Flight Series (Table 16).

< Final assessment of data quality and calibration quality

One change to the HISTORY section occurred in 2023, where the data for Cycles 5-9 were reprocessed and the first three HISTORY lines shown above were changed to account for precipitable water vapor (PWV) and look instead like the example below:

```
HISTORY Reference ZA=45.0, PWV=7.3
HISTORY Telluric correction factor for ZA=41.94, PWV=7.745906670297863:
HISTORY 1.0025019575361516
HISTORY -- Pipeline step: Telluric Correct
HISTORY Parameters:
HISTORY save = True
HISTORY use_wv = True
```

< The data in Me/s were multiplied by this value to correct for airmass and PWV.

C2. HISTORY Section of Grism Headers

Below is an example of selected parts of the HISTORY section at the bottom of the FORCAST headers with specific information that may be of importance for grism data. This section is annotated with explanations.

```
HISTORY -- Pipeline step: Make Profiles
HISTORY Parameters:
HISTORY   save = True
HISTORY   wavefile = /dps/pipelines/forcast/redux/2.7.0/pyforcast/sofia_redux/in
HISTORY struments/forcast/data/grism/wave_cal/v2.0.0/G111_wavecal_OC2.fits
HISTORY   slitfile = /dps/pipelines/forcast/redux/2.7.0/pyforcast/sofia_redux/in
HISTORY struments/forcast/data/grism/slit_function/G111_LS24_slitfn_OC2.fits
```

< The wavelength and spatial calibration files used to calibrate the data.

```
HISTORY -- Pipeline step: Calibrate Flux
HISTORY Parameters:
HISTORY   save = True
HISTORY   save_1d = False
HISTORY   skip_cal = False
HISTORY   respfile = /dps/pipelines/forcast/redux/2.7.0/pyforcast/sofia_redux/in
HISTORY
struments/forcast/data/grism/response/v5.1.0/G111_LS24_DB175_RSP.fits
HISTORY   resolution = 256.0
HISTORY   optimize_atran = False
HISTORY   atrandir = $DPS_SHARE/calibrations/ATRAN/fits
HISTORY   atranfile =
HISTORY   use_wv = False
HISTORY   sn_threshold = 10.0
HISTORY   auto_shift = False
HISTORY   auto_shift_limit = 2.0
HISTORY   waveshift = 0.0
HISTORY   model_order = 1
```

< Response and ATRAN files (if data reduced manually) used to calibrate the spectrum. Also includes information about wavelength shift and polynomial model orders used for telluric subtraction.

D. TABLES OF KNOWN FORCAST DATA ISSUES

This section contains two tables describing the known issues with FORCAST data. The first table, Table 16, lists the data issues encountered by FORCAST flight series and by mission ID (the last three digits of which are the flight number). Table 17 lists all of the imaging and grism issues with descriptions and gives the flight series in which they may be encountered. Table 16 issues are hyperlinked to their descriptions in Table 17.

Table 16: Known FORCAST Data Issues by Flight Series and Mission ID/Flight Number

SERIES	MISSION ID	ISSUES
OC1B	2013-06-21_FO_F108, 2013-06-26_FO_F109, 2013-07-02_FO_F110	IMG_01, IMG_02, IMG_03, IMG_04A, IMG_09, IMG_10 GRI_02, GRI_03, GRI_05,GRI_06, GRI_07
OC1D&F	2013-09-10_FO_F128, 2013-09-12_FO_F129, 2013-09-13_FO_F130, 2013-09-17_FO_F131, 2013-09-19_FO_F132, 2013-10-25_FO_F135	IMG_03, IMG_04A, IMG_09, IMG_10 GRI_02, GRI_03, GRI_05, GRI_06, GRI_07
OC2B	2014-03-20_FO_F153, 2014-03-22_FO_F154, 2014-03-25_FO_F155, 2014-03-27_FO_F156, 2014-03-29_FO_F157	IMG_04A, IMG_09, IMG_10 GRI_02, GRI_08
OC2D	2014-05-01_FO_F165, 2014-05-02_FO_F166, 2014-05-03_FO_F167, 2014-05-06_FO_F168, 2014-05-07_FO_F169, 2014-05-08_FO_F170	IMG_04A, IMG_06, IMG_09, IMG_10 GRI_01, GRI_02, GRI_04, GRI_10
OC2F	2014-06-04_FO_F176, 2014-06-06_FO_F177, 2014-06-11_FO_F178, 2014-06-13_FO_F179	
OC2H	2015-01-29_FO_F190, 2015-02-04_FO_F191, 2015-02-05_FO_F192, 2015-02-06_FO_F193	IMG_04B, IMG_05,IMG_08, IMG_09, IMG_10 GRI_01, GRI_02, GRI_04, GRI_09, GRI_10
OC3C	2015-05-29_FO_F211, 2015-05-30_FO_F212, 2015-06-03_FO_F214, 2015-06-04_FO_F215, 2015-06-05_FO_F216, 2015-06-13_FO_F217	
OC3D	2015-06-19_FO_F219, 2015-06-23_FO_F220, 2015-06-24_FO_F221, 2015-06-28_FP_F222, 2015-07-03_FO_F224, 2015-07-04_FO_F225, 2015-07-06_FO_F226, 2015-07-07_FO_F227	

Table 16: Continued

SERIES	MISSION ID	ISSUES
OC3I	2015-09-11_FO_F238, 2015-09-16_FO_F239, 2015-09-17_FO_F240, 2015-09-18_FO_F241, 2015-09-22_FO_F242	IMG_04B, IMG_05,IMG_08, IMG_09, IMG_10 GRI_01, GRI_02, GRI_04, GRI_10
OC3L	2015-11-04_FO_F254, 2015-11-05_FO_F255, 2015-11-06_FO_F256, 2015-11-10_FO_F257, 2015-11-13_FO_F258, 2015-11-14_FO_F259, 2015-11-19_FO_F260, 2015-11-20_FO_F261	IMG_04C, IMG_05, IMG_07,IMG_08, IMG_09, IMG_10 GRI_01, GRI_02, GRI_04, GRI_10
OC4A	2016-02-04_FO_F272, 2016-02-05_FO_F273, 2016-02-06_FO_F274, 2016-02-09_FO_F275, 2016-02-10_FO_F276, 2016-02-11_FO_F277, 2016-02-17_FO_F278, 2016-02-18_FO_F279	IMG_04D, IMG_05, IMG_08, IMG_09, IMG_10 GRI_01, GRI_02, GRI_04, GRI_10
OC4G	2016-07-11_FO_F318, 2016-07-12_FO_F319, 2016-07-13_FO_F320, 2016-07-14_FO_F321, 2016-07-17_FO_F322, 2016-07-18_FO_F323, 2016-07-19_FO_F324, 2016-07-20_FO_F325	IMG_08 GRI_01, GRI_02, GRI_04, GRI_10
OC4I	2016-09-17_FO_F329, 2016-09-20_FO_F330, 2016-09-21_FO_F331, 2016-09-22_FO_F332, 2016-09-27_FO_F333	IMG_05, IMG_08 GRI_01, GRI_02, GRI_04, GRI_10
OC5J	2017-08-02_FO_F425, 2017-08-03_FO_F426, 2017-08-06_FO_F427, 2017-08-07_FO_F428	IMG_08, IMG_10, IMG_11, IMG_12, IMG_13 GRI_01, GRI_02, GRI_04, GRI_10, GRI_11
OC5K	2017-09-21_FO_F432, 2017-09-26_FO_F433, 2017-09-27_FO_F434, 2017-09-28_FO_F435	IMG_13 GRI_01, GRI_02, GRI_04, GRI_10

Table 16: Continued

SERIES	MISSION ID	ISSUES
OC6J	2018-08-22_FO_F492, 2018-08-23_FO_F493, 2018-08-24_FO_F494, 2018-08-25_FO_F495, 2018-08-28_FO_F496, 2018-08-29_FO_F497, 2018-08-30_FO_F498, 2018-08-31_FO_F499, 2018-09-06_FO_F500, 2018-09-07_FO_F501, 2018-09-08_FO_F502, 2018-09-10_FO_F503	IMG_14, IMG_15, IMG_16, IMG_19 GRI_01, GRI_02, GRI_04, GRI_10
OC7D	2019-07-01_FO_F588, 2019-07-02_FO_F589, 2019-07-03_FO_F590, 2019-07-04_FO_F591, 2019-07-08_FO_F592, 2019-07-09_FO_F593, 2019-07-10_FO_F594, 2019-07-11_FO_F595	IMG_17, IMG_19, IMG_20 GRI_01, GRI_02, GRI_04, GRI_10, GRI_12
OC7G	2019-10-15_FO_F622, 2019-10-16_FO_F623, 2019-10-17_FO_F624, 2019-10-18_FO_F625, 2019-10-22_FO_F627, 2019-10-23_FO_F628, 2019-10-24_FO_F629, 2019-10-25_FO_F630	IMG_17, IMG_19, IMG_20 GRI_01, GRI_02, GRI_04, GRI_10, GRI_12
OC8I	2021-04-07_FO_F713, 2021-04-08_FO_F714, 2021-04-09_FO_F715	IMG_18, IMG_20 GRI_01, GRI_02, GRI_04, GRI_10
OC8O	2021-06-23_FO_F751, 2021-06-30_FO_F752, 2021-07-01_FO_F753, 2021-07-02_FO_F754	IMG_18, IMG_20 GRI_01, GRI_02, GRI_04, GRI_10
OC9A	2021-07-07_FO_F755, 2021-07-08_FO_F756, 2021-07-09_FO_F757	IMG_18, IMG_20 GRI_01, GRI_02, GRI_04, GRI_10
OC9J	2022-01-25_FO_F814, 2022-01-26_FO_F815, 2022-01-27_FO_F816, 2022-02-01_FO_F817, 2022-02-02_FO_F818, 2022-02-03_FO_F819, 2022-02-04_FO_F820, 2022-02-08_FO_F821, 2022-02-09_FO_F822, 2022-02-10_FO_F823, 2022-02-16_FO_F825, 2022-02-17_FO_F826, 2022-02-18_FO_F827, 2022-02-19_FO_F828	IMG_18, IMG_20 GRI_01, GRI_02, GRI_04, GRI_10

Table 16: Continued

SERIES	MISSION ID	ISSUES
OC9P	2022-05-11_FO_F867, 2022-05-12_FO_F868, 2022-05-13_FO_F869, 2022-05-17_FO_F870, 2022-05-18_FO_F871, 2022-05-19_FO_F872, 2022-05-20_FO_F873, 2022-05-24_FO_F875, 2022-05-25_FO_F876, 2022-05-26_FO_F877, 2022-05-27_FO_F878	IMG_18, IMG_20 GRI_01, GRI_02, GRI_04, GRI_10
OC9V	2022-09-07_FO_F910, 2022-09-08_FO_F911, 2022-09-09_FO_F912, 2022-09-14_FO_F913, 2022-09-15_FO_F914, 2022-09-17_FO_F915	IMG_18, IMG_20 GRI_01, GRI_02, GRI_04, GRI_10

Table 17: Descriptions of Known FORCAST Data Issues

MODE	ISSUES	SERIES
Imaging	**[IMG_01] Smearing due to incorrect chop settle time (F108, F109):** For some of the observations on flights 108 and 109, the chop settle time was set incorrectly resulting in some chop smear in the images; see QA notes for further information.	OC1B
	[IMG_02] Flaring in observations using Barr #3 dichroic: Some of the observations taken with the Barr #3 dichroic suffered from significant flaring (the Barr #3 has been discontinued). Affected observations are indicated in the AOR QA notes.	OC1B
	[IMG_03] Elongated PSF: The PSF is significantly elongated in the cross-elevation direction. The axis ratio of point sources is typically 1.3.	OC1B, OC1D&F
	[IMG_04A] WCS Incorrect (A): The WCS solution provided with the data is inaccurate because the secondary mirror offsets are not accounted for correctly yet. Errors are of order the chop/nod amplitude: typically 30″ in NMC mode, and as much as 200–400″ for C2NC2 mode.	OC1B, OC1D&F, OC2B, OC2D, OC2F
	[IMG_04B] WCS Incorrect (B): For NMC mode, the WCS solution provided with the data has been corrected using the requested coordinates (OBSRA/OBSDEC) and is likely to be correct. However, since there is no way to independently verify, the quality of the WCS is still marked as UNKNOWN, and hence the WCS should be used with some caution. For C2NC2 mode, the WCS quality is marked as PROBLEM and is likely to be inaccurate by as much as 200–400″.	OC2H, OC3C, OC3D
	[IMG_04C] WCS Incorrect (C): For C2NC2 mode the WCS quality is marked as PROBLEM and is likely to be inaccurate by as much as 200–400″. The WCS solution provided with the raw data for NMC and NXCAC modes is now accurate to within 10″ (though may have WCS quality marked as UNKNOWN).	OC3I, OC3L
	[IMG_04D] WCS Incorrect (D): The WCS for all modes is now accurate to within 10″ or better.	OC4A
	[IMG_05] Mis-matched Chop/Nods: When the chop and nod amplitudes are not quite matched for FORCAST NMC data, directly stacking the frames results in an elongated or doubled central source that may not be useful for science. However, shifting the frame before stacking causes mismatches in the background structure, which results in strong artifacts in the background of the image.	OC2H, OC3C, OC3D, OC3I, OC3L, OC4A, OC4I
	[IMG_06] Vignetting: A number of observations from OC2D suffered from telescope vignetting. If an observation was potentially vignetted, the LEVEL 3 (flux calibrated) file will have the following HISTORY record in the FITS header: *HISTORY Vignetted, calibration is uncertain!*	OC2D, OC2F
	[IMG_07] Bad Corner Pixels: There is a bad pixel cluster in the LWC channel of the FORCAST array in the upper right corner. This has no effect on the rest of the data in the image but can cause problems with auto scaling in image display tools (e.g., DS9) and in mosaicking.	OC3L
	[IMG_08] Minor issue with droop correction in LWC: Observations taken in the LWC short wavelength filters (8.6, 11.3, 11.8, and 24.2 µm) show minor artifacts close to bright sources due to small errors in the Droop Correction parameters. Most science observations are not affected by this issue	OC2H, OC3C, OC3D, OC3I, OC3L, OC4A, OC4G, OC4I

Table 17: Continued

MODE	ISSUES	SERIES
Imaging	**[IMG_09] UTCSTART Keyword for C2NC2 Mode:** The value for UTC-START in the FITS headers for observations obtained in the C2NC2 mode is likely to be incorrect by up to ~1 arcmin.	OC1B, OC1D&F, OC2B, OC2D, OC2F, OC2H, OC3C, OC3D, OC3I, OC3L, OC4A
	[IMG_10] Smearing due to sky rotation: Possible smearing at edges of imaging data in some filters for long exposures with large rotations on sky. This is due to small inaccuracies in boresite definition (center of rotation) during rotation step while coadding (COA/CAL files).	OC1B, OC1D&F, OC2B, OC2D, OC2F, OC2H, OC3C, OC3D, OC3I, OC3L, OC4A
	[IMG_11] Incorrect boresite: Boresite was setup incorrectly causing errors in the WCS. These were updated manually where possible using WISE. 2MASS, or UCAC4 positions in the final COA and CAL files.	OC5J
	[IMG_12] Poor Nod subtraction: Excess noise is seen as a ripple effect in the background in the 19.7 µm filter (FOR_F197) due to poor NOD subtraction. Dithering alleviated most of the problem but still resulted in poorer than normal background subtraction.	OC5J
	[IMG_13] Nod Misalignment: A mechanical issue associated with the telescope has resulted in misalignment or imperfect matching of the Nods in one FORCAST mode (NMC mode with large Nod Throws≥120 arcsec). This has resulted in double sources with misalignments on scales of 3-5 arcsec. Only data showing header keywords containing NODSTYLE=NMC and NODAMP≥120 are affected.	OC5J, OC5K
	[IMG_14] Window Degradation: Degradation of the FORCAST entrance window resulted in poor background subtraction and artifacts that could not be removed by the pipeline. Calibration factors in the SWC are substantially different (by ~35%) from those derived from previous cycles. Data files are marked as USABLE and observers are cautioned that ancillary data may be required to assess the calibration accuracy. The LWC was also affected and both channels saw variable backgrounds with streaks and large bright and dark areas.	OC6J
	[IMG_15] Array Debris: String-like artifact on the FORCAST short wavelength camera (SWC) array is prominent in data with insufficient dithering. Pipeline was unable to remove this artifact with a custom bad pixel mask due to strong variations in the background due to the degradation of the entrance window.	
	[IMG_16] Distortion: Possibly due to the degradation of the entrance window in Cycle OC6J, images appear to be distorted with the distortion gradually increasing with distance from the center of the array. This distortion is beyond what is regularly being corrected by the pipeline.	
	[IMG_17] Window: New entrance window greatly improved the background noise as compared to OC6J, but still suffered from some structure seen as arcs of positive and/or negative emission at the very edges of the array.	OC7D, OC7G

Table 17: Continued

MODE	ISSUES	SERIES
Imaging	**[IMG_18] Debris:** Some debris has fallen onto the FORCAST array resulting in larger than normal NaN regions in the bad pixel masks. Dithering was added to programs to remove this effect from the data, but it still may be seen in single non-dithered images and acquisitions.	OC8I, OC8O, OC9A, OC9J, OC9V
	[IMG_19] Calibration SWC: During three series (OC6J, OC7D, OC7G) the calibration values referenced to previous data (REFCAL) show an overall decrease in sensitivity. This may be due to the use of a degraded FORCAST entrance window in series OC6J, but problems continued with the replacement window used for OC7D and OC7G as well. The overall change in REFCAL was not consistent across all SWC filters with some filters showing little or no changes (such as FOR_F056), while filters such as FOR_F253 and FOR_F111 changed as much as ~35%. The window was changed again for OC8I, and the values stabilized, and sensitivity returned to nominal values. Please refer to Section 3.4.3 for detailed plots.	OC6J, OC7D, OC7G
	[IMG_20] Calibration LWC: See description of this issue in [IMG 19] above. However, unlike the SWC, the referenced calibration (REFCAL) values for the LWC did not change significantly even with the degraded window used in series OC6J. However, with the window change for OC7D, the calibration changed significantly with an overall decrease in sensitivity. Also, unlike the SWC the calibration values never stabilized throughout the rest of the lifetime of FORCAST even after the window change for OC8I. This change was also not consistent across all filters and were much more extreme. Differences of ~15% could be seen in FOR_F113 while for filters FOR_F315 and FOR_F336 there were calibration differences of >40% as compared to earlier series. Please refer to Section 3.4.3 for detailed plots.	OC7D, OC7G, OC8I, OC8O, OC9A, OC9J, OC9P, OC9V
Grism	**[GRI_01] Ghosting in G6:** Currently the G6 grism suffers from significant ghosting for bright sources, which shows up as a faint spectrum just above the main source in the 2D image. Furthermore, analysis of both stellar and asteroid response curves (i.e., red and blue) indicates that if there is an effect on the flux calibration, it must be less than 5%.	ALL except OC1B & OC1D&F
	[GRI_02] Cross-correlation artifacts: Some FORCAST grism spectra may show very low-level artifacts due to small wavelength shifts between the observation data and the telluric model incurred by slight inaccuracies in the cross-correlation. To verify whether a feature is an artifact or not, download the MRG file for the observation (which is not shifted) and divide by the telluric spectrum and response curve in the original L3 file. Comparing this result to the original L3 spectrum should reveal which features are artifacts due to anomalous shifts.	ALL
	[GRI_03] Telluric correction: All FORCAST spectra should be compared to the telluric model spectrum to identify possible artifacts (e.g., “P Cygni” lines) due to a mis-match between the true PWV and what is assumed for the telluric model. This issue is mitigated for reprocessed data (with SNR $>$ 10) from Cycle 2, 3, and 4.	OC1B, OC1D&F
	[GRI_04] Edge Artifact: This artifact is observed in FOR_G063 and FOR_G111 grisms. In the 2D image of FOR_G063, it manifests as a small ($\approx$ 5 pixel) bright dot close to the PSF of the source. This results in enhancement of flux in the first 5 pixels (i.e., for wavelengths $<$ 5.5 μm) of the spectra. A similar effect is seen in FOR_G111 but instead of enhancement of flux, a drop in the flux is seen for the last 5 pixels (i.e., wavelengths $>$ 13.5 μm). It is recommended that users should determine if their data is affected by this artifact and if the edges of the spectra should be excluded from analysis.	ALL
	[GRI_05] Bad blocker for grism G6: Due to a bad blocker filter, observations with the G6 grism (FOR_G329) have significant contamination from other orders. These observations have not been processed further and should not be used for science. A new blocking filter was installed for observing Cycle 2 to address this issue.	OC1B, OC1D&F

Table 17: Continued

MODE	ISSUES	SERIES
Grism	**[GRI_06] G4xG3 Ghosting:** Any data taken in the G4xG3 cross-dispersed mode are significantly contaminated by ghost images and should not be used for science. There are lower-level ghosts in the G1 and G3 spectra, especially for bright sources.	OC1B, OC1D&F
	[GRI_07] G3 wavecal issue (minor): The wavelength calibration for the G3 grism (FOR_G111) is off by a little over a pixel near 12.8 µm.	OC1B, OC1D&F
	[GRI_08] B Beam not extracted in some cases: Due to an error in the nodding specification, the negative ("B") beam in some observations was too faint to extract. In these cases, only the positive ("A") beam was extracted.	OC2B
	[GRI_09] Wavelength calibration for FOR_XG063: Currently the wavelength solution for the G2xG1 mode (FOR_XG063) in the highest orders is extrapolated due to lack of suitable reference lines. Initial testing indicates that the current wavelength solution may be off by 3–4 pixels for wavelengths shorter than 5.7 µm	OC2H, OC3C, OC3D
	[GRI_10] First Frame Artifact: Two dark structures are seen on the right side of the array for grisms FOR_G227 and FOR_G329. This only occurs in the first frame of a set and disappears by the second frame. This may be due to a settling of the array temperature when changing frametimes, though the exact cause is not known. The effect is small and mostly inconsequential for bright objects, however it may cause significant issues due to noise in the background region for the faint spectra.	ALL except OC1B & OC1D&F
	[GRI_11] Nod Misalignment: A mechanical issue associated with the telescope has resulted in misalignment or imperfect matching of the Nods in one FORCAST mode (NMC mode with large Nod Throws≥120 arcsec). This can result in double instances of the source and/or the source being slightly out of the slit in one Nod beam. Only data showing header keywords containing NODSTYLE=NMC and NODAMP≥120 are affected. This mode was only used with one source on FT428.	OC5J
	[GRI_12] Wavelength Calibration: The wavelength calibration for the G111 grism is uncertain due to changes in the instrument and the unavailability of valid calibration files. Users are cautioned that the reduced spectra for this grism may exhibit spurious emission and absorption features, due to the misalignment of the telluric absorption features in wavelength. The spectra will be re-reduced and re-calibrated in the future when accurate wavelength calibration files are available.	OC7D & OC7G